Western Australian School of Mines

Impurity Rejection in the Nickel Laterite Leach System

Kai Wang

This thesis is presented for the Degree of
Doctor of Philosophy
of
Curtin University

September 2012

Declaration

To the best of my knowledge and belief this thesis contains no material previously published by any other person except where due acknowledgment has been made.

This thesis contains no material which has been accepted for the award of any other degree or diploma in any university.

Signature: …  ……

Date: ……23-08-2012……...

ACKNOWLEDGEMENTS

I would like to take this opportunity to acknowledge the financial support of the Parker Cooperative Research Centre for Integrated Hydrometallurgy Solutions (established and supported under the Australian Government's Cooperative Research Centres Program).

There are many people I would like to thank for helping me complete this PhD project. First, I wish to express my most sincere gratitude to my supervisory panel: Associate Professor Richard Browner, Dr. Jian Li and Dr. Robbie McDonald. This thesis would not have been possible without their thoughtful guidance and constructive suggestions. Their scientific attitudes to seeking truth have inspired me. Thanks for helping me grow.

I am also grateful to Dr. Rob Hart, Dr. Ross Williams and Ms. Elaine Miller for their expertise on XRD and SEM at the Centre for Materials Research (CMR), and Mr. Peter Chapman for his assistance with FTIR at the Department of Chemistry, Curtin University. Thanks also go to Mr. Milan Chovancek, Ms. Sophia Surin, Mr. Bruno Latella, and Ms. Tuyen Pham from the analytical team at CSIRO Process Science and Processing.

I wish to thank Andrew, Robert, Mike, Teresa, Warren and Neil, for providing daily support throughout my studies. Special thanks go to my good friend, Katie Shiraishi, for helping me in general, particularly a positive attitude towards life.

Finally, I would like to give a biggest and warmest hug to my wife, Lucy, for being supportive, inspirational, and her unconditional love.

ABSTRACT

Atmospheric leaching (AL) of low-grade nickel laterite ores can produce a pregnant leach solution (PLS) containing significant amounts of impurities such as trivalent iron, aluminium and chromium ions. Purification of PLS by precipitation of the impurities with an alkaline reagent often causes an associated loss of nickel. This thesis documents an investigation of the physicochemical processes that occur during the precipitation of iron, aluminium and chromium from both synthetic and real nickel laterite AL leach liquors and associated nickel losses.

A chemical equilibrium model in the Fe(III)–Ni(II)–H_2SO_4–H_2O system was developed with the effects of ionic strength and temperature taken into account. This model was able to calculate the concentration distribution of iron and nickel species over the pH range from 0 to 4 and temperature from 25 to 100 °C, and predict the pH value of the solution. In addition, the model can calculate the saturation index of iron oxides such as goethite, ferrihydrite and schwertmannite to predict whether a specific iron oxide will precipitate or dissolve under particular conditions. The solubility of goethite, ferrihydrite and schwertmannite decreased substantially with increasing pH value. Goethite, ferrihydrite and schwertmannite were all undersaturated below pH 2. With increasing pH, ferric ions tended to precipitate first in the form of ferrihydrite followed by goethite and schwertmannite. A mixture was formed above pH 2.5, of which schwertmannite was the dominant phase.

Considerable effort has been put into the experimental study on the relationships between impurities removal and nickel losses from nickel laterite AL liquors. The precipitation experiments were conducted in either single- or multi-stage simulation using synthetic and real PLS. For the single-stage precipitation experiments conducted using a synthetic PLS containing Fe(III)+Ni(II), the effects of the factors governing the iron precipitation process upon nickel losses were investigated by statistical analysis and modelling. Temperature, pH and the initial Fe/Ni ratio in PLS

were found to be the important factors affecting iron removal efficiency and the level of nickel loss to solid. These factors were studied using a three-level Box-Behnken design combined with response surface methodology. Quadratic models were fitted to the experimental data, to enable construction of 3D response surfaces and corresponding contour plots. These graphs clearly demonstrated the links between responses and the interactions of factors.

Further single-stage precipitation experiments performed using PLS containing Fe(III)+Ni(II)+Al(III), Fe(III)+Ni(II)+Cr(III), and Fe(III)+Ni(II)+Al(III)+Cr(III) showed that greater losses of nickel to solids occurred in the presence of aluminium and chromium. Increasing the pH value of solution and precipitation temperature favored the removal of iron, aluminium and chromium, but at a cost of greater nickel losses. By carefully controlling pH and temperature using a multi-stage precipitation process, however, the iron, aluminium and chromium can be effectively rejected with a minimal nickel loss and desirable sludge properties. The optimum conditions for a multi-stage precipitation process were found to be at pH 3 and 55 ºC in the first stage followed by a second stage operated at pH 3 and 85 ºC. Using this precipitation procedure, as much as 95% iron and chromium together with above 80% aluminium can be removed; the level of nickel loss to the solid can be reduced to below 1%. The sludge showed a fast settling rate of 5.05 m/h with the addition of a cationic flocculant. Similar satisfactory results were also obtained when performing this multi-stage precipitation procedure on real leach solutions.

The effect of water salinity on impurities removal and nickel losses was also examined due to variable nature of process water available in Western Australia to process nickel laterite during atmospheric leaching. This was achieved by conducting single-stage precipitation experiments in Fe(III)+Ni(II)+Al(III)+Cr(III) systems with various amounts of sodium chloride added. The presence of high concentration of salts resulted in higher removal efficiencies for iron, aluminium and chromium, and less nickel losses to the solids, particularly when the precipitation reactions were

carried out at 85 ºC. XRD analysis of the residues confirmed that the poorly structural-ordered schwertmannite and/or ferrihydrite were the dominant phases. Natrojarosite ($NaFe_3(SO_4)_2(OH)_6$) can be detected when the precipitation reaction was conducted at pH 2 and 85 ºC from synthetic solution with high salinity.

The presence of large amounts of poorly structural-ordered schwertmannite and ferrihydrite in the iron-rich residues complicates mineralogical identification using routine XRD technique. A comprehensive characterization was performed using a combination of several techniques that include selective Acidified Ammonium Oxalate (AAO) dissolution, differential XRD, SEM and FTIR spectroscopy. These techniques in combination allowed reliable mineralogical identification for samples containing high proportions of schwertmannite and ferrihydrite. The effects of foreign metallic cations on the crystallization, dissolution behaviour and surface sulphate coordination were investigated. The results suggested that the presence of goethite in the precipitates can be identified after removing the schwertmannite and/or ferrihydrite. Nickel, aluminium and chromium retarded the transformations of schwertmannite and/or ferrihydrite to goethite, but aluminium and chromium supressed the formation of 6-line ferrihydrite. Also, aluminium and chromium influenced the symmetry of the sulphate absorbed onto the iron-rich precipitates. The structural order of the phases became less pronounced with the presence of foreign metallic cations, particularly aluminium and chromium. Aluminium and chromium can strongly stabilize iron-rich precipitates making these resistant to leaching by AAO solution. FTIR analysis confirmed the presence of goethite in the bi-metallic precipitates and suggested that the sulphate is present to a greater extent in lower symmetry environments.

TABLE OF CONTENTS

LIST OF FIGURES

LIST OF TABLES

CHAPTER 1

INTRODUCTION

1.1 THE ISSUE

Nickel and its alloys have gained wide application in industry due to their excellent corrosion and heat resistance. Approximately 70% of the land-based nickel reserves are present in lateritic deposits, but these only account for 40% of worldwide nickel production (Dalvi *et al*., 2004). Major nickel production in the future, however, is expected to be from nickel laterite ores.

High temperature pressure acid leaching (HPAL) is almost extensively used for processing laterite ores. Whittington and Muir (2000) systematically reviewed the HPAL technique for processing nickel laterites in terms of mineralogy, leaching chemistry, operating conditions, residue properties and scaling. In subsequent publications (Whittington and Johnson, 2005; Whittington *et al*., 2003a; 2003b), the effects of water salinity, ore type and acid loading were discussed in detail. However, the HPAL process often requires high capital expenditure (CAPEX), and operating expenditure (OPEX). In addition, the process is best suited to ores containing above 40 wt.% iron. Lateritic ores with less than 40 wt.% iron usually contain a higher amount of acid consuming minerals such as magnesium silicates, and are not economically suitable for direct high pressure leaching (Arroyo and Neudorf, 2004).

In recent years, a considerable amount of research has been undertaken investigating more economical and environmentally sound hydrometallurgical approaches for the treatment of nickel laterite ores. Particularly, interest in atmospheric leaching (AL) has been mounting, which is considered as a potentially lower cost alternative to HPAL for laterite projects (McDonald and Whittington, 2008a; 2008b). However, AL is still in its infancy, and many issues have not been resolved. One of the key

problems is that the pregnant leach solution (PLS) from AL usually contains significant amounts of impurities such as soluble trivalent iron, aluminium and chromium ions. For example, typical concentration values for these impurities in the PLS from the heap leaching of Greek nickeliferous laterite with sulphuric acid are reported as 23 g/L Fe^{3+}, 6.0 g/L Al^{3+} and 1.0 g/L Cr^{3+} (Agatzini-Leonardou *et al.*, 2009). In some cases, the concentration of ferric iron which is the main impurity in the PLS can be quite high with Arroyo and Neudorf (2004) reporting 82 g/L. Inefficient removal of those impurities represents a significant impediment to producing pure cobalt and nickel compounds and/or metals in the subsequent downstream hydrometallurgical processing. Therefore, effective purification methods must be developed to selectively remove or reject these ions from the PLS.

Iron is a ubiquitous impurity in PLS for various processes, therefore, most solution purification processes strongly focus upon iron removal. A number of methods that include hydrolysis-precipitation, solvent extraction and ion-exchange have been developed for the iron removal from hydrometallurgical processing solutions. Currently, hydrolysis-precipitation is the favored technique for iron removal, as the reagent costs are low and the precipitates are potentially feed to the iron industry. However, a practical problem in precipitating iron and other impurities during the processing of nickel laterite PLS is the loss of nickel (and cobalt) to the solid precipitates. The laboratory study on iron, aluminium and chromium removal from laterite heap leach solutions conducted by Guise and Castro (1996) showed that 26.5% nickel and 37.1% cobalt were lost to the solids when precipitation was conducted at pH 2.5 and 90 ºC. Recently, Köse and Topkaya (2011) investigated the impurities rejection from column leach liquors of nontronite type lateritic ores, and showed that 100% iron, 92.6% aluminium and 99.6% chromium were removed at pH 3.5 and 90 ºC, but at a cost of 15.7% nickel loss to the iron-bearing precipitates.

The level of nickel loss to the solid in the above impurity-removal processes is very high. Therefore, a need exists to extend investigations on the impurity-removal

process to achieve acceptable levels of nickel loss.

1.2 THESIS AIMS

The principle aim of this thesis is to understand the physicochemical processes that occur during the precipitation of iron and other impurities from both synthetic and real nickel laterite leach liquors and associated nickel losses. Furthermore the aim is to develop a precipitation process to remove impurities efficiently without causing significant losses of nickel. This will be complemented by a series of further aims:

- Initially in this project perform research to advance the understanding of the nature of iron precipitation. This will be achieved by the theoretical investigation of chemical equilibrium of the Fe(III)–Ni(II)–H_2SO_4–H_2O system, which will give insight into the ionic behavior of a mixed metal sulphate aqueous system that commonly occurs in hydrometallurgical processing.
- Investigate the correlation between iron precipitation and nickel loss from synthetic nickel laterite AL liquors containing just iron and nickel ions. The examined factors that are governing the iron precipitation process will include pH, temperature, neutralizing agent, the initial Fe/Ni ratio in the PLS and stirring speed.
- Study the iron, aluminium and chromium co-removal from both synthetic and real nickel laterite AL liquors.
- Develop a multi-step precipitation process to remove impurities effectively and minimise the losses of nickel.
- Investigate the effect of water salinity on iron, aluminium and chromium removal and associated nickel losses.
- Gain further insight into the impurity precipitation chemistry and the nickel loss mechanism through mineralogical and chemical characterization of the iron-rich precipitates by using techniques that include selective Acidified

Ammonium Oxalate (AAO) dissolution, XRD/DXRD, SEM, and FTIR spectroscopy.

1.3 THESIS STRUCTURE

According to the aims of this thesis, Chapter 2 provides a literature review of common iron removal processes and associated nickel losses. The theoretical background of iron hydrolysis and solids formation is described: nucleation, growth, aging and aggregation in precipitation processes. The methods of precipitation and strategy of experimentation are also briefly reviewed in this chapter.

Chapter 3 presents a theoretical investigation of the chemical equilibria in the Fe(III)–Ni(II)–H_2SO_4–H_2O system. A non-ideal chemical speciation model is developed to calculate the concentration distribution of iron and nickel species in a mixed ferric and nickel sulphate aqueous solution over the pH range from 0 to 4 and at temperatures from 25 to 100°C. The ionic strength-dependent equilibrium constant is treated through a semi-empirical Vasil'eV equation, which is based on an extended Debye–Hückel theory.

Chapter 4 is an experimental investigation of the correlations between iron precipitation and associated nickel losses in synthetic PLS containing just iron and nickel ions. The effects of the key process variables, pH, temperature, initial Fe/Ni ratio in synthetic PLS, stirring speed and type of neutralization agent, on the nickel losses are studied using methods of statistical analysis and modelling.

Chapter 5 describes an experimental study on iron, aluminium and chromium co-removal and associated nickel losses from both synthetic and real nickel laterite PLS. The first part focuses on the single-stage precipitation experiments conducted in PLS containing Fe(III)+Ni(II)+Al(III), Fe(III)+Ni(II)+Cr(III), and Fe(III)+Ni(II)+Al(III)+Cr(III). The second part centers on the development of a multi-step precipitation procedure to remove iron and other impurities effectively,

and to minimise nickel losses.

Since there is the possibility to use seawater or hypersaline water in the processing of laterite ore under atmospheric conditions, Chapter 6 is an investigation of impurities rejection from synthetic PLS with the presence of various amounts of chloride salts (added as sodium chloride). The first part of this chapter investigates the effect of water salinity on impurity removal efficiencies and associated nickel losses. The second part focuses on the effect of water salinity on changes to the mineralogy of the precipitates.

Chapter 7 describes a comprehensive characterization of iron-rich precipitates. The iron-bearing residues normally contain large amounts of poorly defined phases such as schwertmannite and ferrihydrite. This often leads to difficulty in mineralogical identification using routine XRD methods. A combination of several techniques that include selective dissolution using Acidified Ammonium Oxalate (AAO) solution, Differential XRD, SEM and FTIR spectroscopy are applied to enable correct mineralogical identifications.

Chapter 8 gives a summary of the outcomes of the work in relation to the aims of this thesis, and future work that may be undertaken based on the outcome of the thesis.

CHAPTER 2

LITERATURE REVIEW

2.1 IRON REMOVAL IN HYDROMETALLURGICAL PROCESSING

A convenient way to control iron removal in the precipitation process is to change important precipitation factors such as temperature and pH. This was recognized by Babčan (1971) who studied the iron phases formed in 0.5 M ferric sulphate solution (Figure 2.1).

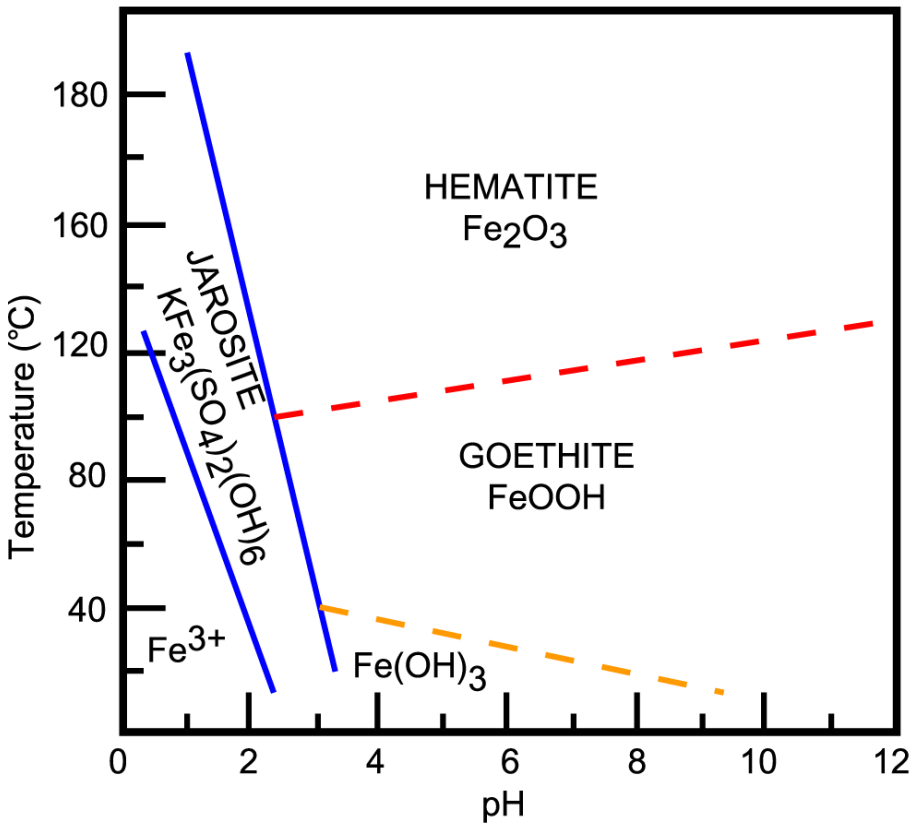

Figure 2.1: Stability regions of different iron precipitated phases (After Babčan (1971)).

The composition and physical nature of the hydrolysis products are normally dependent on kinetic factors and equilibrium relationships. Figure 2.1 shows the relationships between the main equilibrium iron-containing phases but does not include any metastable phases or intermediates, such as ferrihydrite and schwertmannite. The hydrated iron-bearing oxyhydroxide and oxyhydroxysulfate intermediates tend to transform over time to more stable, crystalline iron oxides such as goethite and/or hematite (Cornell and Schwertmann, 2003). In hydrometallurgical operations, the stable and metastable iron phases are often present together in the residues.

There have been a number of precipitation processes proposed for iron removal. Excellent reviews of these processes have been given by Gordon and Pickering (1975) and Dutrizac (1987). While these iron removal processes are widely used for solution purification in the zinc industry, their application to nickel laterite projects has also been explored (Arroyo and Neudorf, 2004; Liu, 2003; Lowenhaupt *et al*., 1985). Generally, the precipitation of iron in nickel processing follows the same routes used in the zinc industry, and an understanding of these processes therefore comes from the studies centred on the processing of zinc. Figure 2.2 gives a comparison between different iron removal processes.

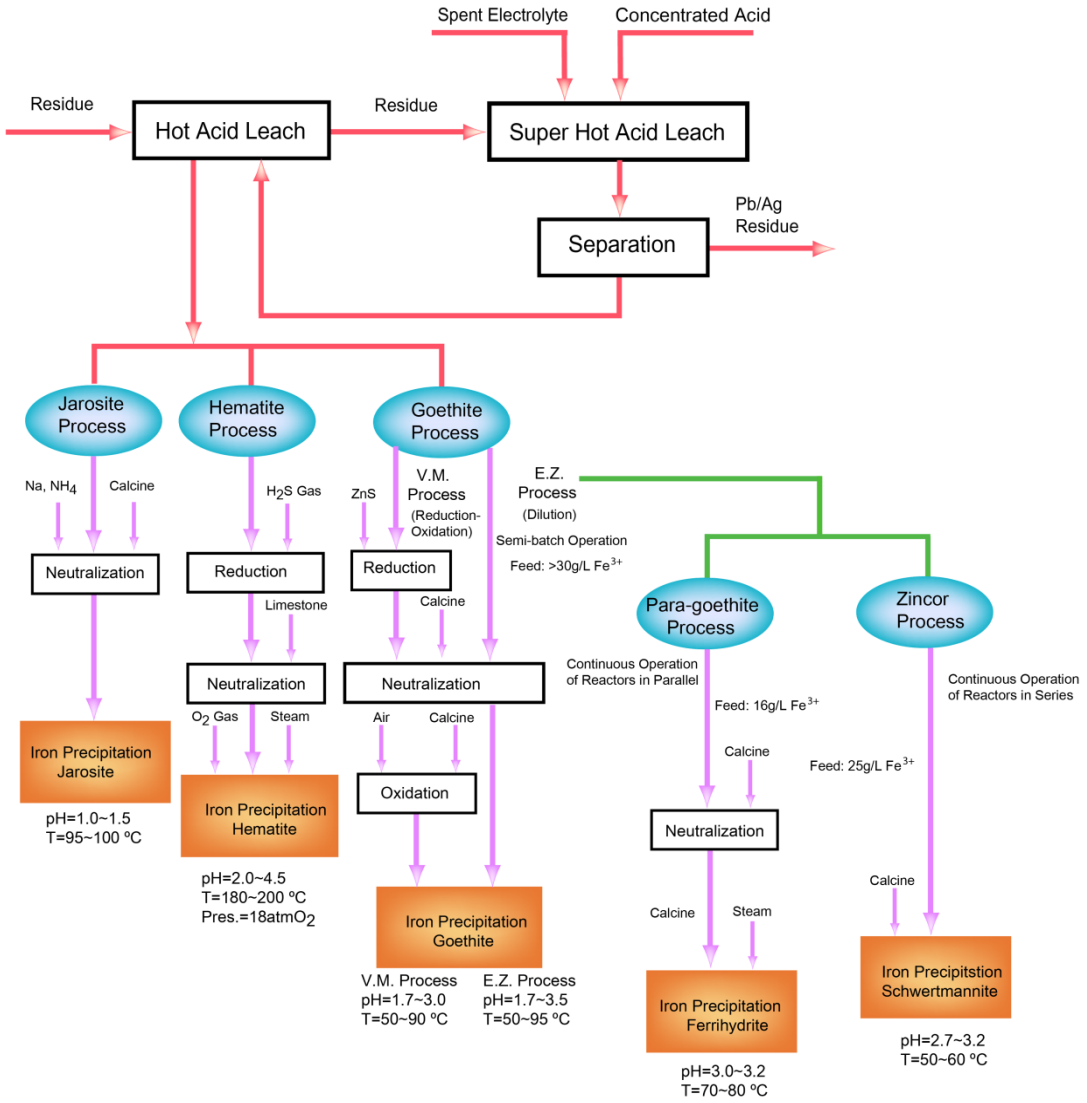

Figure 2.2: Simplified schematic presentation of various iron removal processes (After Allen *et al*. (1970), Bodson (1972), Gordon and Pickering (1975), Dutrizac (1987), Claassen (2002) and Loan *et. al*. (2006)).

The Hematite Process in some respects is an ideal method for the precipitation of iron from PLS, since the iron products have a greater market value with potential application for cement, pigment and steel manufacture (Dutrizac, 1987). Such a process, however, often requires a high temperature-pressure hydrolysis reaction, which involves high costs to construct and maintain the autoclaves. The Jarosite Process is the most commonly used technique for iron removal, as the jarosite-type precipitates are easy to filter, and the precipitation can be carried out in strongly

acidic media (Dutrizac and Kaiman, 1976). However, the larger volumes of jarosite-type residues produced are also thermodynamically unstable, and tend to decompose slowly to produce sulphuric acid and release heavy metals into the environment (Gupta and Mukherjee, 1990). The essential feature of the Goethite Process is that the concentration of ferric iron should be maintained at less than 2 g/L during precipitation (Dutrizac, 1987). Since most leach solutions contain much higher iron concentrations, the Goethite Process initially appears to have little place in hydrometallurgical processing. Two approaches, however, have been developed to allow goethite precipitation. The first method was established in the 1960s by the Vieille-Montagne Company (V.M.) (Bodson, 1972), in which the ferric ions are first reduced to ferrous and then oxidized by air at a controlled rate to precipitate goethite. The Electrolytic Zinc Co. of Australasia, Ltd. (E.Z.) further improved the Goethite Process using a dilution-precipitation approach (Allen *et al.*, 1970). The concentrated leach solution is diluted into a precipitation vessel containing a large volume of solution, producing a low concentration ferric ions (<1 g/L) that are precipitated at 85 to 95 ºC and pH 2.8 to 3.5. The E.Z. method lead to the development of another two iron removal processes in the 1990s: the Paragoethite Process and Zincor Process (Cubeddu *et al*., 1996; Meyer *et al*., 1996). Unlike the Hematite, Jarosite and Goethite Processes, the Paragoethite and Zincor Processes are much less common, being in operation at only three commercial zinc production sites (Claassen *et al*., 2002; Cubeddu *et al*., 1996; McCristal and Manning, 1998). One significant refinement of these two new processes is the change from semi-batch or non-continuous precipitation to a continuous process (parallel or series tanks). These two processes are reported to give lower capital and operating cost, but the residues contain significant amounts of poorly filterable iron oxides/hydroxides and basic iron sulphates rather than the conventional goethite precipitates. Very little information was available on the exact nature of the Paragoethite and Zincor residues, until the recent studies of Loan *et al*. (2006) and Claassen *et al*. (2002) identified 6-line ferrihydrite and schwertmannite to be the major iron precipitation products.

2.2 IRON HYDROLYSIS CHEMISTRY AND PRECIPITATION PATHWAYS

Hydrolysis of Fe (III) consists of a series of deprotonation or polymerization steps. The deprotonation process forms $Fe(OH)_x^{(3-x)+}$ species through two equilibrium reactions (Knight and Sylva, 1974):

$$Fe^{3+} + H_2O \longleftrightarrow FeOH^{2+} + H^+ \qquad \text{Eq. 2.1}$$

$$FeOH^{2+} + H_2O \longleftrightarrow Fe(OH)_2^+ + H^+ \qquad \text{Eq. 2.2}$$

Two monomeric species ($FeOH^{2+}$) tend to form the more stable dimer ($Fe_2(OH)_2^{4+}$). The dimer acts as the precursor to other Fe (III) oxides and oxyhydroxide, such as 6-line ferrihydrite (Schwertmann, 1991). Monomers and dimers can interact to produce trimers, which are only identified in chloride media (Bottero *et al.*, 1994). The existence and identification of other species beyond monomers, dimers and trimers is still contested, as polymerization reactions proceed quite fast with increasing OH^-/Fe mole ratio in solution (Flynn, 1984). It is normally difficult to stop the polymerization reaction at a molecular level due to the high activity of polynuclear species (Jolivet *et al.*, 2004). Further polymerization leads to the formation of reddish-brown polynuclear species with much higher molecular weight ($Fe_pO_r(OH)_s^{[3p-(2r+s)]+}$). Iron atoms in these polynuclear species are octahedrally coordinated to at least one H_2O molecule (Schneide, 1984; Schwertmann, 1991). These colloidal and gelatinous polynuclear species transform to nanoscale polymers with low structural order corresponding to the formation of ferrihydrite (Misawa *et al.*, 1974).

It is often difficult to make a clear structure distinction between polynuclear species and ferrihydrite. The disordered nature of ferrihydrite results in small diffracting domains that are hard to detect by conventional X-Ray Diffraction (XRD) (Jambor

and Dutrizac, 1998). Ferrihydrite is often wrongly designated as hydrous ferric oxide (HFO), colloidal ferric hydroxide ($Fe(OH)_3$) or amorphous iron oxide. Ferrihydrite is conventionally named as "2-line" or "6-line" based on the number of X-ray diffraction lines. Recently, Michel *et al*. (2007) determined the structure of 6-line ferrihydrite and published their work in the journal Science, but their deductions have been questioned by other researchers in the following years (Rancourt and Meunier, 2008). Although the exact structure of ferrihydrite has not been fully understood, the presence of hydroxyl is widely assumed to be essential for maintaining the ferrihydrite structure. The discrepancy in the structural models of ferrihydrite results in the various reported chemical formula: see, for example, $Fe_5HO_8 \cdot 4H_2O$ (Towe and Bradley, 1967), $FeO_x(OH)_{3-2x}$ (Misawa *et al.*, 1974), $Fe_4(O,OH,H_2O)_{12}$ (2-line ferrihydrite) and $Fe_{4.6}(O,OH,H_2O)_{12}$ (6-line ferrihydrite) (Eggleton and Fitzpatrick, 1988). The extensively reported formula, $5Fe_2O_3 \cdot 9H_2O$, is thought to be excessively hydrous (Jambor and Dutrizac, 1998). Michel *et al.* (2010) proposed a new composition for disordered ferrihydrite, $Fe_{8.2}O_{8.5}(OH)_{7.4}+3H_2O$, which differs significantly from previous suggested chemical compositions.

In aqueous solution, ferrihydrite is thermodynamically unstable, and tends to transform over time to goethite and hematite. Ferrihydrite dissolves to reform the soluble ions such as $Fe(OH)_2^+$ in acid solution (pH~4) and $Fe(OH)_4^-$ in alkaline media (pH~12) (Cornell and Schwertmann, 2003). The formation of goethite is favored at such pH values, but the formation of hematite reaches a maximum at a medium pH range (pH~7-8) when the concentration of the monovalent $Fe(OH)_2^+$ ion is a minimum. In strong acidic media (pH<4), the growth of monovalent $Fe(OH)_2^+$ is inhibited by the presence of $FeOH^{2+}$ which is less favorable for goethite formation than the monovalent ion. However, this process (pH<4) favours the formation of hematite (Schwertmann and Murad, 1983). Thus, the formation of goethite and hematite from ferrihydrite seems to be simultaneous, but the conditions that favour the formation of goethite, on the other hand, minimise hematite formation.

Hydrolysis of concentrated ferric solutions by rapid addition of alkali to raise the pH of solution to the pH range between 7 and 8 normally results in the formation of 2-line ferrihydrite (Lewis and Cardile, 1989). If the hydrolysis of Fe^{3+} happens relatively slowly at low concentration and pH values (pH 2.5-3.5), more ordered 6-line ferrihydrite forms (Schwertmann, 1991). This is consistent with the work of Michel *et al*. (2007) reported, 6-line ferrihydrite has few vacancies, hence better structural ordering, presumably as a result of slower precipitate growth. However, aging 2-line ferrihydrite in aqueous solution does not transform it into the relatively well-ordered 6-line ferrihydrite, but usually leads to the formation of hematite and/or goethite (Schwertmann and Murad, 1983).

In the presence of sulphate ions, hydrolysis of ferric ions becomes quite complicated as the formation of the $FeSO_4^+$ complex strongly suppresses the polymerization of the hydroxyl complex and the precipitation of goethite (Cornell and Schwertmann, 2003). The experimental work by Sapieszko *et al*. (1977) has shown that $FeSO_4^+$ is the dominant species at the temperature range from 25 to 85 ºC in ferric sulphate solutions. The hydroxo-forms of Fe(III) exist as mixed hydroxyl sulphate complexes $Fe_2(OH)_2(SO_4)_x^{4-2x}$. (Yakovlev *et al*., 1977). There is a growing awareness that these ferric hydroxyl sulphate complexes have close relationship to schwertmannite.

Schwertmannite ($Fe_8O_8(OH)_x(SO_4)_y$) is the predominant hydrolysis product of ferric iron in concentrated sulphate solution at pH 2 to 4 (Bigham and Nordstrom, 2000). The optimal conditions for the formation of schwertmannite are within the pH range from 3.0 to 4.5 and sulphate concentrations in the range of 1000 to 3000 mg/L (Bigham *et al*., 1994). The ideal formula of schwertmannite is $Fe_8O_8(OH)_6SO_4$, which indicates the Fe/S molar ratio of 8 is between jarosite (Fe/S=1.5) and the normal iron oxides (no S). The schwertmannite formula may also range to $Fe_8O_8(OH)_{4.5}(SO_4)_{1.75}$ depending on the degree to which tunnel and surface sites are saturated with sulphate (Bigham *et al*., 1996). Schwertmannite is a large and complex hydroxy ferric sulfate with poorly crystalline nature and is commonly

admixed with other nanophasic iron minerals. The sulphate in schwertmannite may be partly or fully substituted by anions such as arsenate and chromate. Bigham *et al*. (1994) indicated that schwertmannite is distinguished from ferrihydrite by a tunnel structure similar to that for akaganéite, which is formed in the chloride system. Claassen (2006) suggested that schwertmannite was nothing else but ferrihydrite with high sulphate values. The detailed structure study of schwertmannite using transmission electron microscopy and electron nanodiffraction by Loan *et al*. (2004) indicted that schwertmannite has a structure that is consistent with the maghemite-like structural component for ferrihydrite previously described by Janney *et al*. (2000) rather than the "modified" akaganéite structure proposed by Bigham *et al*. (1994).

At lower pH values (pH 1 to 2) and in the presence of monovalent ions, jarosite-type compounds, $MFe_3(OH)_6(SO_4)_2$, become predominant in sulphate media, where *M* refers to Na^+, K^+, NH_4^+, Ag^+, $1/2Pb^{2+}$ or H_3O^+, *etc*. (Dutrizac and Jambor, 2000). Jarosite synthesis is normally kinetically favored at elevated temperatures (>80°C).

Goethite formation is only favored at low ferric concentration and temperatures below 100°C in sulphate solution (Dutrizac, 1987). Bigham *et al*. (1994) indicated that goethite is a phase commonly associated with schwertmannite at relatively higher pH, especially at pH exceeding 4.5. Parida and Das (1996) suggested that the formation and crystallization of goethite was accelerated in $Fe(NO_3)_3$ solution in the presence of sulphate, though at higher SO_4^{2-}/Fe^{3+} ratio (1.0) formation of the $FeSO_4^+$ complex strongly inhibited the polymerization of hydroxy complexes and goethite precipitation.

2.3 CRYSTALLIZATION AND PRECIPITATION THEORY

Aqueous crystallization and precipitation both refer to unit operations that produce a solid from supersaturated solution. The distinction between crystallization and

precipitation is based on the speed of the process and the size of the solid particles produced (Jarvinen, 2008). Precipitation is generally regarded as being the process of reactive crystallization or fast crystallization (Dirksen and Ring, 1991). The same basic steps often occur in both crystallization and precipitation processes such as supersaturation, nucleation and growth (Jarvinen, 2008). Precipitation occurs from a highly supersaturated solution, resulting in fast nucleation and consequent formation of a large number of small crystals.

2.3.1 Nucleation and growth

Primary homogeneous nucleation occurs in the absence of any solid interface, where it is the dominant nucleation mechanism. The classical theories of primary homogeneous nucleation assume that the solute atoms or molecule units in supersaturated solution tend to combine together to produce clusters or embryos (Garside, 1985). The overall change of Gibbs free energy (ΔG) during the formation of embryos consists of two parts: the free energy associated with the generation of a new volume (ΔG_v) and the free energy due to the created new surface (ΔG_s). The Gibbs free energy of nucleus formation can be written as:

$$\Delta G = \Delta G_v + \Delta G_s = -\left(\frac{4\pi r^3}{3v}\right) kTlnS + 4\pi r^2\gamma \qquad \text{Eq. 2.3}$$

where r is the radius of the generated particle, v is the molecular volume of the generated embryo, k is the Boltzmann constant, T is temperature, S is the degree of supersaturation and γ is the surface tension. Nucleation occurs spontaneously only if ΔG<0, which means S in the first term on the right-hand side of Eq. 2.3 should be great than 1. Under this condition, ΔG has a positive maximum ΔG^*_{hom}, where nucleus size reaches a critical value (r_c). Figure 2.3 is the graphic representation of relationships of changes in Gibbs free energy and nuclei size. The value of ΔG^*_{hom} is the activation energy for nucleation to form critical size nuclei.

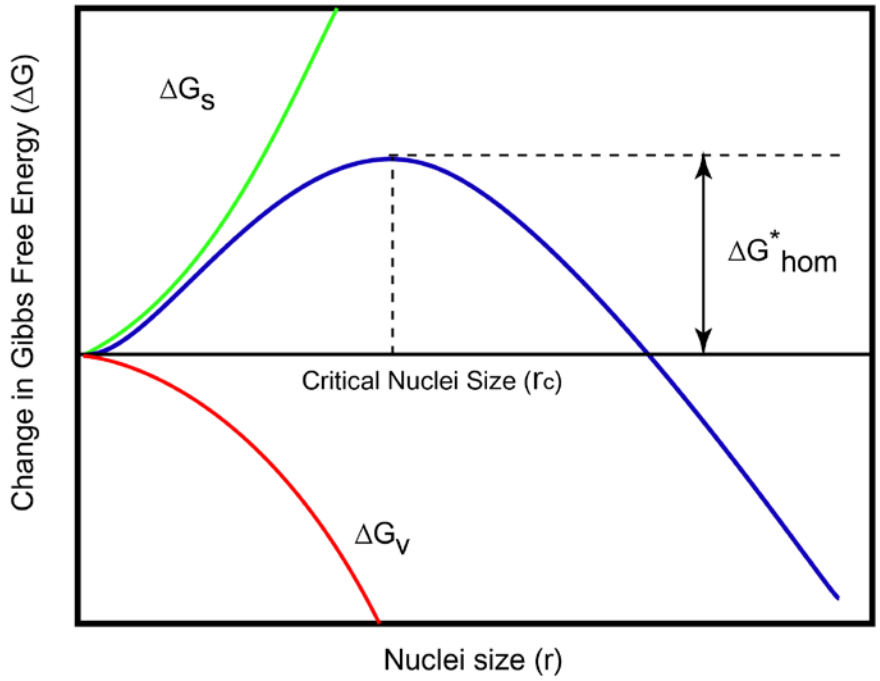

Figure 2.3: Change in Gibbs free energy during nucleation (After Mullin (2001)).

The experimental study of homogeneous nucleation in solution is difficult due to the inevitable presence of other solid phases within the system, *i.e.* particles of a foreign solid phase or the surface of reactors. Most primary nucleation that occurs is likely to be heterogeneous nucleation induced by surfaces (Garside, 1985). Nucleation on a surface is thermodynamically favored due to the lower surface energy, thus the overall free energy change associated with a critical nucleus formed by heterogeneous nucleation, ΔG^*_{het}, should be less than those for homogeneous nucleation, ΔG^*_{hom}. Turnbull (1952) described this process as:

$$\Delta G^*_{het} = \frac{(2+\cos\theta)(1-\cos\theta)^2}{4}\Delta G^*_{hom} \qquad \text{Eq. 2.4}$$

where θ is the contact angle between crystal nucleus and foreign solid surface. If θ=180°, $\Delta G^*_{het}=\Delta G^*_{hom}$, nucleation is not influenced by the foreign solid phase, whereas when liquids contact the surface of a solid phase in a liquid-solid system with θ<180°, then $\Delta G^*_{het}<\Delta G^*_{hom}$.

Once the stable nuclei (particles larger than the critical size) are formed in a supersaturated solution, these begin to grow into particles that are visible. This growth process often involves a series of stages: (a) transport of solute from bulk solution to the particle surface, (b) adsorption on the particle surface, (c) surface diffusion, (d) incorporation into the particle and (e) diffusion of solvent or other species away from the surface (Dirksen and Ring, 1991). Most of the growth processes for iron oxides or oxyhydroxides occur on the molecular scale, which involves the diffusion of "growth units" to the particle surface and then attachment. These attached units can either remain at their initial point of contact or diffuse across the surface and finally integrate into the crystal lattice at a "kink site" or return to the solution (Garside, 1985). A rough interface has many potential kink sites, and surface diffusion becomes less important. The attached units create new corners which are preferred sites for subsequent attachment of additional new unites. On the other hand, growth becomes more difficult when the interface is smooth. Surface diffusion becomes more important as kink sites are only present at the edges of either two-dimensional nuclei or surface steps. On the microscopic levels, surface layer or "step bunches" are often observed. These bunches consist of many molecular layers on the surface that have grouped together. Trapping of solvent inside the particle structure and other defects are mainly achieved by the step bunches. At larger macroscopic levels, heat transfer in solution is relatively fast compared to mass transfer. Thus, mass transfer limitations are predominant in growth control. The supersaturation or concentration gradients in solution can then influence the surface profiles and lead to instabilities in the growth process, which cause solution inclusions and dendrites. There are a range of theories relating to the mechanism and kinetics of crystal growth under particular conditions (Dirksen and Ring, 1991; Garside, 1985; Mullin, 2001; Söhnel and Garside, 1992).

2.3.2 Secondary processes

The dominant growth mechanisms that determine the final crystalline product

formed during precipitation are secondary processes including aging, recrystallization or Ostwald ripening and agglomeration.

Many precipitates formed are often disordered or metastable, and upon aging are transformed to stable compounds (Demopoulos, 2009). If two phases are supersaturated in a solution, the least stable phase precipitates first due to lower free energy of nucleation. This behaviour is referred to as Stranski's rule or the Ostwald Step rule and occurs in a homogeneous nucleation dominated system (Söhnel and Garside, 1992). A good proof of the validity of this rule is the hydrolysis reaction of ferric iron, as described by Blesa and Matijević (1989):

$$Fe^{3+} \longrightarrow \text{ferrihydrite} \longrightarrow \text{goethite} \longrightarrow \text{hematite} \qquad \text{E.q. 2.5}$$

Ferrihydrite is metastable with respect to goethite and/or hematite. Upon aging, it is transformed progressively to more crystalline phases. Hence, ferrihydrite, goethite and hematite are all supersaturated with respect to ferric ions and Stranski's rule predicts the least stable phase ferrihydrite precipitates first.

As shown in Figure 2.4, the order of solubility of ferrihydrite, goethite and hematite and their initial precipitation rates are given as: S(Fh)>S(Gt)>S(Ht) and $R_{Fh}>R_{Gt}>R_{Ht}$, respectively. According to Stranski's rule, Fh is the least stable phase and forms first at a rate R_{Fh}. Once the concentration of Fe^{3+} drops below the solubility of Fh(S), dissolution of the latter occurs at a rate R_{-Fh}. Solid phase Gt then forms at a rate R_{Gt} from the new created concentration of Fe^{3+} (supersaturation). Phase Gt(s) then dissolves slowly at a rate R_{-Gt} when the concentration conditions favor its dissolution. Similar trends apply to the change from phase Gt(s) to Ht(s).

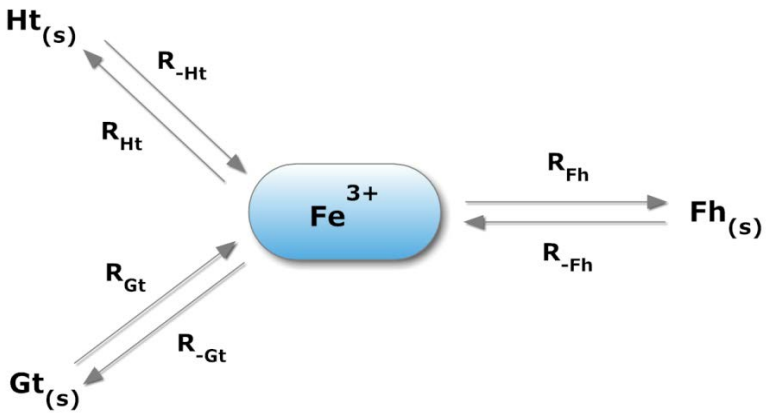

Figure 2.4: Dissolution-recrystallization processes for ferrihydrite (Fh), goethite (Gt) and hematite (Ht) transformation in aqueous solution (After Blesa and Matijević (1989)).

Agglomeration is the major mechanism for growth in precipitation systems dominated by homogeneous nucleation (Demopoulos, 2009). Agglomeration is favored near the point of zero charge (PZC), at higher particle population density and ionic strength (Dirksen and Ring, 1991). Due to the ionization of the surface hydroxyl groups, the aqueous suspensions of insoluble oxides/hydroxides are negatively charged at pH values above the PZC, and positively charged at pH values below the PZC. The charge of the suspended particles is balanced by a layer of ions of the opposite charge (counter ions from the liquid phase), which ensures the interfacial region is electrically neutral. The charged surface, together with the layer of counter ions are arranged in a way that constitutes what is termed the electrical double layer (Cornell and Schwertmann, 2003). Interaction between the electrical double layers of particles is important for agglomeration. The structure study of ferrihydrite aggregates by Lo and Waite (2000) has shown an increase in aggregate size of ferrihydrite particle with increasing time at values close to the PZC (pH 7.8). Primary colloidal ferrihydrite particles between 1 and 7 nm in diameter tend to aggregate together creating ‘bulk’ particles. Background electrolyte concentration also influences aggregate structures, however, mixing effects and apparent destabilization by ferric ions limit the effect of added electrolytes on the stability and

structure of ferrihydrite. The PZC of most iron oxide/hydroxide particles is in the pH range of 6 to 8 (Parks, 1965). Many studies on the synthesis and structure of iron oxide/hydroxides have been conducted at pH values well away from the PZC, and in dilute solutions, in order to investigate primary particles rather than 'bulk' aggregates (Schwertmann and Cornell, 2000).

2.4 NICKEL LOSS DURING IRON PRECIPITATION

It is critical that the iron-bearing precipitates do not contain significant amounts of nickel for an iron removal process to be successfully applied to the nickel laterite PLS. When increasing the pH of an acidic leaching solution, iron and hydroxyl ions tend to form cross-linked three-dimensional networks (Dutrizac, 1987). Rapid growth of these networks results in the formation of an amorphous or poorly defined gelatinous ferrihydrite with poor settling and filtration properties. This precipitate tends to incorporate significant amounts of processing solution in its network structure.

Ferrihydrite has a large specific surface area (200-500 m^2/g) (Cornell and Schwertmann, 2003). Such a precipitate has a strong capacity to collect various elements either by surface adsorption or chemical bonding. For this reason, a direct ferrihydrite precipitation process is less attractive, but is normally used in conjunction with the formation of other iron oxides such as jarosite and goethite. For the formation of jarosite-type compounds, the study by Dutrizac and Dinardo (1983) on lead jarosite has shown that the extent of co-precipitation of nickel with lead-jarosite is small, depending on the synthesis procedure. Up to 2.92% nickel was co-precipitated with lead jarosite through autoclave synthesis (at temperatures ranging from 130 to 180 ºC), but only 0.28% nickel was co-precipitated with lead jarosite by slow-addition synthesis (when lithium carbonate was added slowly to adjust pH in a reaction kettle at 97 ºC). A subsequent study by Dutrizac and Chen (2004) indicated that minor amounts of nickel were structurally incorporated into Na-jarosite, K-

jarosite and NH_4-jarosite when the precipitation reaction was conducted at pH 1.6 and temperatures from 60 to 200 ºC. The extent of incorporation of nickel into the jarosite precipitates increased with increasing concentration of dissolved nickel; increasing concentration of monovalent sulphate salt, and increasing pH and temperature. K-jarosite incorporated more nickel (~1% Ni) than did Na-jarosite or NH_4-jarosite (~0.4% Ni).

In the study of nickel losses associated with goethite formation, an early patent on the E.Z. Goethite Process (Allen *et al.*, 1970) reported that 0.18% nickel remained in the final dried precipitates when the reaction was conducted at 70 °C and pH 2.1 to 2.3. The laboratory study of both the V.M. and E.Z. Goethite Processes by Davey and Scott (1976) indicated respective 1.7% and 0.15% of the total nickel was lost during iron precipitation from the laterite leach liquor at pH 3.5. The recent experimental work on the V.M. process by Chang *et al*. (2010) has shown that 4.1% nickel was lost with the iron precipitation occurring at pH 2.5 to 3.0, whereas 15.9% was lost for iron precipitation at pH 3.0 to 4.0.

The nickel loss associated with iron precipitation is a complicated issue. Normally, nickel hydroxide will also be precipitated above pH 5 (Han *et al*., 1982). In practice, such a high pH value is rarely used in purification processes prior to the recovery of nickel. Conversely, it is well known that co-precipitation and/or adsorption processes occur at a lower pH range than that of simple hydroxide precipitation, although no clear distinction can be made between co-precipitation and adsorption (Benjamin and Leckie, 1981; Crawford *et al*., 1993). Therefore, nickel may not be simply precipitated in the form of nickel hydroxide in a lower pH environment, but is probably incorporated into the precipitates via co-precipitation and/or adsorption. Beukes *et al*. (2000) investigated the adsorption of Ni^{2+} by goethite and hematite in aqueous solution and found that the amount of adsorbed nickel increased with increasing pH from 3 to 8. Notably, nickel was only significantly adsorbed by goethite at pH values greater than 4.

Since there is a low level of nickel normally present in natural or synthetic iron oxide/hydroxide, it is a major challenge to investigate the mechanism of nickel loss by routine characterization techniques, such as X-Ray Diffraction (XRD) and Scanning or Transmission Electron Microscopy (SEM or TEM). One investigation on the incorporation of Ni into natural goethite by X-Ray Absorption Spectroscopy (Carvalho-e-Silva *et al*., 2003) showed that the substitution of Ni for Fe was accompanied by replacement of O^{2-} by OH^{-} to maintain charge neutrality to produce $NiO_2(OH)_4$ octahedra, which had a similar structure to the $FeO_3(OH)_3$ octahedra of pure goethite. Singh *et al*. (2002) made a similar observation for Ni-substitution in synthetic goethite samples. Up to 5 mole % Ni^{2+} was found to substitute for Fe^{3+}.

2.5 PRECIPITATION METHODS

Precipitation reactions can be easily conducted in either batch, semi-batch (semi-continuous) or continuous mode (Figure 2.5). All modes are extensively used in the study of the hydrolysis and precipitation of iron. Each process has its own individual advantages and disadvantages. Batch precipitation is a non-steady-state process. Each batch is a closed system, in which the total mass of the batch is fixed, but the volume and density may vary as the reaction proceeds. Reactant concentrations decrease and product concentrations increase with time. The major advantage of a batch process is the simple equipment and low operational cost. However, a batch reactor is not good from the standpoint of supersaturation control due to the change in reactant concentration and the degree of supersaturation (Demopoulos, 2009; Missen *et al*., 1999).

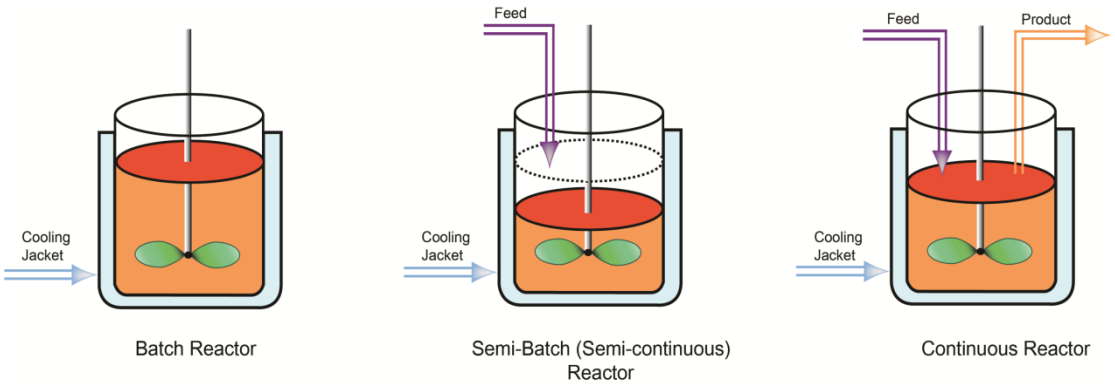

Figure 2.5: Simplified schematic presentations of different reactors for precipitation reactions.

Continuous mode precipitation can be conducted in a continuous stirred-tank reactor (CSTR) that can be arranged in series or parallel. In the continuous precipitation reaction, representative sample data can be obtained only when a steady-state is achieved. At steady-state, the crystal size distribution (CSD), which is often the critical parameter in determining the ease and efficiency of subsequent solid/liquid separation and the stability of the operation, *etc*., can be controlled by the mean residence time and the rate of nucleation and growth (Garside, 1985):

$$n = \left(\frac{B}{G}\right)\exp\left(\frac{-L}{G\tau}\right) \qquad \text{Eq. 2.6}$$

where n is the population density, B is the nucleation rate, G is the growth rate, L is the crystal size, and τ is the mean residence time (τ=reactor volume/flow rate).

Contrary to batch reactor precipitation, continuous precipitation in a CSTR is a steady-state process, hence the nucleation, growth and level of supersaturation can be flexibly controlled by adjusting the flow rate, residence time, *etc*. However, the distinct disadvantages of continuous reactors are the high operational costs and the long times required to reach steady-state.

Semi-batch precipitation (also called semi-continuous) is a process that has

characteristics of both batch and continuous precipitation. In a common semi-batch operation mode, the reactants are added into the reactor over a period of time. Reaction occurs during the addition phase and continues to the point where the yield of the desired product is maximized. A major difference between batch and semi-batch operation is that for the latter, there is a dilution effect due to the additional of reactants (Tsangaris and Baltzis, 1996).

2.6 EXPERIMENTAL STRATEGY

The conventional strategy in studying the effects of various factors during precipitation reactions is to choose a starting point, and change one factor at a time over its range while the others are held constant. After all tests are performed, a set of graphs can be constructed showing how the target value is influenced by each factor with all the other factors kept constant. This “one-factor-at-a-time” approach is widely adopted in research. However, the major disadvantage of this approach is that it fails to consider the possible interactions between factors. These interactions are very common in practice, and if they occur, the “one-factor-at-a-time” approach becomes less efficient compared to the design of experiments (DOE) using statistical methods (Montgomery, 2005). This experimental strategy generally uses a number of experiments in which factors are varied together to study the effects of factors and their possible interactions. Statistically-designed experiments are widely adapted for the studies throughout this thesis and details of these can be found in Chapters 4 to 6.

2.7 SUMMARY

Ferric iron is the major impurity in the pregnant leach solution produced by atmospheric acid leaching of nickel laterite. Effective removal of iron is required to produce pure nickel and cobalt compounds and/or metals during the downstream hydrometallurgical processing of AL laterite leach liquors. This is usually achieved by precipitation but often involves co-precipitation and/or incorporation of nickel

and cobalt.

When choosing a suitable iron removal process for nickel laterite AL system, factors such as the cost of operation, simplicity of equipment, environmental concerns and potential valuable metal losses should all be considered. From the literature survey, the Goethite Process has the advantages of lower capital expenditure over the Hematite Process and generating eco-friendly products relative to the Jarosite Process. The “dilution-precipitation” E.Z Goethite Process is reported to cause less loss of nickel compared to the “reduction-oxidation” V.M. Goethite Process. In addition, E.Z Goethite Process used a semi-batch operation process with simpler equipment and lower capital costs, which makes it a preferred option for processing AL nickel laterite PLS containing significant amounts of ferric iron.

The literature review indicated that the hydrolysis-precipitation of iron as well as the formation and transformation of iron oxides in aqueous solution is quite complicated and not well understood, particularly in acidic media. There seems to be specific conditions for the formation of the precipitates including ferrihydrite, schwertmannite, goethite, hematite, jarosite, *etc*. These compounds form from unique, and as yet unknown, polymerization reactions which change markedly with precipitation conditions. In particular, the higher polymers of iron and sulphate are not well defined, and it is not even certain that the dominant polymer species is closely reproduced in the precipitate formed.

The exact nature of nickel losses associated with iron precipitation is not understood, although it has been suggested by previous studies that nickel loss occurs as either co-precipitation (adsorption) or incorporation into the structure of iron oxides. However, the loss of nickel is found to be closely related to the precipitation factors affecting iron removal such as pH and temperature. This loss shall be minimised by carefully choosing the right combination of the above factors. The changes to these factors can also affect both the chemical (*e.g.* solid composition) and physical properties of the iron-bearing precipitates.

It was concluded that a need exists to extend studies of the effects of various precipitation factors during iron removal upon nickel loss in order to better understand the complicated precipitation behavior of iron oxides and the associated nickel loss mechanism(s). The aspects that require further investigation include: the speciation of iron and nickel species, solubility and precipitation of iron oxides, hydrolysis-precipitation control, co-removal of iron, aluminium and chromium, and mineralogical characterization of the iron-bearing precipitates produced. These identified knowledge gaps are in accord with the aims of this thesis presented in Chapter 1, and will be addressed in each separate chapter.

CHAPTER 3

CHEMICAL MODELLING OF THE Fe(III)-Ni(II)-H_2SO_4-H_2O SYSTEM

3.1 INTRODUCTION

The pregnant leach solution from atmospheric leaching of nickel laterite is rich in various dissolved metals, of which iron is the most abundant. These metals are distributed in aqueous solution as soluble species such as metal ions and, neutral and charged complexes. However, the experimental determination of the speciation in such an aqueous electrolyte solution is difficult, due to the lack of suitable analysis techniques for *in situ* measurement of these species. The chemical modelling of an aqueous electrolyte solution involving different species, particularly at elevated temperatures, can provide a wealth of information that is difficult to obtain from an experimental approach. Thus, modelling of the aqueous electrolyte solution is important to solidify the understanding of the design, analysis and control of the hydrometallurgical process (Liu and Papangelakis, 2005).

Ionic equilibrium and speciation calculations have gained increasing importance in the simulation or modelling of chemical processes. The precipitation product formed by hydrolysis is closely related to the species present at the aqueous solution. Identification of these species becomes of importance in postulating mechanisms which eventually lead to the formation of a precipitation product (Blakey, 1994). Theoretically, given the availability of thermodynamic data for a range of temperatures, the concentration-dependent species in aqueous electrolyte solution can be described as functions of temperatures by solving a group of mathematical equations (Cifuentes *et al.*, 2006). Rafal *et al.* (1995) indicate that phase equilibrium models involving an aqueous phase are generally more difficult to produce than similar models which do not require describing an aqueous phase. Indeed, the main

reasons for the complexity associated with modelling an aqueous solution include: (1) describing the ionic speciation via dissociation, association, hydrolysis and precipitation reactions; (2) the description of the non-ideal behavior of the aqueous solution involving the mean activity coefficient and the different standard state of the aqueous phases, which often requires sound physical-chemistry knowledge to derive the mean activity coefficient models and select reliable thermodynamic data.

Generally, two basic theories are used to describe aqueous solution chemistry and thermodynamics: (a) ion association, and (b) ion interaction. The former tends to describe all the solution non-idealities in terms of various complex formations. This method is based on the ionic strength principle (Johnson and Pytkowicz, 1979), which normally uses equilibrium quotients that only depend on the ionic strength instead of the activity coefficients of ionic species in aqueous solution. The latter, pioneered by Pitzer (Pitzer, 1991), assumes no existence of any complexes or ion association in solution, but interactions between simple ions. The calculation of these interactions is based on virial expansion theory and often requires a fairly large set of interaction coefficients to model a system with great complexity. In addition, one needs to quantify a fairly large number of temperature-dependent parameters describing the physicochemical interactions of all components present in the solution. Unfortunately, there is presently no reliable way to estimate these parameters; instead, these must be fitted to experimentally determined quantities, such as osmotic coefficients (Pitzer, 1991).

In this chapter, the speciation of the mixed ferric and nickel sulphate aqueous system over the pH range from 0 to 4 and temperature from 25 to 100°C is modelled by considering the complex ionic equilibrium reactions and, mass- and charge-balance equations. The Pitzer model is not used due to the complexity described above; instead, a semi-empirical equation based on Debye-Hückel theory with the ionic strength taken into account is used. This equation was initially derived by Vasil'eV (1962), and recently has been utilized by several researchers in various systems

(Filippou *et al.*, 1995; Wang and Breisinger, 1998). From both the experimental and mathematical calculation point of view, it is also convenient to describe the non-ideality of the solution using equilibrium constants which take into account the effect of ionic strength. The speciation model developed can predict the effect of temperature on the concentration distribution of species and estimate the pH values of the system. In addition, the saturation index (SI) for iron oxides such as goethite, ferrihydrite and schwertmannite can be calculated by the model in order to predict whether the selected iron oxide will precipitate or dissolve in a specific solution.

3.2 SOLUTION CHEMICAL MODEL

3.2.1 Specify Fe^{3+} and Ni^{2+} species in sulphuric solutions

The dissociation of electrolytes and formation of complexes occur simultaneously in electrolyte solutions. Casas *et al.* (2000) defined the term “species” as any chemical entity present in solution, *e.g.* ion, complex and molecule; “components” as a minimum number of species that allows complete description of the system. The number of components for a system is constant and given by:

$$N_C = N_S - N_R \qquad \text{Eq. 3.1}$$

where N_C is the number of components, N_S is the number of species and N_R is the number of independent chemical reactions of the solution.

When a simple metal cation enters an aqueous solution, it often reacts with water to form complexes with hydroxide ion (Baes and Mesmer, 1981). This hydrolysis process cannot be simply described as an ionic process, as the metallic cation hydrolyzes usually in a stepwise manner to give a series of soluble species, *e.g.* cations, neutral molecules, or anions. For the solution composition of interest in this study, the important ionic equilibrium reactions include: (a) the hydrolysis reactions of metal ions with H_2O to give hydroxo complexes and protons, (b) the dissociation

of HSO_4^- to give H^+ and SO_4^{2-}, and (c) the formation of complexes between the metallic ions and SO_4^{2-} and between the metallic ions and HSO_4^-. Hence, the ferric and nickel species in a sulphate aqueous solution include: $Fe(OH)_2^+$, $FeOH^{2+}$, $Fe_2(OH)_2^{4+}$, $Fe(OH)_4^-$, $FeHSO_4^{2+}$, $FeSO_4^+$, $Fe(SO_4)_2^-$, $Fe(OH)_3^0$, $Fe_2(SO_4)_3^0$, $NiOH^+$, Ni_2OH^{3+}, $Ni_4(OH)_4^{4+}$, $Ni(OH)_3^-$, $Ni(OH)_4^{2-}$, $Ni(SO_4)_2^{2-}$, $Ni(OH)_2^0$ and $NiSO_4^0$. Other species, such as $FeH(SO_4)_2^0$, $Fe_3(OH)_4^{5+}$, $Ni_3(OH)_3^{3+}$, $Ni_2(OH)_2^{2+}$ and $Ni(OH)_4^{2-}$ are not taken into account, as their existences are still uncertain and less published thermodynamic data are available. The ionic equilibrium reactions and corresponding equilibrium constants in a Fe(III)–Ni(II)–H_2SO_4–H_2O system are given as:

$$H_2O \xleftrightarrow{\beta_0=[H^+][OH^-]} OH^- + H^+ \qquad \text{Eq. 3.2}$$

$$Fe^{3+} + H_2O \xleftrightarrow{\beta_1=\frac{[FeOH^{2+}][H^+]}{[Fe^{3+}]}} FeOH^{2+} + H^+ \qquad \text{Eq. 3.3}$$

$$Fe^{3+} + 2H_2O \xleftrightarrow{\beta_2=\frac{[Fe(OH)_2^+][H^+]^2}{[Fe^{3+}]}} Fe(OH)_2^+ + 2H^+ \qquad \text{Eq. 3.4}$$

$$2Fe^{3+} + 2H_2O \xleftrightarrow{\beta_3=\frac{[Fe_2(OH)_2^{4+}][H^+]^2}{[Fe^{3+}]^2}} Fe_2(OH)_2^{4+} + 2H^+ \qquad \text{Eq. 3.5}$$

$$Fe^{3+} + 4H_2O \xleftrightarrow{\beta_4=\frac{[Fe(OH)_4^-][H^+]^4}{[Fe^{3+}]}} Fe(OH)_4^- + 4H^+ \qquad \text{Eq. 3.6}$$

$$Fe^{3+} + HSO_4^- \xleftrightarrow{\beta_5=\frac{[FeHSO_4^{2+}]}{[Fe^{3+}][HSO_4^-]}} FeHSO_4^{2+} \qquad \text{Eq. 3.7}$$

$$Fe^{3+} + SO_4^{2-} \xleftrightarrow{\beta_6=\frac{[FeSO_4^+]}{[Fe^{3+}][SO_4^{2-}]}} FeSO_4^+ \qquad \text{Eq. 3.8}$$

$$Fe^{3+} + 2SO_4^{2-} \xleftrightarrow{\beta_7=\frac{[Fe(SO_4)_2^-]}{[Fe^{3+}][SO_4^{2-}]^2}} Fe(SO_4)_2^- \qquad \text{Eq. 3.9}$$

$$2Fe^{3+} + 3SO_4^{2-} \xleftrightarrow{\beta_8=\frac{[Fe_2(SO_4)_3^0]}{[Fe^{3+}]^2[SO_4^{2-}]^3}} Fe_2(SO_4)_3^0 \quad \text{Eq. 3.10}$$

$$Fe^{3+} + 3H_2O \xleftrightarrow{\beta_9=\frac{[Fe(OH)_3^0][H^+]^3}{[Fe^{3+}]}} Fe(OH)_3^0 + 3H^+ \quad \text{Eq. 3.11}$$

$$Ni^{2+} + H_2O \xleftrightarrow{\beta_{10}=\frac{[NiOH^+][H^+]}{[Ni^{2+}]}} NiOH^+ + H^+ \quad \text{Eq. 3.12}$$

$$Ni^{2+} + 3H_2O \xleftrightarrow{\beta_{11}=\frac{[Ni(OH)_3^-][H^+]^3}{[Ni^{2+}]}} Ni(OH)_3^- + 3H^+ \quad \text{Eq. 3.13}$$

$$2Ni^{2+} + H_2O \xleftrightarrow{\beta_{12}=\frac{[Ni_2(OH)^{3+}][H^+]}{[Ni^{2+}]^2}} Ni_2OH^{3+} + H^+ \quad \text{Eq. 3.14}$$

$$4Ni^{2+} + 4H_2O \xleftrightarrow{\beta_{13}=\frac{[Ni_4(OH)_4^{4+}][H^+]^4}{[Ni^{2+}]^4}} Ni_4(OH)_4^{4+} + 4H^+ \quad \text{Eq. 3.15}$$

$$Ni^{2+} + 2H_2O \xleftrightarrow{\beta_{14}=\frac{[Ni(OH)_2^0][H^+]^2}{[Ni^{2+}]}} Ni(OH)_2^0 + 2H^+ \quad \text{Eq. 3.16}$$

$$Ni^{2+} + SO_4^{2-} \xleftrightarrow{\beta_{15}=\frac{[NiSO_4{}^0]}{[Ni^{2+}][SO_4^{2-}]}} NiSO_4^0 \quad \text{Eq. 3.17}$$

3.2.2 Bisulphate/sulphate equilibrium and activity of hydrogen ion

There have been many studies on the chemistry of H_2SO_4 solutions (Das, 1988; Dickson *et al.*, 1990; Marshall and Jones, 1966). It is generally believed that the first dissociation reaction of H_2SO_4 to H^+ and HSO_4^- is complete under ambient conditions and sufficiently low concentrations, *i.e.* under the conditions of interested here. As a result, only the dissociation of bisulphate is involved in a solution containing H_2SO_4 and the neutral species $H_2SO_4{}^0$ is not taken into account. The dissociation of bisulphate is given as:

$$HSO_4^- \xleftrightarrow{K_{16}} H^+ + SO_4^{2-} \qquad \text{Eq. 3.18}$$

Dickson *et al.* (1990) studied the molal equilibrium quotients (dissociation constant) of the bisulphate for temperatures up to 250 °C and ionic strength to 5 mol kg^{-1}. An empirical equation containing the Pitzer form of the extended Debye-Hückel term and nine adjustable parameters is given for K_{16}, the dissociation constant expressed as a molal basis (Dickson *et al.*, 1990):

$$\log K_{16}^0 = p_1 + \frac{p_2}{T} + P_3 \ln T + p_4 T + p_5 T^2 \qquad \text{Eq. 3.19}$$

$$\log K_{16} = \log K_1^0 - \frac{4 f^r}{\ln 10} + p_6 \frac{I_m}{T} + F(I_m)\left(p_7 T + \frac{p_8}{T}\right) + p_9 \left(\frac{I_m^2}{T}\right) \qquad \text{Eq. 3.20}$$

$$f^r = -A_\varphi \left[\frac{\sqrt{I_m}}{1 + 1.2\sqrt{I_m}} + \frac{2\ln\left(1 + 1.2\sqrt{I_m}\right)}{1.2} \right] \qquad \text{Eq. 3.21}$$

$$F(I_m) = 1 - (1 + 2\sqrt{I_m})\exp(-2\sqrt{I_m}) \qquad \text{Eq. 3.22}$$

$$\begin{aligned} A_\varphi = {} & 0.322863 + 3.75692 \times 10^{-4}\, t + 2.55932 \times 10^{-6}\, t^2 - 9.96273 \times 10^{-11}\, t^3 \\ & + 5.98066 \times 10^{-3} \exp\left(\frac{t - 270}{10}\right) + \frac{1.39987 \times 10^{-2}}{t + 20} + \frac{18.4374}{315 - t} - \frac{554.596}{(315 - t)^2} \\ & + \frac{7684.77}{(315 - t)^3} - \frac{54091}{(315 - t)^4} + \frac{154381}{(315 - t)^5} \end{aligned} \qquad \text{Eq. 3.23}$$

where T is absolute temperature (K), t refers to the temperature in degree Celsius (°C), I_m is the molal ionic strength. The relevant parameters in Dickson's equations are listed in Table 3.1.

Table 3.1: p parameters in Dickson's formulas (Dickson *et al.*, 1990).

p_1=562.7097	p_2= –13273.75	p_3= –102.5154
p_4=0.2477538	p_5= -1.117033×10^{-4}	p_6= –57.07583
p_7= -1.144759×10^{-3}	p_8=46.72816	p_9=2.499849

In Dickson's empirical equations, K_{16}^0 refers to the thermodynamic equilibrium constant and K_{16} represents the dissociation constant expressed on a molal basis:

$$K_{16}^0 = \frac{a_{H^+} \cdot a_{SO_4^{2-}}}{a_{HSO_4^-}} \qquad \text{Eq. 3.24}$$

$$K_{16} = \frac{m_{H^+} \cdot m_{SO_4^{2-}}}{m_{HSO_4^-}} \qquad \text{Eq. 3.25}$$

The relationship between the equilibrium constant of the bisulphate (HSO_4^-) on a molar basis, β_{16}, and molal basis, K_{16}, is given as (Filippou *et al.*, 1995):

$$\beta_{16} = \frac{[HSO_4^-]}{[H^+][SO_4^{2-}]} = \frac{1/K_{16}}{\rho - 0.001\sum_{i=1}^{n} c_i M_i} \qquad \text{Eq. 3.26}$$

where c_i is the molarity concentration of the species i (mol/L), M_i is the molecular weight of the same species in g/mol, ρ is the density of solution in kg/L. Similarly, the following equations are used to make the interconversion between molarity and molality:

$$m_i = \frac{c_i}{\rho - \sum_{i=1}^{n} c_i M_i} \qquad \text{Eq. 3.27}$$

$$c_i = \frac{m_i \rho}{1 + \sum_{i=1}^{n} m_i M_i} \qquad \text{Eq. 3.28}$$

For simplicity, the density of the solution is assumed to be equal to that of pure water at the temperature of interest. An empirical equation for water density as a function of temperature, which is devised by Tödheide (1972), is given as:

$$\rho = 15.81747 + 9.87802T - 0.035239T^2 + \left(5.38051\times10^{-5}\right)T^3 - \left(3.2612\times10^{-8}\right)T^4$$

Eq. 3.29

where T is expressed in K, and ρ is in kg/m^3.

3.2.3 Calculation of pH value of solution

The pH value is the master variable in hydrometallurgy processing. The change of pH value of solution greatly influences the interaction of species in aqueous electrolyte solutions. Strictly speaking, the concentration of [H^+] cannot accurately describe the actual pH value of solutions which is defined as a logarithm of hydrogen ion activity rather than hydrogen ion concentration (Galster, 1991). Filippou *et al.* (1995) indicated that the activity of H^+ differs greatly from its analytical concentration, and the experimental measurement of pH value is actually a relative indicator of acidity (or alkalinity). The activity of hydrogen ions is defined as $a_{H^+} = m_{H^+}\cdot\gamma_{H^+}$. Hence, to estimate the hydrogen ion activity in sulphuric acid solutions, one needs to know the single hydrogen ion activity coefficient (γ_{H^+}). Das (1988) devised an approach to estimate this single ion activity in aqueous sulphuric acid solutions, of which the activity coefficient of the hydrogen ion in sulphuric solution is expressed by an extended Debye-Hückel equation:

$$\log\gamma_{H^+} = -\frac{A\sqrt{I_m}}{1+5.66B\sqrt{I_m}} + 0.04785I_m - \log\left(1+\frac{0.018\sum_{i=1}^{n}m_i}{1-0.018hm_{H^+}}\right)$$

Eq. 3.30

where A and B are the Debye-Hückel constants depending on the temperature and dielectric constant of solvent. Manov *et al*. (1943) compiled the values of A and B for aqueous solution over the temperature range from 0 to 100°C based on both molar and molal expressions of ionic strength. The hydration number for the hydrogen ion, h, is accepted to be 4 (Das, 1988).

3.2.4 Equilibrium constants as a function of ionic strength

Vasil'eV (2004) suggested that the thermodynamic equilibrium constant, β^0 (molar basis), is independent of the concentration. The thermodynamic equilibrium constant is an essential thermodynamic characteristic of complexation which is related to the change of standard Gibbs free energy in a known equation of the reaction isotherm; while the concentration equilibrium constant, β_T (molar basis), generally depends on the concentration of the species in solution, which is crucial for calculating ionic equilibrium in a specific solution of a given ionic strength. Vasil'eV (1962) derived a semi-empirical equation to obtain the concentration equilibrium constant (β_T) from the thermodynamic constant (β_T^0), which is also a function of ionic strength. This equation is given by (Vasil'eV, 1962):

$$\log\beta_T = \log\beta_T^0 + \frac{A\Delta z^2\sqrt{I_c}}{1+1.6\sqrt{I_c}} + bI_c \qquad \text{Eq. 3.31}$$

where Δz^2 is the difference of charges of species multiplied by the corresponding stoichiometric coefficient, A is the Debye-Hückel constant, I_c is the ionic strength (molar basis), and b is the constant that describe the characteristic of reaction. Notably, if $I_c=0$, $\beta_T^0 = \beta_T$. That is the use of thermodynamic equilibrium constant for calculation of ionic equilibrium gives satisfactory results only for very dilute solutions.

Table 3.2: Equilibrium constant of water and iron species for different media and ionic strength at 25°C.

Species	logK	Medium	Reference
H_2O	–15.60	4.5 M $[(CH_3)_4N]Cl$	(a)
	–14.69	3 M $[(CH_3)_4N]Cl$	(a)
	–14.08	1.5 M $[(CH_3)_4N]Cl$	(a)
$FeHSO_4^{2+}$	0.30	4 M $NaClO_4$	(b)
	0.48	2.67 M $NaClO_4$	(c)
	0.78	1.2 M $NaClO_4$	(d)
$FeSO_4^{+}$	1.92	2.67 M $NaClO_4$	(c)
	2.04	2 M $NaClO_4$	(c)
	2.12	1.2 M $NaClO_4$	(e)
$Fe(SO_4)_2^{-}$	2.9	0.6 M $NaClO_4$	(f)
	3.32	0.2 M $NaClO_4$	(f)
	3.65	0.1 M $NaClO_4$	(b)
$FeOH^{2+}$	–2.79	1.0 M $NaClO_4$	(g)
	–2.72	0.5 M $NaClO_4$	(g)
	–2.66	0.25 M $NaClO_4$	(g)
$Fe(OH)_2^{+}$	–6.3	3 M $NaClO_4$	(h)
	–6.21	1 M $NaClO_4$	(h)
	–5.9	0.1 M $NaClO_4$	(i)
$Fe_2(OH)_2^{4+}$	–2.81	3 M $NaClO_4$	(j)
	–2.89	1 M $NaClO_4$	(j)
	–2.92	0.1 M $NaClO_4$	(j)
$Fe(OH)_4^{-}$	–21.8	0.1 M NaCl	(k)
	–22.7	0.7 M NaCl	(k)
	–24.3	5.0 M NaCl	(k)
$Fe(OH)_3^{0}$	–15	0.1 M NaCl	(l)
	–15	0.7 M NaCl	(l)
	–16	5.0 M NaCl	(l)

Note: (a) Sipos et al. (1997); (b) Martell and Smith (1977); (c) Sapieszko et al. (1977); (d) Lister and Rivington (1955); (e) Cavasino (1968); (f) Dousma et al. (1979); (g) Baes and Mesmer (1976); (h) Byrne et al. (2000); (i) Daniele et al.

(1994); (j) Stefánsson (2007); (k) Millero and Pierrot (2007); (l) Liu and Millero (1999).

The parameter b in Eq. 3.31 can be determined from the slope by plotting the quantity:

$$Y = \log\beta_T - \log\beta_T^0 + \frac{A\Delta z^2\sqrt{I_c}}{1+1.6\sqrt{I_c}} \qquad \text{Eq. 3.32}$$

against ionic strength I_c. Table 3.2 lists the equilibrium constants of water and iron species at various ionic strengths from the literature for the estimation of the parameter b. Table 3.3 shows the b values obtained from linear regression of the data listed in Table 3.2 using Eq. 3.32.

Table 3.3: b values for the Vasil'eV equation.

Species	Parameter b	Squared correlation coefficient (R^2)
H_2O	–0.5176	0.9926
$FeHSO_4^{2+}$	–0.0864	0.9981
$FeSO_4^{+}$	0.1439	0.9857
$Fe(SO_4)_2^{-}$	0.7036	0.9989
$FeOH^{2+}$	0.1105	0.9282
$Fe(OH)_2^{+}$	0.1151	0.8819
$Fe_2(OH)_2^{4+}$	0.0383	0.9983
$Fe(OH)_4^{-}$	–0.3633	0.9624
$Fe(OH)_3^{0}$	0.3581	0.9848

As the values of β vs. I_c are not available for the neutral species $Fe_2(SO_4)_3^0$, the value of b could not be determined by Eq. 3.32. The concentration equilibrium constant of this species was determined by using an equation derived by Papangelakis *et al.* (2004):

$$\log\beta_T = 1.5293 - \frac{9.905\sqrt{I_c}}{1+1.6\sqrt{I_c}} + 0.0294 I_c \qquad \text{Eq. 3.33}$$

Baes and Mesmer (1976) used a similar equation to describe the nickel hydroxo species including $NiOH^+$, $Ni(OH)_2{}^0$, $Ni(OH)_3{}^-$, Ni_2OH^{3+} and $Ni_4(OH)_4{}^{4+}$:

$$\log\beta_T = \log\beta_T^0 + \frac{\alpha_1\sqrt{I_c}}{1+\sqrt{I_c}} + \alpha_2 \qquad \text{Eq. 3.34}$$

where α_1 and α_2 are constants. For the neutral nickel sulphate $NiSO_4{}^0$, the equation developed by Kenttämaa (1958) is employed:

$$\log\beta_T = \log\beta_T^0 + \frac{3.9\sqrt{I_c}}{1+\delta_1\sqrt{I_c}} - \delta_2 I_c \qquad \text{Eq. 3.35}$$

where δ_1 and δ_2 are constants. Table 3.4 lists the values of α_1 and α_2 in Eq. 3.34 and δ_1 and δ_2 in Eq. 3.35

Table 3.4: Parameters in Eqs. 3.34 and 3.35 (sourced from Kenttämaa (1958) and Baes and Mesmer (1976)).

Species	α_1	α_2	δ_1	δ_2
$NiOH^+$	–1.022	0.15		
$Ni(OH)_2{}^0$	–1.022	0.05		
$Ni(OH)_3{}^-$	0	–0.21		
Ni_2OH^{3+}	1.022	0		
$Ni_4(OH)_4{}^{4+}$	2.044	–0.26		
$NiSO_4{}^0$			2.22	–0.32

3.2.5 Extrapolation to elevated temperature

The determination of ionic speciation at elevated temperatures is more challenging. It depends on reliable thermodynamic data and the extrapolation method, *i.e.* the accuracy of the model at elevated temperature will strongly depend on the accuracy

of the equilibrium constant value and the extrapolation of it to elevated temperature.

The thermodynamic equilibrium constant at temperature T can be obtained from the changes of standard Gibbs free energy ΔG_T^0:

$$\Delta G_T^0 = -RT\ln\beta_T^0 \qquad \text{Eq. 3.36}$$

where R is the universal gas constant (8.314 J/mol·K), T is the temperature in Kelvin (K). The value of ΔG_T^0 can be obtained at temperatures higher than 298K when the standard entropy change of the reaction at 298K (ΔS_{298}^0) and the corresponding heat capacity (ΔC_p^0) are known:

$$\Delta G_T^0 = \Delta G_{298}^0 + \int_{298}^{T} \Delta C_p^0 \, dT - (T - 298)\Delta S_{298}^0 - T\int_{298}^{T} \frac{\Delta C_p^0}{T} dT \qquad \text{Eq. 3.37}$$

However, the values of heat capacity for some species participating in equilibrium reactions are not always available. In such cases, extrapolation to calculate the temperature-dependent thermodynamic properties for aqueous ions becomes important. The well-known approaches include the van't Hoff isochore (Burkin, 2001), the Criss-Cobble entropy correspondence principle (Criss and Cobble, 1964a; 1964b) and Helgeson's extrapolation (Helgeson, 1967). According to the van't Hoff isochore, the enthalpy of the reaction, ΔH^0, is assumed to be constant over the temperature range. This assumption on constant enthalpy is equivalent to neglecting the effect of heat capacity. Thus, the van't Hoff isochore is strictly valid only at low concentration and over a small temperature range. For the Criss-Cobble method (Criss and Cobble, 1964a; 1964b), the heat capacity is assumed to be constant instead of zero. However, some researchers (Blakey and Papangelakis, 1996; Liu and Papangelakis, 2005) indicated that the main limitation of Criss and Cobble's method is the lack of model parameters for certain species, such as neutral species and metal oxyanions. Alternatively, Helgeson (1967) assumed that the ratio of heat capacity change at reference temperature ($\Delta C_{p,r}^0(T)$) to the electrostatic contribution to the

heat capacity change ($\Delta C_{p,e}{}^{0}(T)$) is constant. This assumption gives fairly good accuracy at temperatures below 150°C. Above this temperature limit, the influence of the electrostatic contribution becomes strong, as the dielectric constant of water decreases with increasing temperature. Based on this assumption, an approximation of the equilibrium constant at any given temperature below 150°C can be estimated by the following Helgeson equation (Jackson and Helgeson, 1985):

$$\log\beta_T^0 = \frac{\Delta S_{298.15}^0}{2.303RT}\left\{298.15 - \frac{\theta_1}{\theta_2}\left[1 - \exp\left(\exp(\theta_3 + \theta_4 T) + \theta_5 + \frac{T - 298.15}{\theta_1}\right)\right]\right\} - \frac{\Delta H_{298.15}^0}{2.303RT}$$

Eq. 3.38

The θ in the Eq. 3.38 represent the temperature-independent constants: θ_1=219, θ_2=1.003229, θ_3=−12.741, θ_4=0.01875, and θ_5=−0.000784. Table 3.5 lists the thermodynamic data that was used to estimate the required equilibrium constants.

Table 3.5: Species and thermodynamic data for Fe(III)–Ni(II)–H_2SO_4–H_2O system.

Species	$\Delta G_{f,298}^0$ kJ mol^{-1}	S_{298}^0 J mol^{-1}K^{-1}	$\Delta H_{f,298}^0$ kJ mol^{-1}	Reference
H^+	0	0	0	(a)
OH^-	–157.29	–10.88	–230.12	(a)
H_2O	–237.18	69.96	–285.85	(a)
SO_4^{2-}	–744.63	20.08	–909.18	(a)
HSO_4^-	–756.01	131.8	–887.01	(a)
Fe^{3+}	–4.6	–315.9	–48.5	(b)
$FeOH^{2+}$	–229.41	–142	–290.8	(b)
$Fe(OH)_2^+$	–446.4	–29.29	–543.8	(b)
$Fe_2(OH)_2^{4+}$	–466.97	–355.64	–611.38	(b)
$Fe(OH)_4^-$	–830	25.5	–1050.4	(a)
$Fe(OH)_3^0$	–660	75.4	–795.73	(a)
$Fe_2(SO_4)_3^0$	–2243	–571.53	–2825.04	(a)
$FeSO_4^+$	–772.8	–129.7	–931.78	(b)
$Fe(SO_4)_2^-$	–1524.65	–43.07	–1828.39	(b)
$FeHSO_4^{2+}$	–768.38	–18.68	–894.29	(a)
Ni^{2+}	45.5	–130	–54.1	(c)
$Ni(OH)_2^0$	–417	–48	–540	(c)
$NiOH^+$	–228.4	–74	–290	(c)
$Ni(OH)_3^-$	–587	–85	–791	(c)
Ni_2OH^{3+}	–272	–260	–359	(c)
$Ni_4(OH)_4^{4+}$	–971	–203	–1190	(c)
$NiSO_4^0$	–803.3	–18	–949.3	(d)

Note: The thermodynamics data sourced from (a) Filippou et al. (1995); (b) Papangelakis and Demopoulos (1990); (c) Plyasunova (1998); (d) Liu and Papangelakis (2005).

3.2.6 Saturation index

The dissolution and precipitation equilibrium between a sparingly soluble iron oxide and the concentration of its ions in a saturated solution are often described by the solubility product (K_{so}) (Cornell and Schwertmann, 2003). Take the dissolution of goethite in water as an example:

$$FeOOH + H_2O \longleftrightarrow Fe^{3+} + 3OH^- \qquad \text{Eq. 3.39}$$

At equilibrium, the solubility product is given by:

$$K_{so} = a_{Fe^{3+}} \cdot a^3_{OH^-} \qquad \text{Eq. 3.40}$$

where $a_{Fe^{3+}}$ and a_{OH^-} are the activities of Fe^{3+} and OH^-, respectively. In an acid solution, Eq.3.39 is often described as:

$$FeOOH + 3H^+ \longleftrightarrow Fe^{3+} + 2H_2O \qquad \text{Eq. 3.41}$$

The corresponding solubility product is given by:

$$K^*_{so} = a_{Fe^{3+}} \cdot a^{-3}_{H^+} \qquad \text{Eq. 3.42}$$

Comparison of Eqs 3.40 and 3.42, K_{so} and K^*_{so} has the relationship:

$$K_{so} = K^*_{so} \cdot K^3_W \qquad \text{Eq. 3.43}$$

where K_w is the ion product of water. The value of K_w depends on ionic strength and temperature. At 25 ºC and in low ionic strength solution, $\log K_w$ =13.99 (Cornell and Schwertmann, 2003).

Table 3.6 tabulates the reported solubility products of goethite, ferrihydrite and schwertmannite. Notably, the general trend in solubility follows the order:

schwertmannite>ferrihydrite>goethite.

Table 3.6: Solubility products of goethite, ferrihydrite and schwertmannite [§].

Mineral	Reaction	Solubility products	x value	[†]
Gt	$FeOOH + 3H^+ \longleftrightarrow Fe^{3+} + 2H_2O$	***–38.7±0.2 ($logK_{so}$)*** [ξ]		(a)
		–0.02 ($logK^*_{so}$)		(b)
		–40.83 ($logK_{so}$)		(c)
		1.4±0.1 ($logK^*_{so}$)		(d)
		–42.4±0.4 ($logK_{so}$)		(e)
Fh	$Fe(OH)_3 + 3H^+ \longleftrightarrow Fe^{3+} + 3H_2O$	***–39.02±0.35 ($logK_{so}$)*** [ξ]		(f)
		4.3 ($logK^*_{so}$)		(g)
		–37.7 ($logK_{so}$)		(e)
		4.3±0.5 ($logK^*_{so}$)		(h)
		4.28±0.5 ($logK^*_{so}$)		(i)
		–31.7 ($logK_{so}$)		(j)
Sh	$Fe_8O_8(OH)_{8-2x}(SO_4)_x + (24-2x)H^+ \longleftrightarrow 8Fe^{3+} + xSO_4^{2-} + (16-2x)H_2O$	***18.0±2.5 ($logK^*_{so}$)*** [ξ]	x=1.6	(d)
		10.5±2.5 ($logK^*_{so}$)	1.74≤x≤1.86	(h)
		7.06±0.09 ($logK^*_{so}$)	x=1.05	(k)
		9.6±4.0 ($logK^*_{so}$)	x=1	(l)
		18.8±1.7 (log^*K_{so})	1.40≤x≤1.50	(m)

Note: [§] All solubility products were measured at 25 ºC, otherwise the experimental conditions were noted. Gt=goethite; Fh=ferrihydrite; Sh=Schwertmannite; [ξ] Adapted for SI calculation in this chapter; [†](a) Bienermann and Schindler (1957), background electrolyte 3 M $NaClO_4$; (b) Lindsay (1979), calculated from ΔG_f; (c) Hsu and Marion (1985), ageing $Fe(ClO_4)_3$ solutions, ionic strength 0.2 M ; (d) Bigham et al., (1996) solubility product of goethite was measured by schwertmannite dissolution over a period of 543 days; (e) Diakonov (1998), calculated from ΔG_f ; (f) Vlek et al. (1974), measured by EDTA complexation; (g) Byrne and Kester (1976), in seawater with 3.62% salinity; (h) Yu et al. (1999), geochemical modeling of AMD waters at

15 ºC; (i) Byrne and Luo (2000), in 0.7 M $NaClO_4$ solutions; (j) Fox (1988), derived both from measurements of dissolved ferric ion over a pH range from 2.5 to 6.7 and electrochemical values reported in the literature; (k) Kawano and Tomita (2001), dissolution of aged natural samples at 30 ºC; (l) Majzlan et al. (2004), calculated from ΔG_f; (m) Sánchez-España et al (2011), titration of pit lake waters.

Saturation index (SI) is the logarithm of the quotient of the ion activity product (IAP) and solubility product (K_{so}) (Appelo and Postma, 2005):

$$SI = \log \frac{IAP}{K_{so}} \qquad \text{Eq. 3.44}$$

where IAP is the product of free ion species activity that is determined from analytical concentrations by considering ionic strength, temperature and complex formation (Appelo and Postma, 2005).

For dissolution-precipitation equilibrium, Gibbs free energy (ΔG) is given by:

$$\Delta G = -\frac{RT}{n} \cdot \ln \frac{IAP}{K_{so}} = -\frac{2.303RT}{n} \cdot SI \qquad \text{Eq. 3.45}$$

When SI=0, ΔG=0, the solution is in equilibrium; when SI<0, ΔG>0, the solution is undersaturated; when SI>0, ΔG<0, the solution is saturated.

The activity of ion species is expressed as the product of ion concentration and its activity coefficient. The activity coefficients of ferric and sulphate ions during SI calculation in this chapter are determined by Davies equation (Davies, 1962):

$$\log \gamma_i = -AZ_i^2 \left(\frac{\sqrt{I_m}}{1+\sqrt{I_m}} - 0.3 I_m \right) \qquad \text{Eq. 3.46}$$

where γ_i is the activity coefficient, A is the Debye-Hückel constant, Z_i is the charge of ion i , I_m is the ionic strength on a molal basis.

3.3 RESULTS AND DISSCUSION

3.3.1 Solving the model equations

Table 3.7: List of chemical species in Fe(III)–Ni(II)–H_2SO_4–H_2O system.

H^+	Fe^{3+}	$Fe(OH)_4^-$	$Fe(OH)_3^0$	$Ni(OH)_3^-$	$NiSO_4^0$
OH^-	$FeOH^{2+}$	$Fe(SO_4)_2^-$	$Fe_2(SO_4)_3^0$	Ni_2OH^{3+}	
SO_4^{2-}	$Fe(OH)_2^+$	$FeSO_4^+$	Ni^{2+}	$Ni_4(OH)_4^{4+}$	
HSO_4^-	$Fe_2(OH)_2^{4+}$	$FeHSO_4^{2+}$	$NiOH^+$	$Ni(OH)_2^0$	

In the Fe(III)–Ni(II)–H_2SO_4–H_2O system, there are 21 species which are given in Table 3.7. In order to determine the concentration of these 21 species, a system of 21 equations with 21 unknown variables needs to be solved. The equations of this system include 17 ionic equilibrium equations (Eqs. 3.2-3.18) and another 4 equations given as follows:

(I) The ferric iron mass balance:

$$[Fe^{3+}]_{Total} = [Fe^{3+}] + [FeOH^{2+}] + [Fe(OH)_2^+] + 2[Fe_2(OH)_2^{4+}] + [Fe(OH)_4^-] + [FeSO_4^+] + [Fe(SO_4)_2^-] + [FeHSO_4^{2+}] + [Fe(OH)_3^0] + 2[Fe_2(SO_4)_3^0]$$

Eq. 3.47

(II) The nickel mass balance:

$$[Ni^{2+}]_{Total} = [Ni^{2+}] + [NiOH^+] + [Ni(OH)_3^-] + 2[Ni_2(OH)^{3+}] + 4[Ni_4(OH)_4^{4+}] + [Ni(OH)_2^0] + [NiSO_4^0]$$

Eq. 3.48

(III) The sulphate mass balance:

$$[SO_4^{2-}]_{Total} = [SO_4^{2-}] + [FeSO_4^+] + 2[Fe(SO_4)_2^-] + [FeHSO_4^{2+}] + 3[Fe_2(SO_4)_3^0] + [HSO_4^-] + [NiSO_4^0]$$

Eq. 3.49

(IV) The charge balance:

$$3[Fe^{3+}] + 2[FeOH^{2+}] + [Fe(OH)_2^+] + 4[Fe_2(OH)_2^{4+}] + [FeSO_4^+] + 2[FeHSO_4^{2+}] + 2[Ni^{2+}] + [NiOH^+] + 3[Ni_2OH^{3+}] + 4[Ni_4(OH)_4^{4+}] + [H^+] = [Fe(OH)_4^-] + [Fe(SO_4)_2^-] + [Ni(OH)_3^-] + [OH^-] + [HSO_4^-] + 2[SO_4^{2-}]$$

Eq. 3.50

The 21 species in the Fe(III)–Ni(II)–H_2SO_4–H_2O system can be further reduced to four key components (Fe^{3+}, Ni^{2+}, SO_4^{2-} and H^+), *i.e.* other species can all be described by these "building blocks". If the concentrations of all these key components are known, the concentration of any other species can be calculated. For instance, the concentrations of OH^- and $Fe(OH)_2^+$ can be described as:

$$OH^- = \beta_0[H^+]^{-1}$$ Eq. 3.51

$$FeOH^{2+} = \beta_0\beta_1[Fe^{3+}][H^+]^{-1}$$ Eq. 3.52

Eqs. 3.46 to 3.49 can be rearranged as:

$$[Fe^{3+}]_{Total} - [Fe^{3+}] - \beta_1[Fe^{3+}][H^+]^{-1} - \beta_2[Fe^{3+}][H^+]^{-2} - 2\beta_3[Fe^{3+}]^2[H^+]^{-2} - \beta_4[Fe^{3+}][H^+]^{-4} - \beta_6[Fe^{3+}][SO_4^{2-}] - \beta_7[Fe^{3+}][SO_4^{2-}]^2 - \beta_5\beta_{16}[Fe^{3+}][H^+][SO_4^{2-}] - \beta_9[Fe^{3+}][H^+]^{-3} - 2\beta_8[Fe^{3+}]^2[SO_4^{2-}]^3 = 0$$

Eq. 3.53

$$[Ni^{2+}]_{Total} - [Ni^{2+}] - \beta_{10}[Ni^{2+}][H^+]^{-1} - \beta_{11}[Ni^{2+}][H^+]^{-3} - 2\beta_{12}[Ni^{2+}]^2[H^+]^{-1} - 4\beta_{13}[Ni^{2+}]^4[H^+]^{-4} - \beta_{14}[Ni^{2+}][H^+]^{-2} - \beta_{15}[Ni^{2+}][SO_4^{2-}] = 0$$

Eq. 3.54

$$[SO_4^{2-}]_{Total} - [SO_4^{2-}] - \beta_6[Fe^{3+}][SO_4^{2-}] - 2\beta_7[Fe^{3+}][SO_4^{2-}]^2 - \beta_5\beta_{16}[Fe^{3+}][H^+][SO_4^{2-}] - 3\beta_8[Fe^{3+}]^2[SO_4^{2-}]^3 - \beta_{16}[H^+][SO_4^{2-}] - \beta_{15}[Ni^{2+}][SO_4^{2-}] = 0$$

Eq. 3.55

$$3[Fe^{3+}] + 2\beta_1[Fe^{3+}][H^+]^{-1} + \beta_2[Fe^{3+}][H^+]^{-2} + 4\beta_3[Fe^{3+}]^2[H^+]^{-2} + \beta_6[Fe^{3+}][SO_4^{2-}] + 2\beta_5\beta_{16}[Fe^{3+}][H^+][SO_4^{2-}] + 2[Ni^{2+}] + \beta_{10}[Ni^{2+}][H^+]^{-1} + 3\beta_{12}[Ni^{2+}]^2[H^+]^{-1} + 4\beta_{13}[Ni^{2+}]^4[H^+]^{-4} + [H^+] - \beta_4[Fe^{3+}][H^+]^{-4} - \beta_7[Fe^{3+}][SO_4^{2-}]^2 - \beta_{11}[Ni^{2+}][H^+]^{-3} - \beta_0[H^+]^{-1} - \beta_{16}[H^+][SO_4^{2-}] - 2[SO_4^{2-}] = 0$$

Eq. 3.56

Eqs. 3.53-3.56 are non-linear equations containing only four key components (Fe^{3+}, Ni^{2+}, SO_4^{2-} and H^+). In order to solve these non-linear equations, a Microsoft® Visual C++ computer program was written that utilized the Newton-Raphson method (Albarède, 1995). The complete computer program is given in Appendix A. The conceptual flowchart of this calculation procedure is described in Figure 3.1.

The initial assumption is that all the electrolytes are completely dissociated, thus only Fe^{3+}, Ni^{2+}, SO_4^{2-} and H^+ ions exist in the aqueous solution. Guess and input the initial values of those species:

$$[H^+] = 2[H_2SO_4]_{free} = 2\left([SO_4^{2-}]_{total} - \frac{3}{2}[M_i^{z_i+}]\right) = 2\left([SO_4^{2-}]_{total} - [Ni^{2+}]_{total} - \frac{3}{2}[Fe^{3+}]_{total}\right)$$

Eq. 3.57

$$[SO_4^{2-}]^0 = [SO_4^{2-}]_{total} \quad \text{Eq. 3.58}$$

$$[Ni^{2+}]^0 = [Ni^{2+}]_{total} \quad \text{Eq. 3.59}$$

$$[Fe^{3+}]^0 = [Fe^{3+}]_{total} \quad \text{Eq. 3.60}$$

In terms of Eq. 3.56, the hydrogen ion is assumed to only come from the free acid corresponding to the total sulphate minus that bound to metals, stoichometrically assuming simply sulphate (Rubisov and Papangelakis, 2000). Based on the initial input values of the key components, the initial ionic strength on a molar basis, I_c^0, can be calculated accordingly:

$$I_c^0 = \frac{1}{2}\sum_{i=1}^{n} c_i z_i^2 = \frac{1}{2}([H^+]^0 + 4[SO_4^{2-}]^0 + 4[Ni^{2+}]^0 + 9[Fe^{3+}]^0) \quad \text{Eq. 3.61}$$

After solving the nonlinear equations (Eqs. 3.53-3.56), the new concentrations of Fe^{3+}, Ni^{2+}, SO_4^{2-} and H^+ ions can be obtained. The concentrations of various species can also be obtained according to the corresponding equilibrium reactions. When a complete set of concentration values was obtained, the new ionic strength, I_c, can then be calculated:

$$\begin{aligned} I_c = \frac{1}{2}\sum_{i=1}^{n} c_i z_i^2 = \frac{1}{2}([H^+] + [OH^{-1}] + 4[SO_4^{2-}] + [HSO_4^-] + 4[Ni^{2+}] + 9[Fe^{3+}] \\ + 4[FeOH^{2+}] + [Fe(OH)_2^+] + 16[Fe_2(OH)_2^{4+}] + [Fe(OH)_4^-] + 4[FeHSO_4^{2+}] \\ + [FeSO_4^+] + [Fe(SO_4)_2^-] + [NiOH^+] + [Ni(OH)_3^-] + 9[Ni_2OH^{3+}] + 16[Ni_4(OH)_4^{4+}]) \end{aligned} \quad \text{Eq. 3.62}$$

The accuracy of the calculated model is evaluated by comparing the new obtained I_c to the initial I_c^0. The final calculation for hydrogen ion activity and pH value of the system are conducted only when the relative error of those two ionic strengths is within an acceptable level.

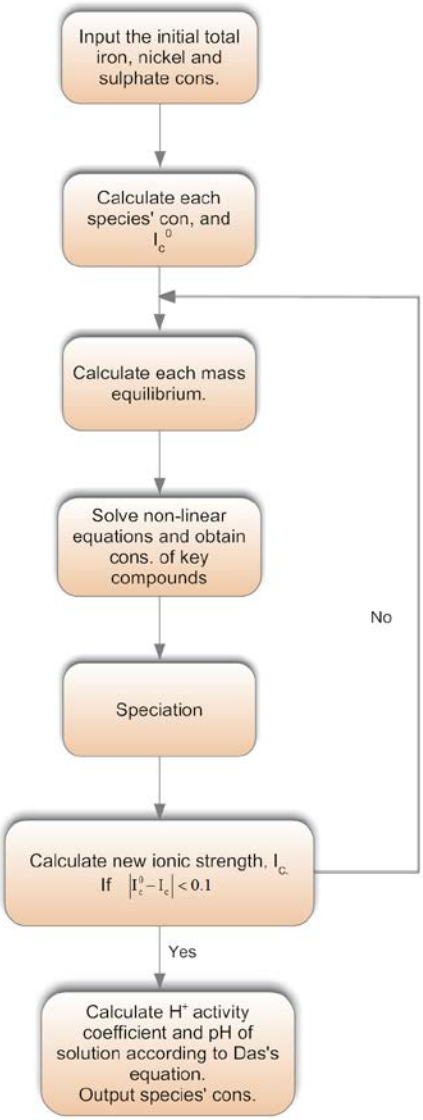

Figure 3.1: Flowchart of the calculation procedures.

3.3.2 Ferric iron and nickel speciation

Figures 3.2 and 3.3 show the calculated concentration distribution of iron and nickel species over the pH range from 0 to 4 at 25 ºC, respectively. The simulated solution contains 0.015 mol ferric iron and 0.0025 mol nickel ions. This gives a Fe/Ni ratio of 6, which is the primary Fe/Ni ratio for the atmospheric nickel laterite leach solutions investigated throughout this thesis. The precipitation processes studied in the subsequent chapters, however, involve high concentrations of ferric iron and nickel ions. To some extent, this can be considered as the orders of magnitude of the simulated low concentration conditions.

The pH value of solution is adjusted by varying the total sulphate concentration. The mole fraction, represented on the Y axis, refers to the ratio of the concentration of each iron or nickel species to the total concentration of iron or nickel.

As shown in Figure 3.2, the ferric sulphate species $Fe(SO_4)_2^-$ and $FeSO_4^+$ are dominant in highly acidic solution. The concentration of the $Fe(SO_4)_2^-$ species drops steeply with increasing pH values from 0 to 4. The concentration of $FeSO_4^+$ rises rapidly and becomes the dominant species with a maximum fraction of about 78% over the pH range from 1 to 2, and drops rapidly at pH values above 2.5. The amount of ferric hydroxo species, $FeOH^{2+}$, $Fe(OH)_2^+$, $Fe_2(OH)_2^{4+}$, $Fe(OH)_4^-$ and $Fe(OH)_3^0$ are negligible at pH values below 2. At pH values above 3, a considerable amount of $FeOH^{2+}$, $Fe(OH)_2^+$ and $Fe(OH)_3^0$ species are predicted. Concentrations of $FeOH^{2+}$, $Fe(OH)_2^+$ and $Fe(OH)_3^0$ hydroxo species are closely related to the proton concentration in terms of the hydrolysis reactions (Eqs. 3.3, 3.4 and 3.11). As the concentration of hydrogen ion decreases, these hydrolysis reactions lead to the production of further H^+, $FeOH^{2+}$, $Fe(OH)_2^+$ and $Fe(OH)_3^0$. As expected, the concentration of $FeOH^{2+}$ increases first with increasing pH and then declines as the concentration of $Fe(OH)_2^+$ increases. A similar trend can also be noted for the $Fe(OH)_2^+$ and $Fe(OH)_3^0$ species. Ferric sulphate species dominate at lower pH range while ferric hydroxo species are abundant in the higher pH region.

For the speciation of nickel species (Figure 3.3), it is interesting to note that the dominant nickel species present at low pH is the sulphate complex ($NiSO_4^0$), suggesting the strong complexation ability of sulphate. With increasing pH value, the concentration of free nickel ions (Ni^{2+}) increases significantly. Under the conditions of interest here, other nickel hydroxyl species are negligible.

Figures 3.4 and 3.5 show the calculated concentration distribution of ferric and nickel ions, respectively, as a function of temperature for a solution containing total dissolved Fe^{3+} of 0.015 mol, Ni^{2+} of 0.0025 mol and SO_4^{2-} of 0.05 mol. The predominance of the $FeSO_4^+$ species over the temperature range from 25 to 100 °C is

apparent (Figure 3.4). However, the concentration of the $FeSO_4^+$ species starts to drop with increasing temperature above 70°C, while the concentrations of $FeHSO_4^{2+}$ and $FeOH^{2+}$ increase. For the nickel species (Figure 3.5), in the temperature range studied, the dominant nickel species are $NiSO_4^0$ and Ni^{2+}. The concentrations of other nickel hydroxyl species remain essentially zero.

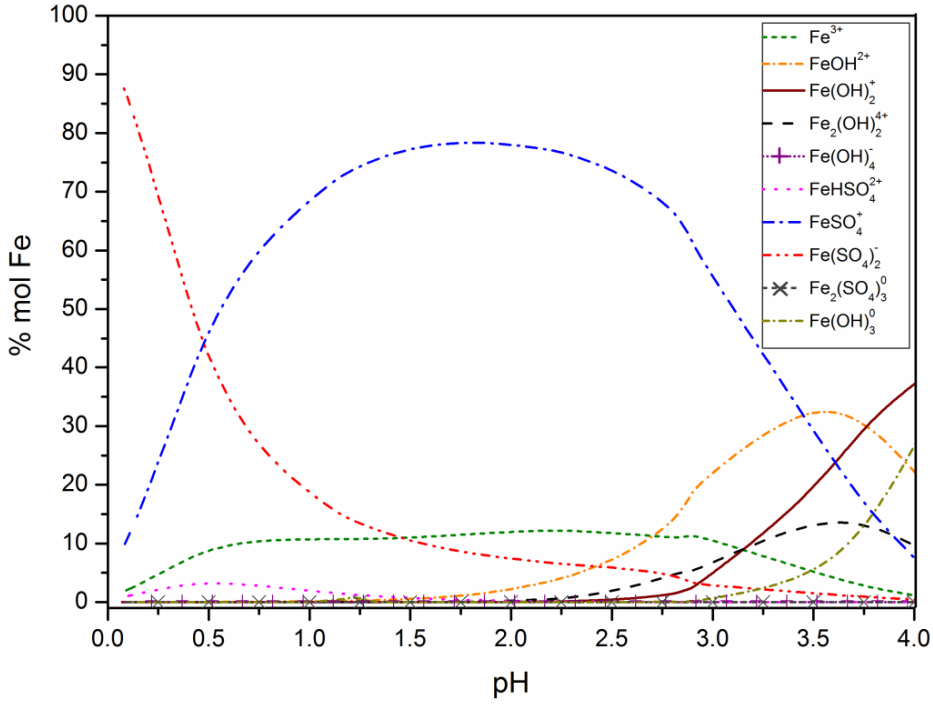

Figure 3.2: Ferric ions speciation diagram at 25 ºC as a function of pH. The simulated solution contains total dissolved Fe^{3+} of 0.015 mol and Ni^{2+} of 0.0025 mol. The pH value is adjusted by varying the total sulphate concentration.

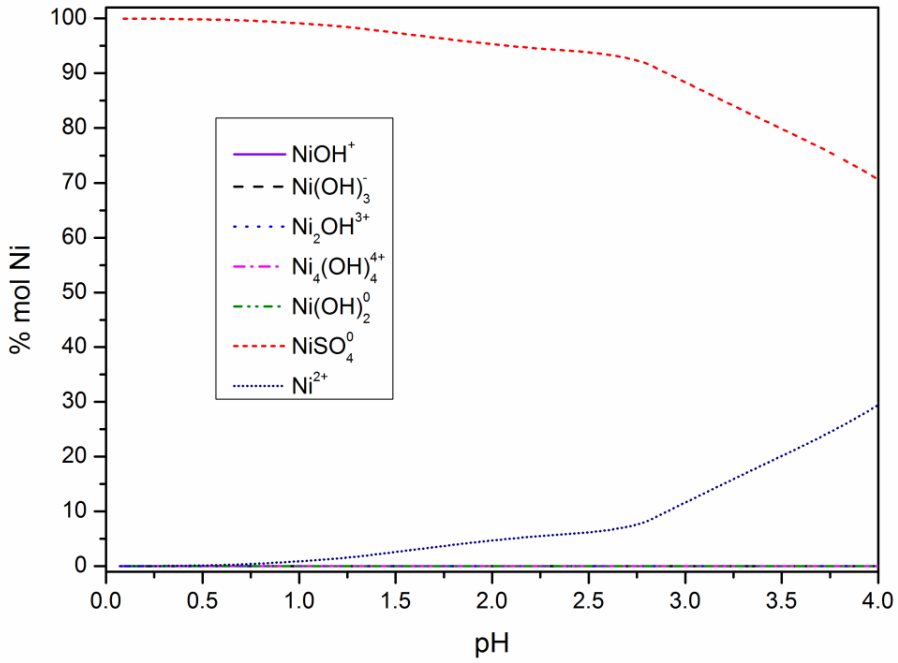

Figure 3.3: Nickel ions speciation diagram at 25 ºC as a function of pH. The simulated solution contains total dissolved Fe^{3+} of 0.015 mol and Ni^{2+} of 0.0025 mol. The pH value is adjusted by varying the total sulphate concentration.

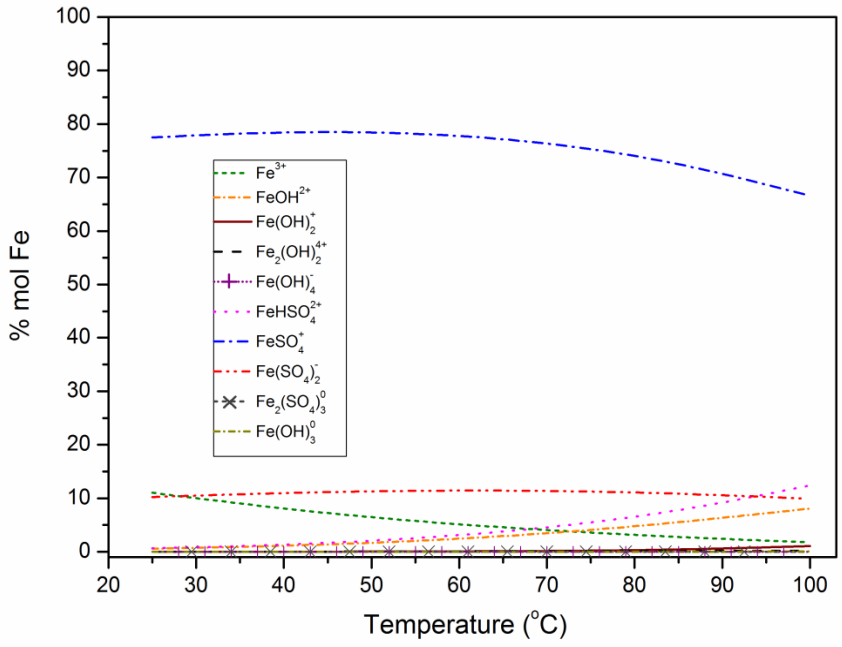

Figure 3.4: Distribution of ferric species as a function of temperature for a solution containing total dissolved Fe^{3+} of 0.015 mol, Ni^{2+} of 0.0025 mol and SO_4^{2-} of 0.05 mol.

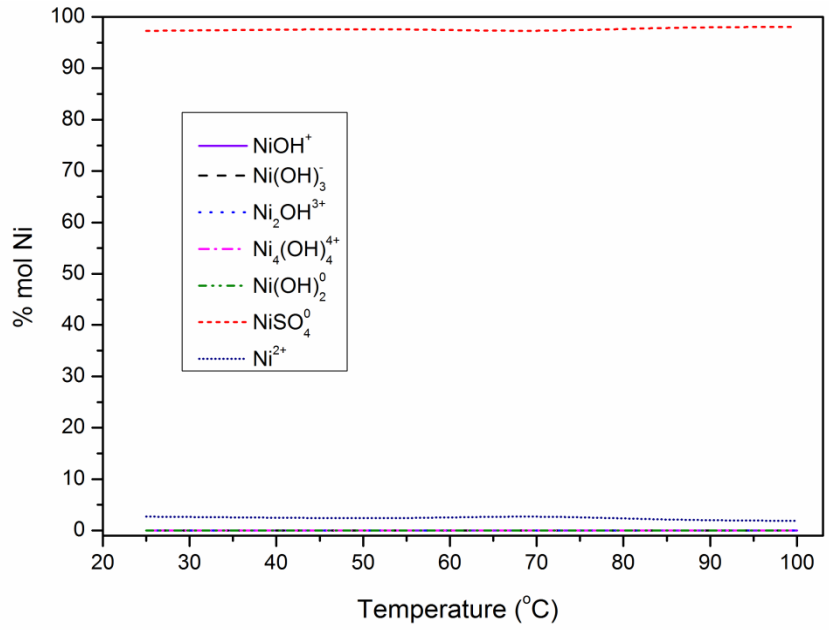

Figure 3.5: Distribution of nickel species as a function of temperature for a solution containing total dissolved Fe^{3+} of 0.015 mol, Ni^{2+} of 0.0025 mol and SO_4^{2-} of 0.05 mol.

One important outcome that supports the validity of this model is that the speciation diagram for ferric ions can indirectly predict the precipitation pathway proceeding through the formation of different iron oxide/hydroxide/oxyhydroxysulphate products. When hydrolysis of ferric ions occurs from a solution in the absence of sulphate, low molecular weight monomer species ($FeOH^{2+}$ and $Fe(OH)_2^{+}$) form first and dominate in the acid pH region at 25 °C (Knight and Sylva, 1974). The monovalent $Fe(OH)_2^{+}$ species favours the formation of goethite, but the divalent $FeOH^{2+}$ which is less favourable for goethite formation dominates when the pH of solution is decreased to less than 4 (Knight and Sylva, 1974; Schwertmann and Murad, 1983). The $FeOH^{2+}$ and $Fe(OH)_2^{+}$ can react to form dimers ($Fe_2(OH)_2^{4+}$). Further polymerization leads to the precipitation of ferrihydrite, or more crystalline iron oxide/hydroxides, such as goethite and hematite (Cornell and Schwertmann, 2003). Ferrihydrite is thermodynamically unstable towards goethite and hematite. It can dissolve to reform soluble ions such as $Fe(OH)_2^{+}$ in acid solution (pH ~4) (Cornell and Schwertmann, 2003). Upon the dissolution of ferrihydrite, hematite is

formed via $FeOH^{2+}$ at pH <4, while the formation of goethite is favoured at pH about 4 where the maximum of $Fe(OH)_2^+$ is achieved (Knight and Sylva, 1974; Schwertmann and Murad, 1983). In the presence of sulphate, the $FeSO_4^+$ is predominant, and the formation of $FeSO_4^+$ strongly suppresses the polymerization of hydroxyl species and the precipitation of goethite (Parida and Das, 1996). Similar conclusions were presented by Matijević *et al*. (1975), Musić *et al*. (1994) and Sapieszko *et al*. (1977). The $Fe_2(OH)_2^{4+}$ species rarely occurs in low concentration in a sulphate solution. Rather, the hydroxo-forms of Fe(III) exist in the form of mixed hydroxyl sulphate complexes $Fe_2(OH)_2(SO_4)_x^{4-2x}$ (Yakovlev *et al*., 1977). The Fe-OH-SO_4 species are not taken into account in the model calculation, as their existences are still uncertain and little published thermodynamic data are available. However, such species are important in sulphate aqueous solution and are reported to be the precursors of the poorly defined oxyhydroxysulfates which have close relationship with schwertmannite (Kiyama and Takada, 1973; Stipp, 1990; Zinck and Dutrizac, 1998).

3.3.3 Predicting solution pH

Using the developed speciation model, it is possible to calculate the activity of the hydrogen ion and hence the pH value of the solution. The result of such a calculation for the solution containing 0.01 mol Fe^{3+}, 0.01 mol Ni^{2+} and 0.025 mol SO_4^{2-} at various temperatures is graphed in Figure 3.6 (solid line). In general, the model predicts that pH of the solution decreases progressively with increasing temperature.

In order to test the model, pH measurements at various temperatures were conducted. In these experiments, a beaker containing a sulphuric solution with nickel and iron of unknown pH value was immersed into a thermostatically controlled oil bath. The pH measurement system consisted of a TPS® AQUA pH meter and a METTLER TOLEDO® pH electrode (InLab® Versatile) which has a working temperature range from 0 to 100 °C. The pH electrode was calibrated before the measurement using pH

4 and 7 buffer solutions. Each measurement at elevated temperature was made after the temperature of the solution was stable for over 10 minutes.

From the comparison of the calculated and the experimental measured pH values, as shown in Figure 3.6, the model values are basically in good agreement with the experimental data. At temperature above 70 °C, it is noticeable that the model predicted pH values are much higher than the experimental measured ones. Such large discrepancies may be due to the formation of solid iron precipitates, and associated generation of acid, at elevated temperature which was not taken into account in the modelling.

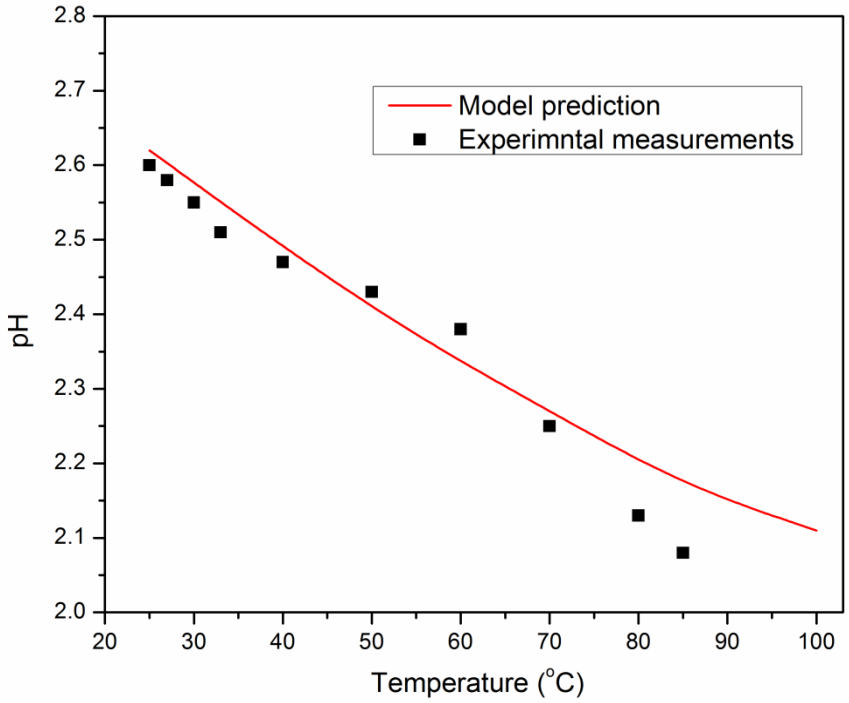

Figure 3.6: Experimental measured and model predicted pH values of solution containing 0.01 mol Fe^{3+}, 0.01 mol Ni^{2+} and 0.025 mol SO_4^{2-} as a function of temperature.

Speciation modelling of aqueous electrolyte solutions, especially the ferric iron aqueous species, has been extensive. However, discrepancies exist between the different speciation diagrams produced. This is mainly attributed to the differences in

the thermodynamic data and modelling methods. Table 3.5 gives a comparison between the calculated data obtained in this study and the values obtained by other researchers. Filippou *et al.* (1995) in this study used a similar thermodynamic database and modelling method to simulate the aqueous electrolyte solution. Hence, excellent agreements exist between the values calculated in the present work and the data previously reported by Filippou *et al.* (1995). Comparison is also made between the data obtained in the present work and the values calculated by the Visual MINTEQ® ver 3.0 computer software package. Visual MINTEQ® is a chemical equilibrium model for the calculation of metal speciation and solubility equilibrium for natural water, which is freely available in the public domain (Gustafsson, 2011). It can be seen from Table 3.8 that good agreement exists for the sulphate only solutions. More significant discrepancies exist when the simulated solution contains ferric iron and/or nickel ions. This may be attributed to the different thermodynamic databases and models used for ion activity correction. In the Visual MINTEQ® software, all the values of equilibrium constants and thermodynamic data are sourced from MINTEQA2 database. The aqueous $FeHSO_4^{2+}$, $Fe_2(SO_4)_3^0$, Ni_2OH^{3+} and $Ni_4(OH)_4^{4+}$ species that are taken into account for the calculation in this study are not included in the MINTEQA2 database. In addition, the default method using in Visual MINTEQ® software for ion activity correction is the Specific Ion Interaction (SIT) model. Within this model, the parameters for cation-cation and anion-anion combinations are neglected. The electrostatic term of the SIT model also gives an inaccurate description of single electrolyte activity (Pivovarov, 2005).

Table 3.8: Comparisons of calculated pH values and ionic strengths to those of other works.

Solution Composition (mol/L)			pH value			Ionic strength (mol/L)		
$[Fe^{3+}]$	$[Ni^{2+}]$	$[SO_4^{2-}]$	(a)	(b)	(c)	(a)	(b)	(c)
0	0	0.01	1.86	1.87	1.87	0.02	0.02	0.02
0	0	0.10	0.99	1.01	1.04	0.16	0.15	0.14
0	0	0.25	0.64	0.66	0.70	0.36	0.33	0.32
0.025	0	0.063	1.54	1.60	1.62	0.10	0.08	0.08
0.01	0.01	0.025	2.62		3.01	0.03		0.05
0	0.02	0.05	1.43		1.56	0.06		0.09
0.10	0	0.15	2.29		2.67	0.22		0.17

Note: (a) this study; (b) Filippou et al. (1995); (c) Computed by Visual MINTEQ ver. 3.0 software program (Gustafsson, 2011).

3.3.4 Saturation index

The stability of a sulphate solution containing 0.015 mol Fe^{3+} and 0.0025 mol Ni^{2+} with respect to goethite, ferrihydrite and schwertmannite is described as a function of saturation index (SI) and pH, as shown in Figure 3.7. Generally, the solubility of goethite, ferrihydrite and schwertmannite decreases substantially with increasing pH values of solution. The saturation index of goethite, ferrihydrite and schwertmannite are all negative at pH values below 2, suggesting the solution is undersaturated with respect to these minerals. Increasing the pH values above 2, the SI is close to the saturation with respect to ferrihydrite but undersaturated with respect to goethite and schwertmannite. Increasing the pH to above 2.25, the solution becomes saturated with respect to goethite, ferrihydrite and schwertmannite. It was interesting to note that the SI of schwertmannite increases steeply with increasing pH. When the pH value is above 2.5, the SI of schwertmannite is much higher compared to those of goethite and ferrihydrite, indicating schwertmannite is expected to be the dominant phase over this pH range.

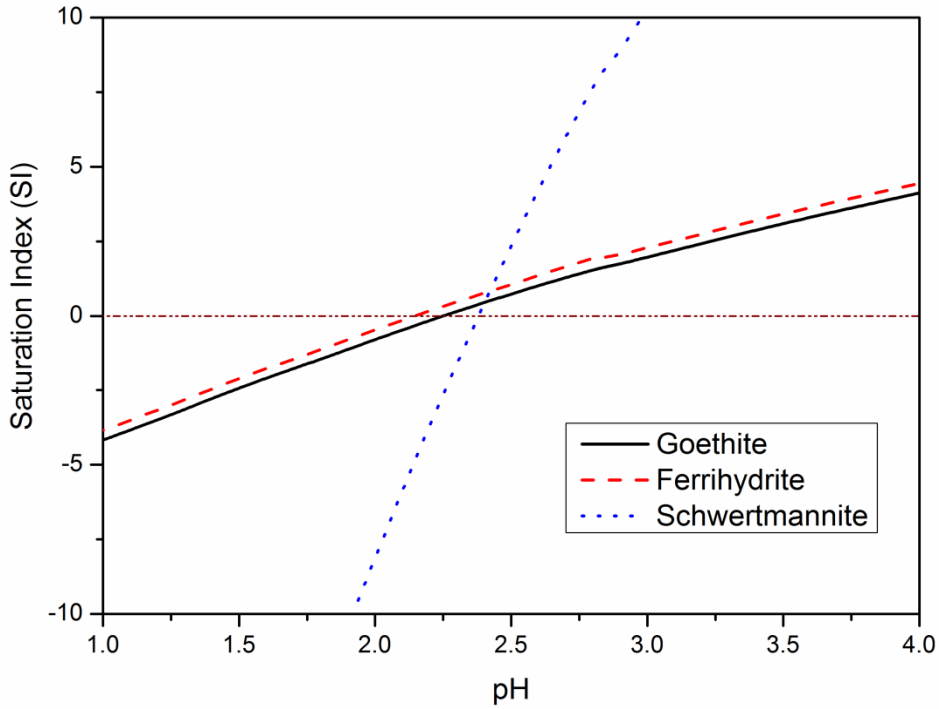

Figure 3.7: Saturation Index (SI) for goethite, ferrihydrite and schwertmannite at 25 ºC, as a function of pH values of solution containing 0.015 mol Fe^{3+} and 0.0025 mol Ni^{2+}.

It is also noteworthy from Figure 3.7 that the changes of SI for goethite and ferrihydrite are very similar in shape, probably due to the similarity in the solubility products ($logK_{so}$=–38.7±0.2 for goethite and $logK_{so}$=–39.02±0.35 for ferrihydrite). In an acidic sulphate aqueous solution, schwertmannite is the dominant phase. Its formation is thermodynamically favoured over ferrihydrite in the pH range between 2 and 8 (Majzlan *et al.*, 2004). However, the calculation of SI is highly dependent on the value of solubility product. Ferrihydrite and schwertmannite are both metastable phases with poorly-ordered structures. The thermodynamics and physicochemical properties of these phases are poorly defined and still under debate. In any event, the present calculations indicate there are specific conditions for the formation of a precipitate such as ferrihydrite, schwertmannite and/or goethite. Further more detailed experimental investigations are, therefore, necessary to investigate the formation mechanisms for these mineral phases.

3.4 CONCLUSION

In this chapter, a speciation model is developed with the effects of ionic strength and temperatures taken into account. The model is able to produce speciation diagrams of all possible species in the Fe(III)–Ni(II)–H_2SO_4–H_2O system, calculate the activity of hydrogen ion and corresponding pH value, and predict the precipitation or dissolution of hydrated iron oxide phases.

In a mixed ferric and nickel sulphate aqueous solution, the predominant ferric and nickel species are $Fe(SO_4)_2^-$ and $FeSO_4^+$ and $NiSO_4^0$ in the highly acidic region (pH<3) at 25°C. At pH above 3, considerable amounts of $FeOH^{2+}$, $Fe(OH)_2^+$, $Fe(OH)_3^0$ and free Ni^{2+} exist. The temperature dependence of the ionic equilibrium can be calculated if the temperature dependence of the equilibrium constant can be obtained. Hence, the accuracy of the developed model highly depends on the accuracy of the equilibrium constants and the extrapolation of these to elevated temperatures. As the temperature increases, the concentration of the $FeSO_4^+$ species decreases while the formation of $FeHSO_4^{2+}$ and $FeOH^{2+}$ become increasing favoured. The changing equilibrium of ferric and nickel species results in changes in the pH value of the system. Increasing temperature results in a decrease in pH value.

Calculation of the saturation index of goethite, ferrihydrite and schwertmannite leads to a better understanding of the formation conditions for goethite, ferrihydrite and schwertmannite. This is achieved by studying the equilibrium relationship between each phases and solution chemistry. The solubility of goethite, ferrihydrite and schwertmannite decreases substantially with increasing pH value of solution. Goethite, ferrihydrite and schwertmannite are all undersaturated below pH 2. With increasing pH, ferric iron tends to precipitate first in the form of ferrihydrite followed by goethite and schwertmannite. A mixture is formed above pH 2.5, of which schwertmannite is predicated to be the dominant phase.

The modelling methodology presented in this chapter can be extended to simulate

other aqueous electrolyte systems. Modelling of aqueous electrolyte solution is extremely useful in developing understanding of solution chemistry and predicting solution properties. The speciation model developed here for the Fe(III)–Ni(II)–H_2SO_4–H_2O system allows prediction of the expected precipitates. This assisted the experimental design for the work presented in subsequent chapters, which aims to provide insight into the mechanisms of the formation for goethite, ferrihydrite and schwertmannite, and the associated nickel losses.

Nomenclature

A= Debye-Hückel constant

Aφ=Debye-Hückel osmotic coefficient parameter

B= Debye-Hückel constant

Cp=heat capacity, $J \cdot mol^{-1} \cdot K^{-1}$

G=Gibbs free energy, $J \cdot mol^{-1}$

H=enthalpy, $J \cdot mol^{-1}$

I_c=ionic strength on molar basis, $mol \cdot L^{-1}$

I_m= ionic strength on molal basis, $mol \cdot kg^{-1}$

K^0=thermodynamic equilibrium constant on molal basis, $mol \cdot kg^{-1}$

K=equilibrium constant on molal basis, $mol \cdot kg^{-1}$

K_{so}=solubility product

K^*_{so}=solubility product described in acidic media

K_w=ionic product of water

M=molecular weight, $g \cdot mol^{-1}$

R=universal gas constant, 8.314 $J \cdot mol^{-1} \cdot K^{-1}$

S=entropy, $J \cdot mol^{-1} \cdot K^{-1}$

T=temperature in Kelvin, K

Y=auxiliary function for the estimation of the Vasil'ev constant b

a=activity

b=Vasil'ev constant

c=molar concentration, $mol \cdot L^{-1}$

f^r= Dickson's auxiliary function

h=hydration number for the hydrogen ion in Das's equation

i=species indicator

m=molal concentration, $mol \cdot kg^{-1}$

p= Dickson's parameter

t=temperature in degree Celsius, °C

z=ionic charge

α_1, α_2=coefficients for the estimation of equilibrium constant of nickel hydroxo species

β^0=thermodynamic equilibrium constant on molar basis, $mol \cdot L^{-1}$

β=equilibrium constant on molar basis, $mol \cdot L^{-1}$

γ=activity coefficient

δ_1, δ_2=coefficients for the estimation of equilibrium constant of neutral nickel sulphate

θ=Helgeson's parameter

ρ=density of solution, $kg \cdot L^{-1}$

Δ=change

CHAPTER 4

THE EFFECT OF IRON PRECIPITATION UPON NICKEL LOSSES FROM SYNTHETIC ATMOSPHERIC NICKEL LATERITE LEACH SOLUTIONS

4.1 INTRODUCTION

Chapter 4 presents an experimental investigation of the effects of iron precipitation on nickel losses from synthetic atmospheric nickel laterite leach solutions. As reviewed in Chapter 2, the loss of nickel is expected to be related to the factors affecting the iron precipitation such as pH, temperature and possibly iron to nickel ratio in the leach liquor. Hence, the purpose of Chapter 4 is to study the effects of various process variables (factors) governing the effect of iron precipitation on nickel losses. This is achieved by using the design of experiment (DOE) and the method of statistical analysis and modelling. The statistically-designed experimental method generally employs a small number of experiments to study the effects of factors and their possible interactions (Chapter 2). These have been successfully applied in many areas of hydrometallurgical processes: see, for example, the study of the V.M. goethite precipitation process (Agatzini-Leonardou and Burkin, 1985), the extraction of nickel and cobalt in heap leach treatment of laterite ores (Agatzini-Leonardou *et al.*, 1997), the recovery of nickel and cobalt by precipitation from neutralised nickel laterite heap leach PLS (Oustadakis *et al.*, 2006), and the effects of agglomeration on iron precipitation (Claassen and Sandenbergh, 2006).

Chapter 4 is separated into three parts. The first describes the preliminary experiments to determine some ‘held constant’ factors that were fixed throughout subsequent statistically-designed experiments. The ‘held constant’ factors include the reaction and ageing times. The effect of these factors and gypsum formation when

using calcium carbonate as the neutralizing agent on the iron removal efficiency and nickel losses were detailed in this part. The second part investigates the effects of five widely used process variables (pH, temperature, the iron to nickel ratio in the initial leach liquor, stirring speed, and the neutralizing agents) on iron removal efficiency and associated nickel losses, using a Fractional Factorial Design (FFD) to screen these variables. The third part employs the Box-Behnken Design (BBD) which is a response surface methodology (RSM) to optimize the significant independent variables determined in the second part.

4.2 EXPERIMENTAL SETUP AND PROCEDURES

Similar to the process described by Roche (2009), a semi-batch precipitation procedure was used in this chapter and the remaining chapters of this thesis, shown in Figure 4.1, which includes a 2 L baffled glass reaction vessel equipped with an overhead agitator. For better mixing, the feed solution and slurry of neutralizing agent were injected directly above a six-bladed titanium Rushton impeller through PTFE tubes. The pH value during reaction was monitored by a METTLER TOLEDO® pH probe (InLab® Versatile) which has a working temperature range from 0 to 100 ºC. A thermostatically controlled oil bath filled with polyethylene glycol was used for temperature control. At the beginning of each experiment, de-ionized water was placed into the reaction vessel to dilute the input streams. A volume of synthetic PLS (500 mL) containing iron and nickel sulphates was pumped into the reaction vessel during a specific period, at a controlled rate ranging from 10 to 20 mL/min to maintain the concentrations of ferric iron between 1.0 and 2.5 g/L (*i.e.* between 0.018 and 0.045 M). The neutralizing agent was simultaneously added at a fixed pumping rate of 5 mL/min, as a suspension in de-ionized water to achieve the target pH value. At the completion of the reaction, the slurry was vacuum filtered through a 0.45 µm Gelman Supor® membrane and the ferric and nickel ion concentrations in the filtrate analysed by ICP-OES. The filter cake was washed three times with large amounts of de-ionized water by repulping the washing water until

nickel was not detected in the third wash water, and then dried overnight at 60 ºC. The chemical composition of the dried solid products was determined by ICP-OES after aqua regia digestion.

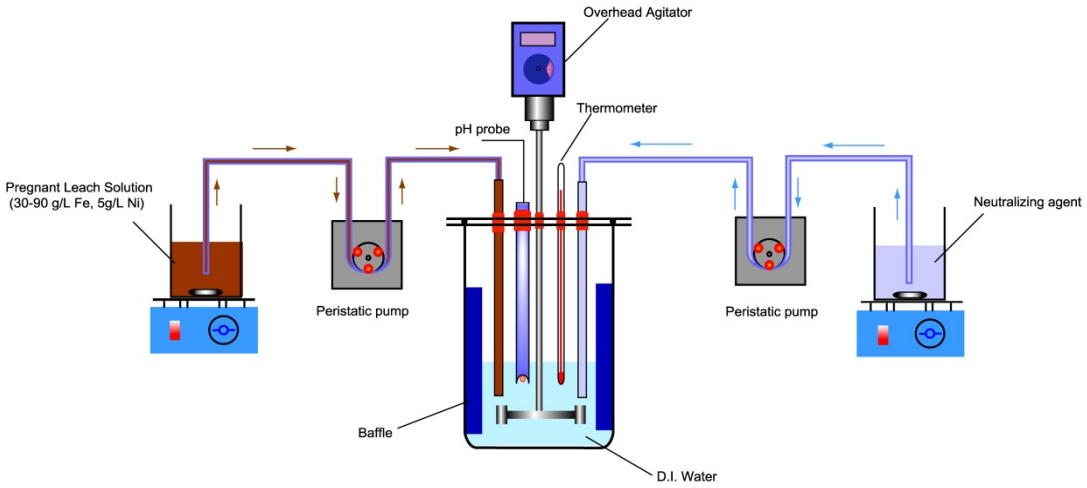

Figure 4.1: Schematic diagram of semi-batch experimental equipment.

All reagents were obtained from various suppliers and used without further purification: $Fe_2(SO_4)_3 \cdot xH_2O$ (Chem Supply, LR) and $NiSO_4 \cdot 6H_2O$ (Ajax Finechem, LR) were used to prepare the PLS. The slurries containing neutralizing agent were prepared by adding MgO (BDH-Limited, AR) or $CaCO_3$ (Chem Supply, AR) powder to de-ionized water.

The two main experimental outcomes or responses investigated in this work were the iron removal efficiency (%) and nickel loss (%). Due to the dilution effects of the semi-batch experimental procedure and large amounts of wash water used, more accurate iron removal efficiency and nickel loss could be determined by analyzing solid residues. These refer to the weight of iron and nickel in the final solid products relative to the initial weight of iron and nickel in the synthetic PLS. Mineralogical investigation was carried out on micronized powder samples by X-Ray Diffraction (XRD) analysis, using a Bruker D8 Advance diffractometer equipped with LynxEye$^{@}$ Super Speed detector. All XRD patterns were collected using a CuKα_1 radiation source operated at 40kV and 40 mA and using a step scan of 0.02º.

4.3 PRELIMINARY EXPERIMENTS

Preliminary experiments were conducted to determine the effects of reaction time, ageing time and gypsum formation on the responses. The 'reaction time' denotes the period for which PLS was pumped, and 'ageing time' refers to the retention time after PLS pumping was completed. In this study, 2.5 and 5 hour reaction times were studied, employing the conditions of experiment FFD-8 (Tables 4.1 and 4.2). To study ageing time, after 2.5 hours reaction, the products were allowed to age for a specific ageing time at the experimental pH, temperature and stirring speed. Gypsum is a common precipitate in the sulphate solution when using $CaCO_3$ as the neutralizing agent. The effect of gypsum formation on the nickel loss was examined in an acid solution of nickel sulphate with no ferric iron present. The nickel concentration was kept at 5 g/L in the preliminary and in subsequent statistically-designed experiments. The acidity was adjusted to a pH of approximately 0.45 using concentrated H_2SO_4, which was the same value of a solution containing 90 g/L iron and 5 g/L nickel. All the experimental procedures were kept the same as those used in the statistically-designed experiments.

4.4 STATISTICAL EXPERIMENTAL DESIGN

4.4.1 Fractional Factorial Design (FFD)

Screening experiments were performed using a one quarter fractional factorial design (FFD) to evaluate the factors that have significant effects on the two responses. The factors investigated were four quantitative factors (pH, temperature, the Fe/Ni ratio in the PLS and stirring speed) and one qualitative factor (neutralizing agent, *i.e.* MgO or $CaCO_3$). All factors were evaluated at two levels: low level (denoted as '–') and high level (denoted as '+'). The factors investigated and their levels are given in Table 4.1, and the experimental design matrix in Table 4.2.

Table 4.1: Factors and selected levels in the 2^{5-2} resolution III fractional factorial design.

Factors	Name	Low level (–)	High level (+)	Unit
A	pH	2	4	pH units
B	Temperature	25	85	°C
C	Neutralizing agents	15 % MgO	25 % $CaCO_3$	w/w
D	Fe/Ni ratio	6	18	-
E	Stirring speed	200	500	rpm

Table 4.2: Design matrix for 5 factors and 8 experiments.

Sample	Run Number	Basic design			Factor generator	
		A	B	C	D=AB	E=AC
FFD-1	1	+	–	+	–	+
FFD-2	2	+	+	–	+	–
FFD-3	3	–	+	+	–	–
FFD-4	4	–	+	–	–	+
FFD-5	5	+	+	+	+	+
FFD-6	6	–	–	–	+	+
FFD-7	7	+	–	–	–	–
FFD-8	8	–	–	+	+	–

The low and high levels of factor A (pH) were set to be 2 and 4, respectively, which is the typical working pH range for an iron oxide/hydroxide precipitation process. For factor B (Temperature), the minimum level of 25°C is not the preferred precipitation temperature currently used in industry due to the possible formation of poorly filterable iron oxides and/or hydroxides, but it has potential application in atmospheric heap leaching. The maximum level, 85°C, is a typical temperature for goethite precipitation (Davey and Scott, 1975). For factor C (Neutralizing agents), the rather high price of magnesia limits its application, whereas the high alkalinity and small volume of final sludge make it an effective neutralizing agent. Conversely, calcium carbonate, the main component of limestone, is a relatively low-cost source

of alkalinity and has a wide application in industry (Hoak and Sindlinger, 1949). For the factor D (Fe/Ni ratio), the nickel concentration was maintained at 5 g/L in all experiments, while the ferric iron concentration was varied from 30 to 90 g/L to achieve the desired Fe/Ni ratios. Such a wide range of concentration roughly approximates those of leach liquors produced by atmospheric sulphuric acid heap, and agitation leaching of nickel laterite ores. The chemical composition of synthetic solutions for each experiment is given in Table 4.3. Stirring speed affects the collision frequency of particles which is closely related to the energy dissipated in a precipitation system (Seyssiecq *et al.*, 1998). Since excessive agitation has a deleterious effect on the settling and filtration rates (Allen *et al.*, 1970), the maximum stirring speed was limited to 500 rpm in this study.

Table 4.3: The initial and final chemical compositions of synthetic solutions.

Sample *	Fe (g/L)		Ni (g/L)	
	Initial	Final	Initial	Final
PT-1	89.12	16.22	4.74	2.18
PT-2	89.12	17.82	4.74	2.21
PT-3	89.12	13.03	4.74	2.13
PT-4	89.12	6.25	4.74	2.10
PT-5	N/A §	N/A	4.91	2.40
PT-6	N/A	N/A	4.91	2.40
PT-7	N/A	N/A	4.91	2.48
PT-8	N/A	N/A	4.91	2.50
FFD-1	27.96	0.006	4.70	2.14
FFD-2	89.12	0.002	4.74	1.16
FFD-3	27.96	0.11	4.70	2.19
FFD-4	27.96	1.17	4.70	2.21
FFD-5	89.12	0.002	4.74	1.22
FFD-6	89.12	27.05	4.74	2.02
FFD-7	27.96	0.003	4.70	1.81
FFD-8	89.12	16.22	4.74	2.18

Table 4.3 continued.

BBD-1	31.38	3.25	5.29	2.55
BBD-2	31.38	0.02	5.29	2.29
BBD-3	31.38	0.07	5.29	2.46
BBD-4	31.38	0.008	5.29	2.32
BBD-5	60.05	15.02	5.09	2.33
BBD-6	60.05	0.68	5.09	2.33
BBD-7	60.05	0.02	5.09	2.11
BBD-8	60.05	0.03	5.09	1.93
BBD-9	60.05	0.01	5.09	2.27
BBD-10	60.05	0.01	5.09	2.25
BBD-11	60.05	0.01	5.09	2.21
BBD-12	90.50	3.14	5.13	2.14
BBD-13	90.50	0.01	5.13	1.53
BBD-14	90.50	0.02	5.13	2.01
BBD-15	90.50	0.01	5.13	2.01

*Note: * PT refers to a preliminary experiment, FFD to a one quarter fractional factorial design experiment and BBD to a Box-Behnken design experiment (see sections 4.5.2 and 4.5.3).* § *N/A =Not Available.*

4.4.2 Box Behnken Design (BBD)

The significant factors determined by FFD and their possible interactions were further studied by using Box-Behnken Design (BBD), which was first developed by Box and Behnken (1960). Details of this modelling approach are included in Appendix B. The three-factor BBD used here is shown in Tables 4.4 and 4.5 with the three levels represented in coded form as –, 0 and +.

Table 4.4: Factors and their levels in BBD.

Factors	Name	Low level (–)	Medium level (0)	High level (+)	Unit
A	pH	2	3	4	pH units
B	Temperature	25	55	85	°C
C	Fe/Ni ratio	6	12	18	-

Table 4.5: Design matrix of BBD for 3 factors and 15 experiments.

Sample	Run Number	Basic design		
		A	B	C
BBD-1	1	–	0	–
BBD-2	2	+	0	–
BBD-3	3	0	–	–
BBD-4	4	0	+	–
BBD-5	5	–	–	0
BBD-6	6	–	+	0
BBD-7	7	+	–	0
BBD-8	8	+	+	0
BBD-9	9	0	0	0
BBD-10	10	0	0	0
BBD-11	11	0	0	0
BBD-12	12	–	0	+
BBD-13	13	+	0	+
BBD-14	14	0	–	+
BBD-15	15	0	+	+

In order to visualize the relationship between response and factors, response surface graphs and corresponding contour plots were constructed in terms of fitted quadratic models. The computer-simulation programming, Design-Expert® Version 8.0.3 (STAT-EASE Inc., Minneapolis, Trial version), was used for regression analysis and graphical construction of the data obtained.

4.5 RESULTS AND DISCUSSION

4.5.1 Preliminary experiments

4.5.1.1 The effect of reaction and ageing time

Normally, iron precipitation reactions can reach equilibrium within several hours at elevated temperature; for example, 1 hour is sufficient for the iron hydrolysis reaction to approach equilibrium at pH 3 and 50°C (Zinck, 1993), and 3 to 3.5 hours for complete precipitation at pH 3 to 3.5 and 85°C in the V.M. and E.Z. goethite processes (Davey and Scott, 1975). However, iron precipitation becomes slower at lower pH values and temperatures, therefore, preliminary experiments were conducted at low pH (2.0) and temperature (25°C) to determine the effect of reaction and ageing time on the degree of iron removal and the amount of nickel loss. These results are given in Table 4.6.

Table 4.6: The effect of reaction and ageing time on iron removal efficiency and nickel loss (pH=2, 25 ºC, neutralizing agent: $CaCO_3$, Fe/Ni=18, stirring speed: 200 rpm).

Sample	Reaction time (h)	Ageing time (h)	Elemental composition in solid product (weight %)			Iron removal efficiency * (%)	Nickel loss to solid * (%)
			Fe	Ni	Ca		
PT-1	2.5	0	16.95	0.0026	15.56	49.89	0.14
PT-2 §	2.5	0	17.26	0.0026	14.90	50.06	0.14
PT-3	5	0	16.99	0.0043	13.46	51.55	0.24
PT-4	2.5	22	17.51	0.0067	15.43	68.99	0.49

*Note: * Weight of nickel and iron in final solid product relative to initial weight of nickel and iron in solution. § Repeat Experiment.*

The first two experimental results shown in Table 4.6 labelled as PT-1 and PT-2, indicated good reproducibility of the experimental method for 2.5 hours reaction time. The effect of reaction time is shown in the experiments labelled PT-1 and PT-3. There is no significant change in overall iron removal when the reaction time increases from 2.5 to 5.0 hours, but a noticeable increase in nickel loss to solid. This result is in good agreement with the work by Davey and Scott (1976) and Köse and Topkaya (2011), in which similar trends were noted for both iron removal and nickel loss. Comparison of PT-2 and PT-4 shows that increasing the ageing time from 0 to 22 hours increases the extent of iron removal significantly but again at the cost of more nickel loss. These results clearly indicate that the reactions conducted at pH=2 and 25°C had not reached equilibrium within the 2.5 hours without any ageing time. However, as the main concern of this chapter was to minimize nickel loss, the subsequent statistically-designed experiments were all conducted with 2.5 hours reaction time and zero ageing time. Hence, the final conditions of precipitation in the experiments are not always equilibrium conditions.

4.5.1.2 The effect of gypsum formation on nickel loss

Gypsum is a common secondary product when using calcium carbonate slurry to neutralize acid sulphate leach solutions. In this section, a series of experiments was conducted to estimate the effect of gypsum formation on the nickel loss, in which an acid nickel-containing solution with no iron present was neutralized with $CaCO_3$ slurry. The results, given in Table 4.7, show no nickel was detected in the final solid products obtained at various pH values and temperatures. The solid product was confirmed to be gypsum by XRD. In addition, the Ca/S ratio of all samples approximated to 1.2 which is close to the ideal value for gypsum. Therefore, the subsequent calculations of nickel loss are based on the assumption that this is only associated with iron-containing precipitates.

Table 4.7: The effect of gypsum formation on nickel loss (neutralizing agent: $CaCO_3$, reaction time 2.5 h, ageing time 0 h, stirring speed: 500 rpm).

Sample	pH	Temp. (°C)	Elemental composition in solid product (weight %)		
			Ni	Ca	S
PT-5	2	25	BDL[§]	21.01	18.85
PT-6	4	25	BDL	21.30	19.02
PT-7	2	85	BDL	21.11	18.74
PT-8	4	85	BDL	21.38	18.80

Note: [§] BDL =Below Detection Limit (0.002 %).

4.5.2 Fractional factorial design (FFD)

A fractional factorial experimental design in one block (2^{5-2}) of resolution III was completed in order to screen the main effects of the five selected factors. The experimental results are given in Table 4.8.

Table 4.8: Elemental analyses obtained for the FFD experiments.

Sample	Elemental composition in solid product (weight %)				Iron removal efficiency (%)	Nickel loss to solid (%)
	Fe	Ni	Ca	Mg		
FFD-1	18.05	0.0483	12.76		89.22	1.42
FFD-2	51.73	0.9096		0.15	96.08	31.79
FFD-3	22.36	0.0079	11.01		87.92	0.19
FFD-4	48.41	0.0079		0.02	84.72	0.08
FFD-5	15.75	0.1660	14.84		96.17	19.17
FFD-6	44.69	0.0079		0.01	29.19	0.10
FFD-7	46.46	0.6263		0.12	95.25	7.64
FFD-8	16.95	0.0026	15.56		49.89	0.14

Fractional factorial design is a saturated design with no degrees of freedom left to

estimate error variance, and consequently conventional ANOVA cannot be used for analysis (Angelopoulos *et al.*, 2009). However, Daniel (1959) presented a method that examines a normal or half probability plot of effect estimates. The assumption is that the system is dominated by some of the main effects and low-order interactions, and that most of the high-order interactions are negligible. The error of these high-order interactions is estimated by combining their mean squares. Thus, the effects that are unimportant are normally distributed with a mean of zero and the variance, σ^2, will tend to fall onto a straight line in this plot, while the statistical significant factors will have non-zero mean values and tend to fall outside the line. The half-normal probability plot is an alternative to the widely used normal probability plot of the factor effects that is easier to interpret particularly when there are only a few tests and effect estimates (Myers and Montgomery, 2002).

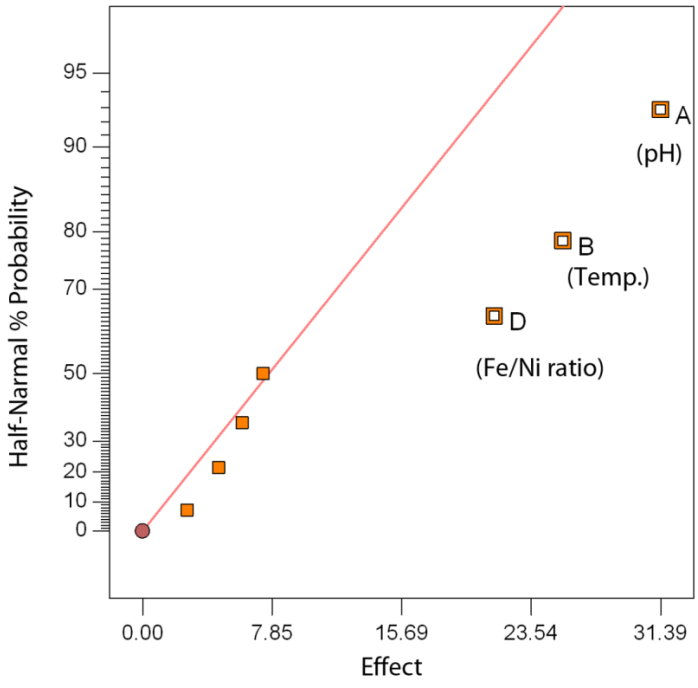

Figure 4.2: Half-normal probability plots for iron removal efficiency (%).

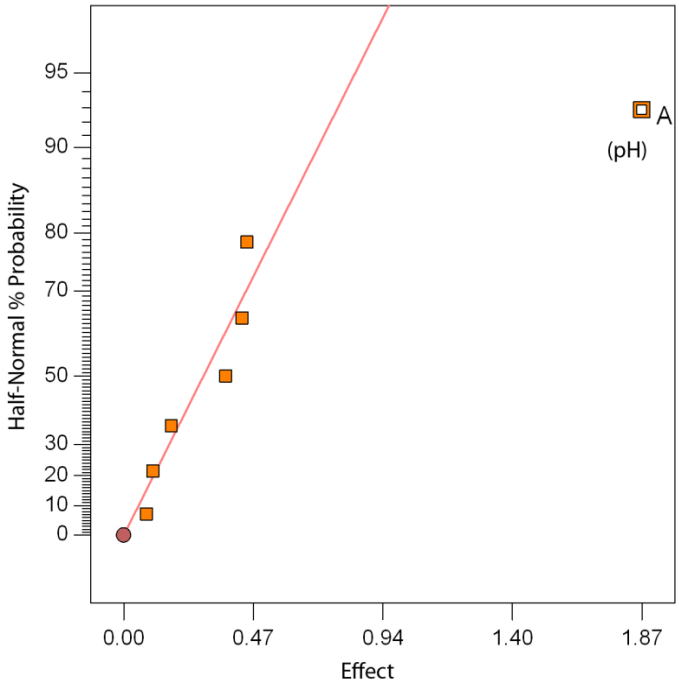

Figure 4.3: Half-normal probability plots of the effects for log (nickel loss (%)).

The factors demonstrating statistically significant effects were estimated by plotting half-normal probability graphs, as shown in Figures 4.2 and 4.3 for iron removal efficiency (%) and log (nickel loss (%)). The nickel loss here is described by a log transformation as the range of response values is large. This data processing technique can be used for stabilizing the variance of the responses. The Box-Cox procedure (Box and Cox, 1964) was used to identify the power transformations for describing data in an appropriate form for statistical analysis. This procedure identifies a transformation from the family of power transformation on y (the responses), in the form of $y' = y^{(\lambda)}$, where λ is the parameter of the transformation to be estimated. For various values of λ, a standard analysis is usually performed on the preferred form as (Box *et al.*, 1978):

$$y^{(\lambda)} = \begin{cases} \dfrac{y^{\lambda-1}}{\lambda \dot{y}^{\lambda-1}} & \lambda \neq 0 \\ \dot{y} \ln y & \lambda = 0 \end{cases} \qquad \text{Eq. 4.1}$$

where $\dot{y}$ is the geometric mean of $y_1, y_2,\ldots,y_n$. The maximum likelihood estimation for λ is the value for which the residual sum of squares, $RSS_{(\lambda)}$, is a minimum. This value of λ can be found by plotting a graph of $RSS_{(\lambda)}$ versus λ and then finding the value of λ that minimizes the $RSS_{(\lambda)}$ from the graph (Myers and Montgomery, 2002).

The graphical representation of $LnRSS_{(\lambda)}$ for various λ is shown in Figure 4.4. The values $LnRSS_{(\lambda)}$ are used here since the range of values for $RSS_{(\lambda)}$ is large. The optimum value of λ is –0.3, which corresponds to the lowest point of the $LnRSS_{(\lambda)}$ curve. Furthermore, the 100(1–α) % confidence interval for λ can be obtained by calculating a critical sum of squares, *SS*, from:

$$SS = SS_{(\lambda)}\left[1+\frac{t^2_{\alpha/2,\nu}}{\nu}\right] \qquad \text{Eq. 4.2}$$

The degree of freedom, *v*, is 6, and α=0.05 for 95% confidence interval in this study. The values of λ_-=–0.62 and λ_+=0.03 for the low and high 95% confidence interval can be obtained from the graph where the line LnRSS parallel to the λ-axis cuts the $LnRSS_{(\lambda)}$ curve. Since the optimum value of λ and zero falls in the 95% confidence interval, the use of a log transformation is adequate for processing the nickel loss (%) data (Figure 4.3).

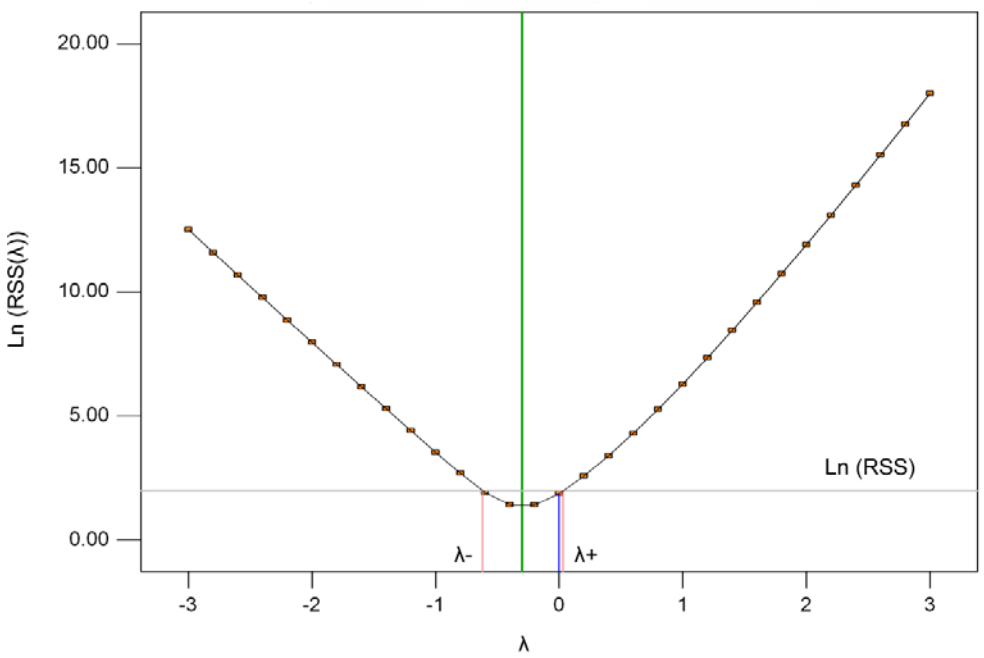

Figure 4.4: The Box-Cox plots used to determine the power transformation applied to the data for nickel loss (%).

Figures 4.2 and 4.3 show the following results: the factors A (pH), B (temperature) and D (Fe/Ni ratio) have large dispersion effects on the iron removal efficiency (%) response, but factor A (pH) is the most important factor within the range of values studied for the log (nickel loss (%)) response. No interaction terms were found to be significant in the half-normal probability plots. This observation is mainly ascribed to the fact that the one-quarter fractional factorial design has the lowest resolution, in which no main effects are confounded with any other main effect, but main effects are confounded with two-factor interactions and some two-factor interactions may be confounded with each other. That is, the effects of A, B and D, as demonstrated in Figure 4.3, are the results of A+BD+CE, B+AD+CDE and D+AB+BCE, respectively. Normally, high order interactions are negligible in a fractional factorial design. Thus the main effects of factors A, B and D are actually confounded with BD+CE, AD, and AB, respectively. Although, the main effects cannot be distinguished from two factor interactions in this analysis, pH, temperature and Fe/Ni ratio lead to variation in the response for iron removal efficiency (%) and only pH appears to determine the quantity of the nickel loss (%). However, taking into

consideration that the pH may be confounded with the interaction of temperature and Fe/Ni ratio, the three factors that had a major contribution to the responses, pH, temperature and Fe/Ni ratio were chosen for a more detailed study through a response surface methodology. The other factors that showed statistical insignificance, *e.g.* neutralizing agents and stirring speed, were fixed in the subsequent optimization experiments. Zinck and Dutrizac (1998) observed that the variation of stirring speed from 200 to 800 rpm had little effect on the amount of iron precipitate or its composition. Therefore, the stirring speed was kept constant: at the higher value of 500 rpm to ensure better mixing. Calcium carbonate was used as the neutralizing agent, mainly because of its wide application in industry and relatively low cost.

4.5.3 Box-Behnken design (BBD)

In order to obtain more meaningful information about nickel losses during the iron precipitation, a Box-Behnken design with fifteen experiments was performed for three factors (pH, Temperature, Fe/Ni ratio) at three levels; with the results given in Table 4.9.

Table 4.9: Elemental analyses obtained for the BBD experiments.

Sample	Elemental composition in solid product (weight %)			Iron removal efficiency (%)	Nickel loss to solid (%)
	Fe	Ni	Ca		
BBD-1	20.45	0.0082	13.06	68.14	0.16
BBD-2	19.80	0.1263	15.75	93.10	3.52
BBD-3	21.39	0.0093	13.19	83.19	0.22
BBD-4	19.92	0.0419	14.74	92.67	1.16
BBD-5	18.68	0.0031	17.38	47.86	0.09
BBD-6	18.04	0.0081	15.40	79.22	0.42
BBD-7	17.91	0.0400	15.52	92.12	2.43
BBD-8	18.52	0.1340	17.46	96.11	8.20
BBD-9	17.44	0.0095	13.06	84.29	0.54
BBD-10	16.94	0.0092	14.94	83.32	0.54
BBD-11	17.46	0.0101	14.15	86.07	0.59
BBD-12	17.60	0.0085	15.45	75.40	0.64
BBD-13	17.38	0.1229	16.20	96.74	12.08
BBD-14	17.66	0.0118	15.28	89.39	1.06
BBD-15	16.77	0.0282	16.54	95.35	2.83

Using these experimental results, and by employing the method of least squares to estimate coefficients of the empirical quadratic models (Appendix Eq. B.1), the iron removal efficiency (%) and log (nickel loss (%)) can be modelled by the following equations:

$$Y_{\text{Iron removal efficiency (\%)}} = -46.36 + 63.83\times \text{pH} + 8.96\times 10^{-1}\times \text{Temperature} - 2.93\times \frac{\text{Fe}}{\text{Ni}}\text{ratio} - 0.23\times \text{pH}\times \text{Temperature} - 6.31\times \text{pH}^2 + 1.39\times 10^{-1}\times \frac{\text{Fe}}{\text{Ni}}\text{ratio}^2$$

Eq. 4.3

$$Y_{\log(\text{nickel loss }(\%))} = -1.07 - 0.54 \times \text{pH} + 1.79 \times 10^{-2} \times \text{Temperature} - 6.78 \times 10^{-2} \times \frac{\text{Fe}}{\text{Ni}}\text{ratio} - 1.05 \times 10^{-3} \times \text{pH} \times \text{Temperature} - 4.19 \times 10^{-4} \times \text{Temperature} \times \frac{\text{Fe}}{\text{Ni}}\text{ratio} + 2.09 \times 10^{-1} \times \text{pH}^2 + 5.7 \times 10^{-3} \times \frac{\text{Fe}}{\text{Ni}}\text{ratio}^2$$

Eq. 4.4

The statistical significance of the above models and their terms were assessed by Fisher's *F*-test, with the analysis of variance (ANOVA) results given in Table 4.10. Normally, a *p*-Value less than 0.05 (95% confidence level) indicates statistical significance. It can be seen from Table 4.10, that both fitted quadratic models contain highly significant terms with very small *p*-Values (<0.0001). It was noted that the interaction of pH and temperature have a significant effect on iron removal efficiency (%) while the interaction of pH and temperature, and temperature and Fe/Ni ratio have a significant effect on Log (nickel loss (%)). The fitted models are adequate as the *p*-Values for "lack of fit" in both models were above 0.05. In addition to the basic analysis of variance, the fit of the quadratic models was evaluated by determining the regression coefficient, R^2. Both iron removal efficiency (%) and log (nickel loss (%)) models demonstrated satisfactory results, with R^2 of 0.9622 for iron removal efficiency and 0.9991 for log (nickel loss (%)).

Table 4.10: ANOVA table for fitted quadratic models.

Source	Iron removal efficiency (%)					Log (nickel loss (%))				
	Sum of Squares	Degrees of Freedom	Mean Square	F Value	p-Value Probability>F	Sum of Squares	Degrees of Freedom	Mean Square	F Value	p-Value Probability>F
Model	2261.28	6	376.88	33.92	<0.0001	5.16	7	0.74	1105.75	<0.0001
A-pH	1443.43	1	1443.43	129.93	<0.0001	3.54	1	3.54	5310.81	<0.0001
B-Temp.	322.44	1	322.44	29.02	0.0007	0.68	1	0.68	1027.39	<0.0001
C-Fe/Ni ratio	48.95	1	48.95	4.41	0.069	0.61	1	0.61	914.18	<0.0001
AB	187.27	1	187.27	16.86	0.0034	3.965×10^{-3}	1	3.965×10^{-3}	5.95	0.0448
BC						0.023	1	0.023	34.08	0.0006
A^2	143.83	1	147.83	13.31	0.0065	0.16	1	0.16	245.2	<0.0001
C^2	93.26	1	93.26	8.39	0.02	0.16	1	0.16	234.6	<0.0001
Residual	88.88	8	11.11			4.667×10^{-3}	7	6.666×10^{-4}		
Lack of Fit	85.01	6	14.17	7.32	0.125	3.652×10^{-3}	5	7.304×10^{-4}	1.44	0.4581
Pure Error	3.87	2	1.93			1.014×10^{-3}	2	5.072×10^{-4}		
Corrected Total	2350.16	14				5.16	14			

The model results can be plotted as 3D response surface graphs and 2D contour plots (Figures 4.5 to 4.7). All the response surface graphs display saddle points, *i.e.* neither maximum nor minimum values, for iron removal efficiency (%) and nickel loss (%) could be achieved within the factor ranges used. According to Figure 4.5, there are a wide range of experimental conditions for which most of the iron can be removed, for example, more than 80% of iron was removed from solution above pH 3, even at 25 ºC, and nearly complete iron removal was achieved at a pH value of around 4. At pH of 2, however, the iron removal efficiency (%) was reduced to about 50% when the temperature was 25 ºC. In addition, it appears to be difficult to distinguish the individual effect of Fe/Ni ratio on the iron removal efficiency (%), probably due to the confounding of the individual Fe/Ni ratios with the factors pH and temperature.

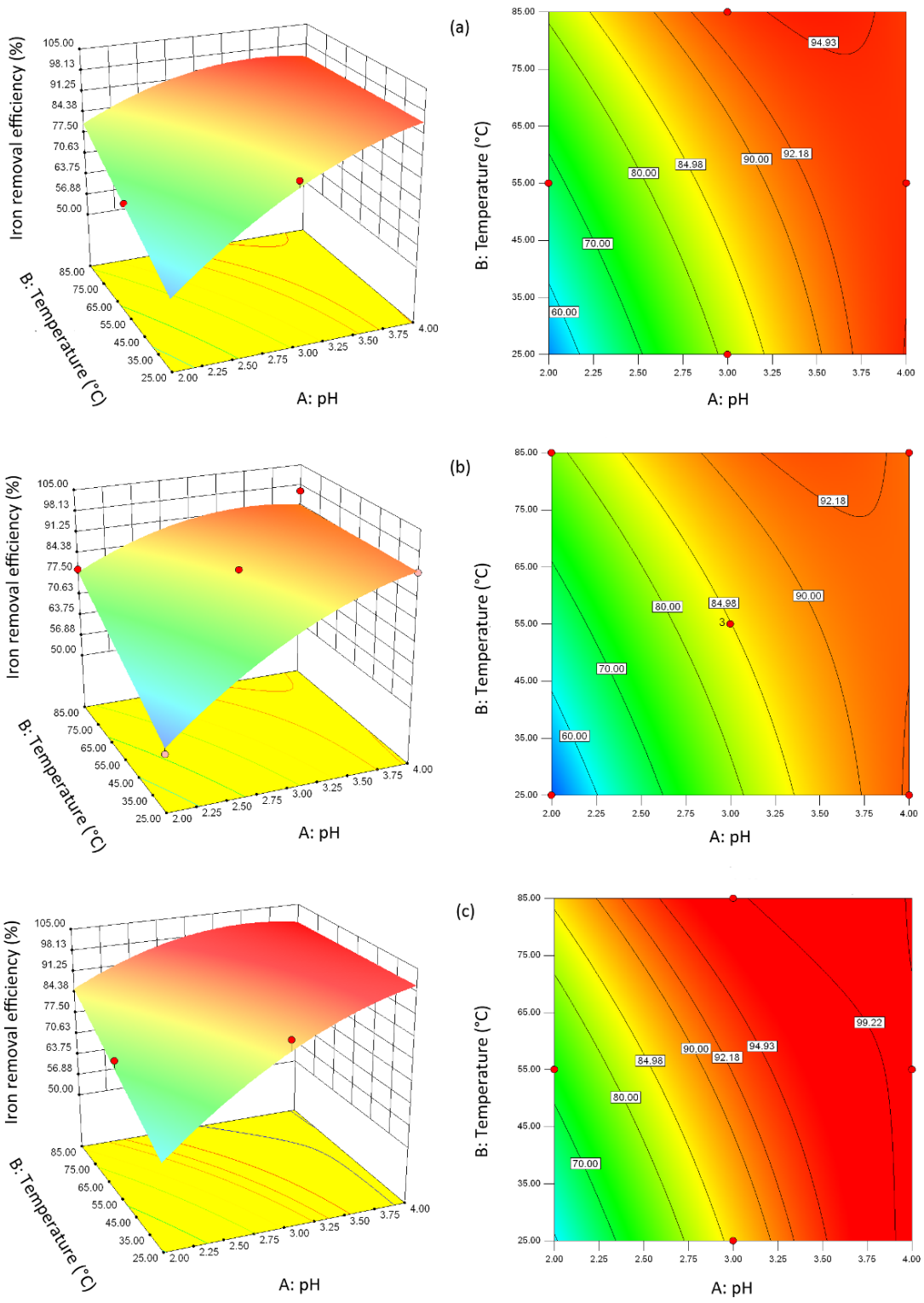

Figure 4.5: Response surface graphs (left) and corresponding contour plots (right) showing the effects of interaction of pH and Temperature on iron removal efficiency (%) ((a) Fe/Ni=6; (b) Fe/Ni=12; (c) Fe/Ni=18).

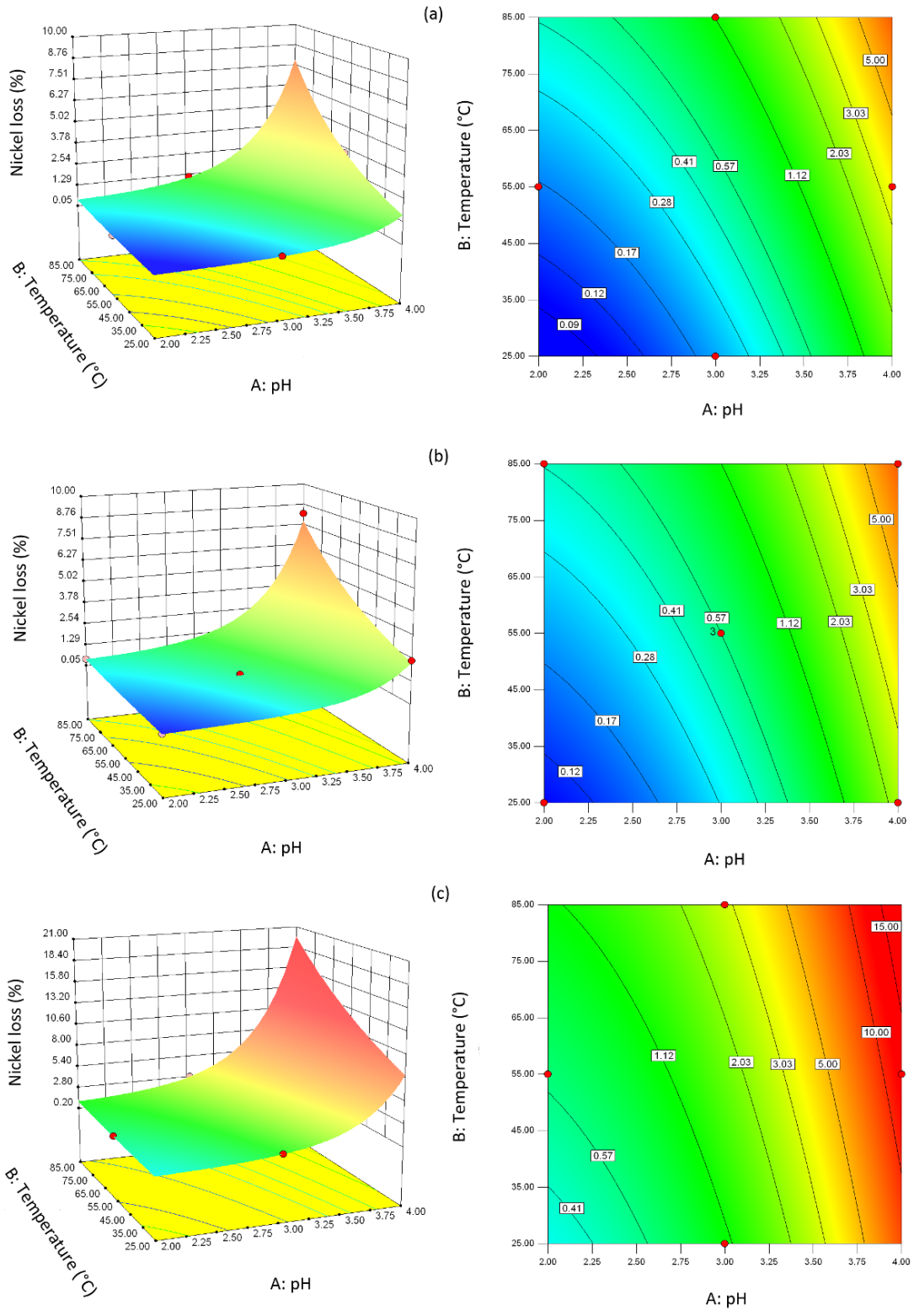

Figure 4.6: Response surface graphs (left) and corresponding contour plots (right) showing the effects of interaction of pH and Temperature on nickel loss (%) ((a) Fe/Ni=6; (b) Fe/Ni=12; (c) Fe/Ni=18).

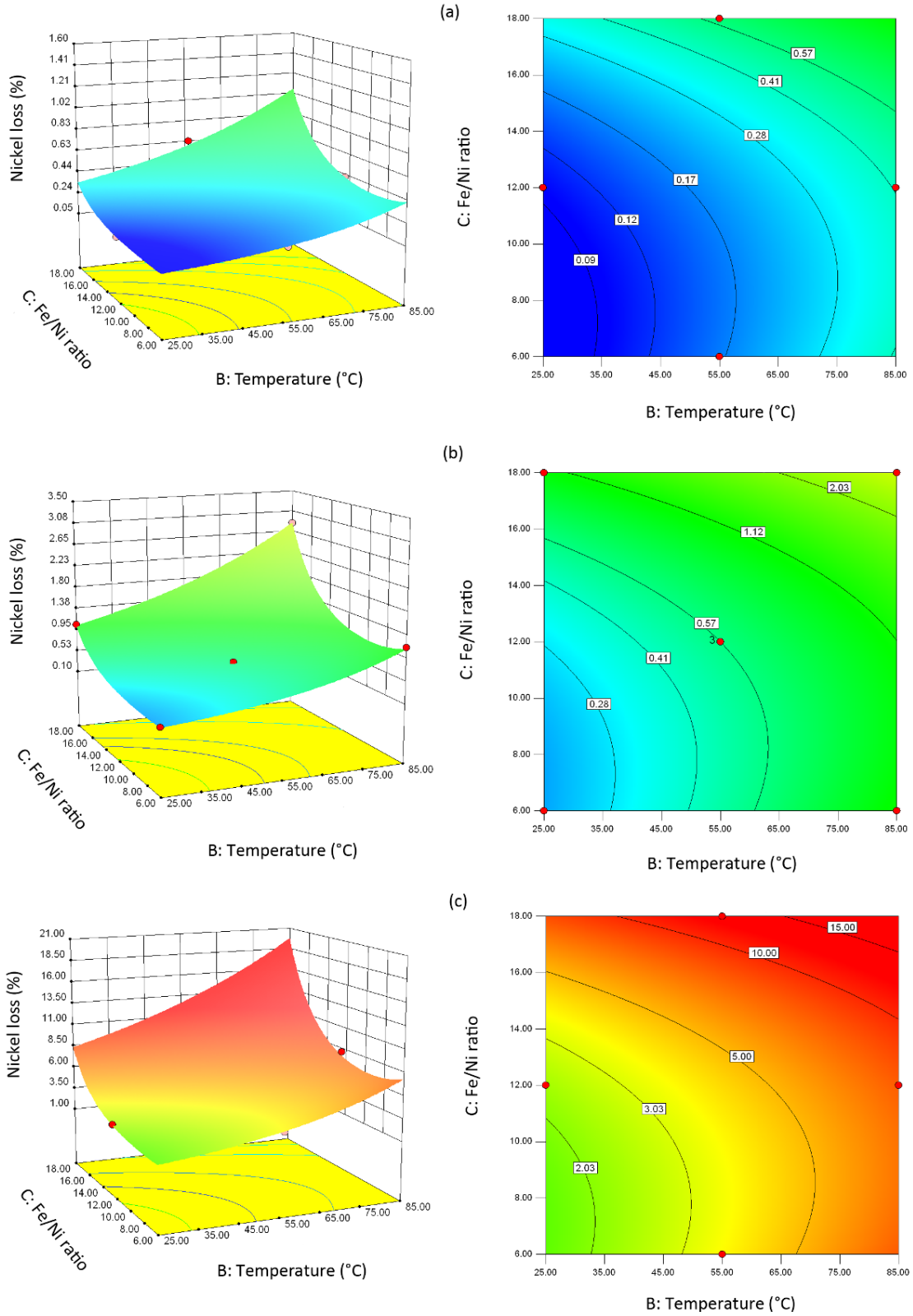

Figure 4.7: Response surface graphs (left) and corresponding contour plots (right) showing the effects of interaction of Temperature and Fe/Ni ratio on nickel loss (%) ((a) pH=2; (b) pH=3; (c) pH=4).

Nickel loss (%) can be minimized to less than 1% by adjusting the pH to 2 (Figures 4.5 and 4.7). At this pH value, however, increasing the temperature from 25 to 85 ºC resulted in greater nickel loss, for example, from 0.42 to 1.06% for a Fe/Ni ratio of 18. Similar behaviour was also noted by Davey and Scott (1975), who investigated the effect of temperature on the loss of zinc in the E.Z. process, and concluded that increasing temperature resulted in an increase in the divalent ions incorporated into the iron-containing precipitate. A higher Fe/Ni ratio was found to lead to greater nickel loss in this study (Figure 4.7). These results are in good agreement with the observations in a recent study on V.M. goethite precipitation in synthetic leach liquor simulating the PLS produced by atmospheric leaching of laterite ores (Chang *et al.*, 2010), in which a higher initial Fe/Ni ratio in synthetic solutions resulted in more nickel loss to the residue within the pH range of 2.5 to 3.0.

4.5.4 Process optimization and model prediction

The models developed by the response surface methodology allow iron removal efficiency (%) and nickel loss (%) to be optimized independently. Figures 4.5 and 4.6 respectively show that iron removal is optimized by increased pH and temperature and nickel loss is reduced by decreased pH and temperature, hence one response may need to be optimized at the expense of the other. If the target value is set at 95% for iron removal efficiency (%) and 1.5% for nickel loss (%), the optimized factors and model predicted values are highly dependent on the priority of the target. Table 4.11 shows that if the goal of 95% iron removal efficiency is given priority it can only be achieved with greater than 1.5% nickel loss, whereas if the goal of 1.5% nickel loss is given priority it can only be achieved with less than 95% iron removal efficiency. The models suggest that a “high temperature-low pH, and low temperature-high pH” multi-step neutralizing strategy is likely to be required. This approach is the same as that adopted by Roche (2009).

Target Value			Optimized factors			Model Predicted Value	
Iron Removal Efficiency (%)	Importance	Nickel Loss (%)	Importance	pH	Temperature (°C)	Fe/Ni ratio	Iron Removal Efficiency (%)	Nickel Loss (%)
95	+++++	1.5	+	3.99	25	6	95	1.64
95	+	1.5	+++++	3.19	85	6	94.77	1.5

4.5.5 XRD analysis of the precipitates

The iron precipitation process used in this work is similar to the semi-batch precipitation method reported by Roche (2009), which in turn is a modified E.Z. goethite process. The E.Z goethite process was named by Allen *et al*. (1970) because of the resemblance of the precipitates to goethite, however Gordon and Pickering (1975) noted that the residues appeared not be the pure goethite. The extensive experiments by Davey and Scott (1975) showed that the so-called goethite precipitates may consist of goethite (α-FeOOH), akaganéite (β-FeOOH), lepidocrocite (γ-FeOOH), hematite (α-Fe_2O_3), maghemite (γ-Fe_2O_3) as well as poorly crystalline phases. Dutrizac (1987) found that the final precipitates contained some poorly defined basic iron sulphates rather than conventional goethite precipitates which were later identified as ferrihydrite and/or schwertmannite (Claassen *et al*., 2002; Loan *et al*., 2002).

Figure 4.8 shows the XRD patterns of several precipitation products obtained under various experimental conditions. Additional washing was performed to remove gypsum from these samples before XRD analysis. It was noted that the mineralogy of these precipitates is dominated by poorly structural-ordered schwertmannite and/or ferrihydrite. No obvious presence of goethite was detected by XRD. In the presence of sulphate, the formation of schwertmannite is considered to be thermodynamically favoured over ferrihydrite in the pH range between 2 and 8 (Majzlan *et al*., 2004).

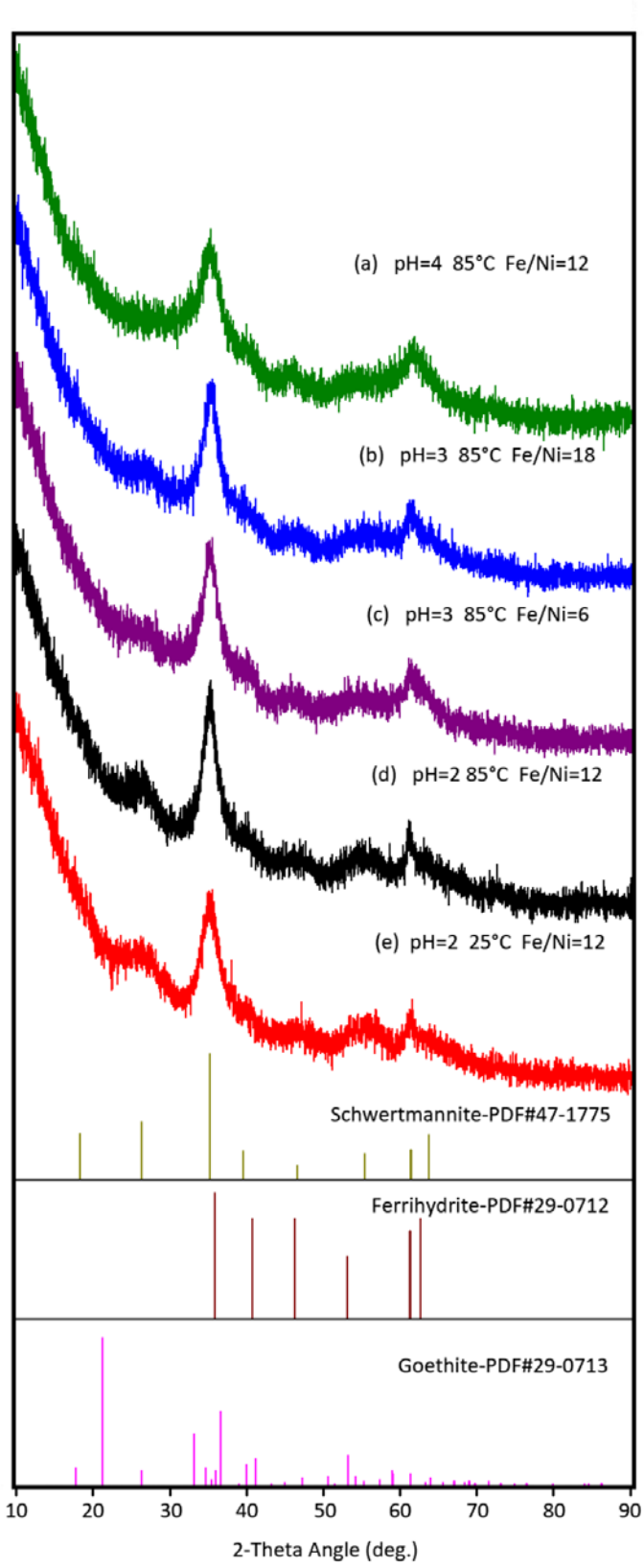

Figure 4.8: X-ray diffraction patterns of the final precipitates obtained from various experimental conditions. The stick representations are those of the standard patterns.

The identification of ferrihydrite and schwertmannite is complicated as these occur in small particles close to or below 10 nm in size (Murad and Rojík, 2003). The disordered nature of ferrihydrite results in small diffracting domains that are hard to detecte by conventional X-Ray Diffraction (XRD) (Jambor and Dutrizac, 1998). Claassen (2006) proposed that schwertmannite is nothing more than ferrihydrite with high sulphate values. In fact, schwertmannite is distinguished from ferrihydrite by a tunnel structure similar to that of akaganéite, which is formed in the chloride system (Cornell and Schwertmann, 2003). Ferrihydrite and schwertmannite are thermodynamically unstable, and proposed to be the growth precursors of more crystalline iron oxides, such as goethite and hematite (Bigham *et al*., 1996; Pollard *et al*., 1992). Increasing temperature favours the transformation towards more stable goethite and/or hematite (Jolivet *et al*., 2004; Schwertmann *et al*., 1999). The presence of goethite is not clearly identified from the XRD analysis in the present study (Figure 4.8), possibly because the transformation of the ferrihydrite to goethite is inhibited by the presence of divalent Ni ions (Cornell *et al*., 1992), or that the main XRD peaks of goethite are overlapped by the presence of large amounts of poorly crystalline ferrihydrite and schwertmannite. However, it is well known that schwertmannite and ferrihydrite can be dissolved more easily than goethite by acidic ammonium oxalate at pH 3 and 25 ºC in the absence of light (Bigham *et al*., 1996). Therefore, the presence of goethite could be confirmed after selectively removing these poorly crystalline phases. More detailed characterization of the iron precipitates can potentially help to understand the nickel loss mechanisms. This is pursued in Chapter 7.

4.6 CONCULSION

In this Chapter, statistically-designed experiments combined with response surface methodology were successfully employed for modelling the nickel loss associated with iron precipitation from synthetic nickel laterite AL liquors containing just nickel and iron. The following conclusions can be drawn:

1) The two-level fraction factorial design is an effective tool to identify which factors will have significant impacts on the desired responses. Four quantitative factors (pH, temperature, the initial Fe/Ni ratio and stirring speed) and one qualitative factor (neutralizing agents) were considered in this stage. It was found that the neutralizing agent and stirring speed had little effect on iron removal efficiency (%) and log (nickel loss (%)).

2) Emphasis was placed on the investigation of the effects of important factors and how these factors interact with each other. Three factors, pH, temperature and Fe/Ni ratio were further studied by a three-level Box-Behnken design. Employing response surface methodology, the data obtained from the Box-Behnken design was used to develop mathematic models for both iron removal efficiency (%) and log (nickel loss (%)). Satisfactory precision was obtained, as well as good accuracy.

3) Graphical response surface and contour plots were constructed to demonstrate the links between responses and the interaction of factors. It should be noted that such models only work satisfactorily within the ranges of factor values studied but must be used with caution for conditions outside these ranges.

4) The data suggest that a “high temperature-low pH, and low temperature-high pH” multi-step neutralizing strategy is best suited to the removal of iron from the solutions examined in this chapter. It becomes clear shortly that the effects of other trivalent metals such as aluminium and chromium on nickel loss need to be studied in further detail, which is considered in Chapter 5.

5) The precipitates obtained in this chapter were mainly composed of ferrihydrite and schwertmannite rather than pure goethite. The formation/presence of goethite needs to be confirmed by further studies. Chapter 7 provides insight into this issue.

CHAPTER 5

IRON, ALUMINIUM AND CHROMIUM CO-REMOVAL FROM SYNTHETIC AND REAL ATMOSPHERIC NICKEL LATERITE LEACH SOLUTIONS

5.1 INTRODUCTION

As outlined in Chapter 1, the pregnant leach solution produced from atmospheric acid leaching of nickel laterite ores often contains significant amounts of impurities, of which ferric iron is the most abundant. The other main soluble trivalent ions include aluminium and chromium. The effect of iron precipitation on nickel losses has been discussed in Chapter 4. Chapter 5 presents a further experimental study on the iron, aluminium and chromium co-removal by precipitation from both synthetic and real atmospheric nickel laterite leach solutions.

Iron, aluminium and chromium are often removed by chemical precipitation before the recovery of nickel (and cobalt). The pH value is the main variable that governs the impurity rejection efficiency, as is detailed for the case of iron precipitation in Chapter 4. An example of a titration curve of typical Acid Mine Drainage (AMD) containing Fe^{3+} and Al^{3+} ions is given in Figure 5.1. The titration curve shows two steep inflection points at pH values about 3.0 and 4.5. This suggests a considerable acidity released due to the hydrolysis of Fe^{3+} and Al^{3+} ions. Their respective following plateaus at pH values above 3.0 and 4.5 correspond to the total hydrolysis and precipitation of iron and aluminium. The gentle slope in the pH range from 5 to 9 suggests the progressive hydrolysis of other metallic cations.

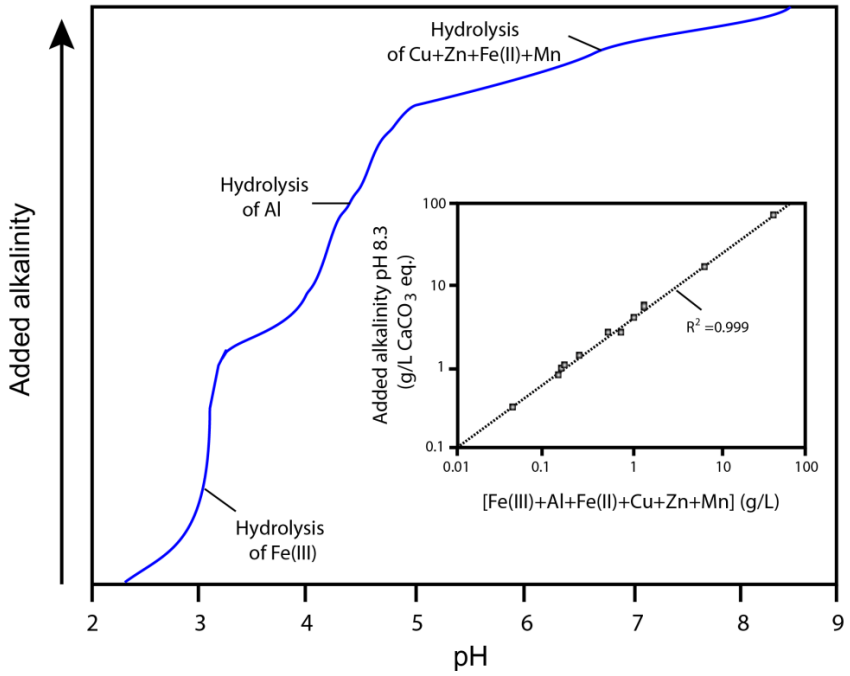

Figure 5.1: Typical titration curve of an acidic mine water. The inset shows the correction between the acidity released during titration of water from an acidic mine pit lake to a target pH value of 8.3 and respective concentrations of major cations (Fe(III)+Al+Fe(II)+Cu+Zn+Mn) (After España (2007)).

Figure 5.2 gives another example showing the precipitation of heavy metals with the progressive neutralization of the solution. The precipitation curves clearly show the order of heavy metal hydroxide precipitation as a function of pH. Figures 5.1 and 5.2 indicate that ferric iron precipitation occurs at a lower pH range, than aluminium and chromium. Hence, in order to achieve maximum removal of aluminium and chromium, higher pH values for precipitation are often used. The study by Agatzini-Leonardou *et al.* (2009) on the separation and recovery of nickel from heap leach liquor of nickeliferrous laterite ore has shown that more than 92% of the iron in solution can be easily removed by raising the pH value of the solution to around 2.8 at 95 ºC, whereas the removals of aluminium and chromium under the same conditions are lower, reported as 73% and 76%, respectively. Increasing pH to 4.0, 98.7% iron, 97.7% aluminium and 95.8% chromium can be removed. In the work of

Agatzini-Leonardou *et al*. (2009), similar to the experiments reported in Chapter 4, a conventional single-stage precipitation procedure was used. However, a multi-stage precipitation process for impurity removal has gained more attention in industrial operations to obtain better impurity removal efficiency, easier handing of waste products, and to minimise losses of valuable metals.

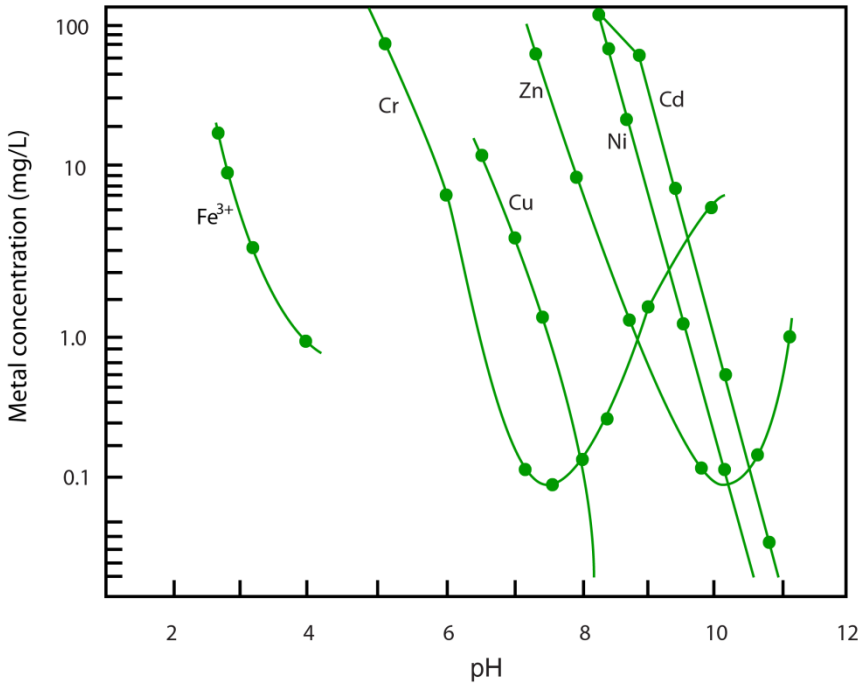

Figure 5.2: Precipitation of heavy metals as hydroxides (After Zinck (1993)).

Boliden Mineral AB (Bolin and Sundkvist, 2008; Sundkvist, 2002) patented a two-stage precipitation process to separate iron and arsenic efficiently from acidic leach solution, which produces a very clean iron-arsenic precipitate with minimum co-precipitation of base metals. The pH of the acid leach solution is raised and controlled in the range of 2.2 to 2.8 at 35 ºC to remove above 90% ferric iron in the first stage. The resulting slurry is discharged into a thickener. The overflow from the thickener is then diverted to the second stage precipitation, where pH is increased to a value in the range of 3.0 to 4.5 and air is injected simultaneously to remove ferrous iron as well. Above 99% zinc and copper recoveries to solution are reported by using this two-stage precipitation process to deal with acidic leach liquors.

The study on iron, aluminium and chromium removal from laterite heap leach solutions by Guise and Castro (1996) showed that 41.3% iron, 21.8% aluminium and 29.5% chromium were rejected at pH 1.8 and 90 ºC by the addition of 50 g/L MgO slurry in the first stage of the precipitation process. In the second stage of the precipitation process operated at pH 2.5 and 90 ºC, 99.9% iron, 53% aluminium and 93.9% chromium of that remaining after the first stage were removed, but at a cost of 26.5% nickel and 37.1% cobalt losses to the solids. Köse and Topkaya (2011) recently studied the Mixed Hydroxide Precipitation (MHP) process to remove impurities from the leach liquors of nontronite type lateritic ores, and showed that the concentrations of Fe^{3+}, Al^{3+} and Cr^{3+} decreased from 38600, 3950, and 1060 ppm respectively to 290, 1260 and 202 ppm by a first removal stage conducted at pH 2.5 and 90 ºC, and these values further dropped to 1.38, 3.6 and 0.77 ppm by a second removal stage conducted at pH 4.25 and 70 ºC. However, nickel loss at the second removal stage was still substantial at 17.2 %.

Unfortunately, the levels of nickel losses to the solids are very high in the impurity-removal processes of Guise and Castro (1996) and Köse and Topkaya (2011). Therefore, a more detailed study on the precipitation process for impurity removal is required to achieve acceptable low levels of nickel loss, which is the aim of this chapter. The aims of Chapter 5 are to study the effects of iron, aluminium and chromium co-elimination upon nickel losses, develop a multi-stage precipitation process to remove impurities efficiently without causing significant losses of nickel, and produce precipitation sludge with satisfactory physical properties such as fast settling rate. In order to achieve these goals, both single- and multi-stage precipitation experiments were carried out with synthetic leach solution and real leach liquor obtained by column leaching of low-grade Western Australia nickel laterite ores with sulphuric acid at ambient temperature. The precipitation experiments for the synthetic leach solution are conducted using a solution containing various combinations of metal ions: Fe(III)+Ni(II), Fe(III)+Ni(II)+Al(III), Fe(III)+Ni(II)+Cr(III) and Fe(III)+Ni(II)+Al(III)+Cr(III).

5.2 EXPERIMENTAL

5.2.1 Single-stage precipitation

All the single-stage precipitation experiments were conducted using a semi-batch reaction vessel. The experimental set-up and procedure has been detailed in Chapter 4. For each experiment, a volume of 500 mL of synthetic leach solutions containing 30 g/L Fe^{3+} [as $Fe_2(SO_4)_3 \cdot xH_2O$], 0 to 5 g/L Ni^{2+} [as $NiSO_4 \cdot 6H_2O$], 0 to 6.5 g/L Al^{3+} [as $Al_2(SO_4)_3 \cdot 18H_2O$], and 0 to 2 g/L Cr^{3+} [as $Cr_2(SO_4)_3 \cdot xH_2O$] was pumped into a baffled reaction vessel containing a pre-determined amount of de-ionized water over a period of 2.5 hours. A $CaCO_3$ (25% w/w) suspension in de-ionized water was simultaneously pumped into the reaction vessel to achieve the target pH values. The temperature was controlled using an oil bath and the precipitation reactions conducted at 25, 55 or 85 ºC. At the completion of the reaction, the resulting slurry was vacuum filtered through a 0.45 µm Gelman Supor® membrane. The metal concentrations in the filtrate were analysed by ICP-OES, the filter cake was carefully washed with large amounts of de-ionized water, and then dried overnight at 60 ºC. The chemical composition of the dried solid products was determined by ICP-OES after aqua regia digestion.

5.2.2 Multi-stage precipitation

Multi-stage precipitation experiments with a combination of pH and temperature control were conducted using both synthetic and real leach solutions. The multi-stage precipitation experiments consisted of two consecutive precipitation processes. Similar to the single-stage precipitation described in section 5.2.1, the first stage precipitation process involved pumping 500 mL of leach solution into a reaction vessel within 2.5 hours. A $CaCO_3$ (25% w/w) suspension in de-ionized water was pumped simultaneously to control pH value. Temperature was controlled by an oil bath. Instead of stopping the reaction after 2.5 hours, a second stage of precipitation was conducted by ageing the resultant slurry for one hour. After leach solution

pumping was completed, the pH was adjusted to the desired value by pumping $CaCO_3$ (25% w/w) suspension in de-ionized water or adding concentrated H_2SO_4, and the temperature was increased as required by heating. Once the new equilibrium pH and/or temperature were reached, the reaction was maintained for 1 hour. It should be noted that the second stage is described as a precipitation process, however, depending on the final pH and temperature compared to the first stage, it may involve a combination of precipitation and/or dissolution of existing precipitate.

5.2.3 Flocculant preparation and settling rate test

Two commercial polyacrylamide polymers were used as flocculants to improve the settling rate of sludge produced from the precipitation: a non-ionic polymer, FA 920 VHM, and a cationic polymer, FO 4190 VHM. Both flocculants are supplied by SNF FLOERGER®, France.

Flocculant was prepared by the method used by Loan (2004). The flocculant stock solution was prepared 1 day before use. Flocculant powder, 0.25 g, was placed in a clean 100 mL plastic bottle and 2 mL of methylated spirits added. After adding 98 mL of de-ionized water, the bottle was stoppered by a lid and shaken vigorously for 30 seconds. The bottle was then agitated on a roller for 1 hour. Before use, the flocculant stock solution was diluted by a factor of 10 to give a fresh flocculant solution with concentration of 0.025%.

The settling rate test was conducted in a 250 mL measuring cylinder at room temperature. After transferring 250 mL of sludge from the reaction vessel to the measuring cylinder, a specific dosage of fresh flocculant was added. The measuring cylinder was inverted 10 times to ensure thorough mixing. Once the cylinder was set upright, the settling rate was determined as a function of time from the height of the solid-liquid interface (mud-line). The drop in the mud-line was plotted as a function of time and the slope of the linear portion of the plot used to define the initial settling rate.

5.3 RESULTS AND DISCUSSION

5.3.1 Single-stage precipitation experiments

Single-stage experiments were conducted with the aim of estimating the effects of the co-precipitation of trivalent iron, aluminium and chromium ions on nickel losses. Table 5.1 gives the initial and final chemical compositions of the synthetic leach liquor. The experiments shown in Table 5.1 labelled as FN refer to the precipitation reactions conducted in the Fe(III)+Ni(II) binary system, of which the initial synthetic leach solutions contain only ferric iron and nickel. These experiments served as a "baseline". Similarly, the experiments labelled as FNA and FNC represent the experiments carried out in the Fe(III)+Ni(II)+Al(III) and Fe(III)+Ni(II)+Cr(III) ternary systems, respectively.

Table 5.1: The initial and final chemical composition of synthetic leach liquor for single-stage precipitation experiments from the Fe(III)+Ni(II), Fe(III)+Ni(II)+Al(III) and Fe(III)+Ni(II)+Cr(III) systems.

Sample	Precipitation conditions		Initial (g/L)				Final (g/L)			
	pH	T(°C)	Fe	Ni	Al	Cr	Fe	Ni	Al	Cr
FN-1	3	25	29.9	4.9	N/A*	N/A	0.07	2.5	N/A	N/A
FNA-1	3	25	30.0	5.1	6.4	N/A	0.06	2.4	2.5	N/A
FNC-1	3	25	31.3	4.8	N/A	2.1	0.07	2.4	N/A	0.4
FN-2	4	25	29.9	4.9	N/A	N/A	0.01	2.3	N/A	N/A
FNA-2	4	25	30.0	5.1	6.4	N/A	0.004	2.3	0.2	N/A
FNC-2	4	25	29.4	4.9	N/A	2.0	0.01	2.2	N/A	0.01
FN-3	3	85	29.9	4.9	N/A	N/A	0.01	2.4	N/A	N/A
FNA-3	3	85	30.0	5.1	6.4	N/A	0.01	2.4	0.3	N/A
FNC-3	3	85	31.3	4.8	N/A	2.1	0.02	2.2	N/A	0.01

Table 5.1 continued.

FN-4	4	85	29.9	4.9	N/A	N/A	0.01	2.2	N/A	N/A
FNA-4	4	85	30.0	5.1	6.4	N/A	0.01	1.9	0.01	N/A
FNC-4	4	85	29.4	4.9	N/A	2.0	0.03	2.1	N/A	0.004

Note: * *N/A=Not Applicable to experiments.*

Table 5.2: Elemental analysis and metal recovery of the precipitates obtained for the single-stage precipitation from the Fe(III)+Ni(II), Fe(III)+Ni(II)+Al(III) and Fe(III)+Ni(II)+Cr(III) systems.

Sample	Elemental composition in final solid product (weight %)					Metal recovery * (%)			
	Fe	Ni	Al	Cr	Ca	Fe	Al	Cr	Ni
FN-1	18.71	0.01	N/A§	N/A	11.47	82.97	N/A	N/A	0.25
FNA-1	17.11	0.01	0.70	N/A	12.63	86.85	16.58	N/A	0.38
FNC-1	17.39	0.01	N/A	0.75	11.84	87.89	N/A	55.81	0.40
FN-2	18.45	0.04	N/A	N/A	11.97	92.74	N/A	N/A	1.35
FNA-2	13.61	0.05	2.54	N/A	13.04	94.43	82.70	N/A	1.93
FNC-2	16.92	0.05	N/A	1.13	11.45	91.17	N/A	87.68	1.67
FN-3	18.84	0.03	N/A	N/A	12.46	94.84	N/A	N/A	0.90
FNA-3	13.56	0.06	2.68	N/A	14.04	91.50	84.78	N/A	2.35
FNC-3	17.41	0.06	N/A	1.21	12.95	88.24	N/A	90.17	1.85
FN-4	18.26	0.23	N/A	N/A	12.34	97.40	N/A	N/A	7.50
FNA-4	13.02	0.27	2.73	N/A	14.50	95.42	93.75	N/A	11.67
FNC-4	17.09	0.27	N/A	1.21	12.04	95.92	N/A	97.94	9.15

Note: * *Weight of iron, aluminium, chromium and nickel in the final solid product relative to initial weight of iron, aluminium, chromium and nickel in the initial solution;* § *N/A=Not Applicable to experiments.*

Table 5.2 shows the elemental analysis of and metal recoveries to, the solid precipitation products for the single-stage precipitation of the Fe(III)+Ni(II),

Fe(III)+Ni(II)+Al(III) and Fe(III)+Ni(II)+Cr(III) systems. The experimental results indicate that increasing pH and temperature favour the removal of iron, aluminium and chromium, but at a cost of more nickel loss to the solids. Noticeably, the precipitation recoveries of aluminium and chromium were quite low at pH 3 and 25 °C with only 16.58% for aluminium (FNA-1) and 55.81% for chromium (FNC-1). Comparison of the results obtained in the Fe(III)+Ni(II)+Al(III) system (FNA-1 to FNA-4) and with those of the Fe(III)+Ni(II) system (FN-1 to FN-4) shows that more nickel was lost during iron and aluminium co-precipitation. A similar trend was noticed when comparing the results for the Fe(III)+Ni(II)+Cr(III) system (FNC-1 to FNC-4) to the Fe(III)+Ni(II) system (FN-1 to FN-4), where the loss of nickel increased during iron and chromium co-precipitation. Further comparison of the experimental results obtained in the Fe(III)+Ni(II)+Al(III) system and the Fe(III)+Ni(II)+Cr(III) system show that the presence of aluminium ions in the initial solution resulted in more loss of nickel to the solids than when chromium was present. However, one exception is noted for the pair of experiments labelled as FNA-1 and FNC-1 a slightly higher nickel loss was recorded in the Fe(III)+Ni(II)+Cr(III) system when the precipitation reaction was conducted at pH 3 and 25 °C. As the level of nickel loss was quite low at this experimental condition, such inconsistency could be due to analytical variation.

In Chapter 4, the effect of Fe/Ni ratio in the initial leach liquor on nickel loss was discussed. Similarly, the Al/Ni and Cr/Ni ratios are expected to influence the nickel loss as well. In a more complicated Fe(III)+Ni(II)+Al(III)+Cr(III) quaternary system, for example, interactions of aluminium and chromium during co-precipitation may also occur. Therefore, further investigation of the Fe(III)+Ni(II)+Al(III)+Cr(III) quaternary system with various Al/Ni and Cr/Ni ratios is necessary.

5.3.2 Statistically-designed experiments

In order to examine the effects of Al/Ni and Cr/Ni ratios on nickel loss, a series of experiments with various aluminium and chromium concentrations in the initial

synthetic leach liquors were performed using a two-factor full factorial design with replication. These experiments were conducted in the Fe(III)+Ni(II)+Al(III)+Cr(III) quaternary system at pH 4 and 85 °C, which aims to study the nickel loss under the conditions of maximum precipitation of aluminium and chromium.

Table 5.3: Factors and their levels for 2^2 replicated factorial design experiments.

Factors	Name	Low level (−)	High level (+)	Unit
A	Al concentration	3	10	g/L
B	Cr concentration	0.5	2.5	g/L

The two-factor full factorial design consists of all possible combinations of levels for all factors. The factors and their levels for this replicated factorial design experiment are shown in Table 5.3. All the factors were evaluated at a low level (denoted as '−') and a high level (denoted as '+'). The wide concentration ranges of aluminium and chromium ions used span those typical of leach liquors produced by heap and atmospheric leaching of nickel laterite ores using sulphuric acid. The experimental design matrix, and the initial and final chemical composition of the synthetic leach liquor is given in Table 5.4.

Table 5.4: The design matrix, initial and final chemical composition of synthetic leach liquor.

Sample	Matrix		Initial (g/L)				Final (g/L)			
	A	B	Fe	Ni	Al	Cr	Fe	Ni	Al	Cr
FD-1	−	−	30.1	5.1	2.9	0.5	0.002	1.9	0.005	0.001
FD-2	+	−	30.0	5.1	9.9	0.5	0.002	1.6	0.002	0.001
FD-3	−	+	29.3	4.9	2.9	2.5	0.005	1.9	0.002	0.001
FD-4	+	+	30.1	5.0	9.9	2.5	0.002	1.5	0.002	0.001
FD-5	−	−	30.1	5.1	2.9	0.5	0.006	1.9	0.002	0.001
FD-6	+	−	30.0	5.1	9.9	0.5	0.008	1.7	0.003	0.001
FD-7	−	+	29.3	4.9	2.9	2.5	0.006	1.8	0.005	0.001
FD-8	+	+	30.1	5.0	9.9	2.5	0.003	1.4	0.003	0.001

Table 5.5: The elemental analyses for 2^2 replicated factorial design experiments to investigate the effects of iron, aluminium and chromium on nickel losses.

Sample	Elemental composition in final solid product (weight %)					Ni loss to solid (%)*
	Fe	Ni	Al	Cr	Ca	
FD-1	12.41	0.24	1.19	0.22	15.77	10.73
FD-2	11.05	0.24	3.49	0.20	15.65	12.83
FD-3	11.30	0.21	1.09	0.91	16.18	11.29
FD-4	10.73	0.24	3.31	0.88	14.08	13.28
FD-5	12.35	0.24	1.21	0.23	16.07	10.93
FD-6	11.28	0.25	3.59	0.21	14.60	12.08
FD-7	13.04	0.24	1.19	0.99	14.70	10.85
FD-8	10.69	0.25	3.35	0.87	13.85	13.75

*Note: * Weight of nickel in the final solid product relative to initial weight of nickel in the initial solution.*

Table 5.6: Analysis of variance (ANOVA) for the results obtained in the 2^2 replicated factorial design experiments *.

Source	Sum of Squares	DF	Mean Square	*F* value	*P* Value Prob>F	Significance at =0.05
Factor-A	8.12	1	8.12	68.17	0.0012	S
Factor-B	0.90	1	0.90	7.54	0.0516	NS
AB interaction	0.30	1	0.30	2.55	0.1853	NS
Pure error	0.48	4	0.12			
Corrected Total	9.80	7				

*Note:*DF=degree of freedom; Prob=Probability; S=significant; NS=Non-Significant.*

The main response under investigation was the percentage of nickel loss to the solid, with the results given in Table 5.5. The statistical significance of each factor and their interactions were assessed by Fisher's *F*-test, with the analysis of variance (ANOVA) results given in Table 5.6. Normally, a *p*-value less than 0.05 (95% confidence level) indicates statistical significance. For the factor ranges studied, the effect of aluminium was found to be statistically significant for nickel loss (%), whereas the interaction between aluminium and chromium showed statistical insignificance. The effect of chromium was considered to be statistically insignificant, even though it had a borderline *p*-value. In addition, the effect of aluminium was found to be positive, suggesting that increasing the amount of aluminium in the initial leach liquors resulted in more nickel loss. This result, to some extent, is in agreement with an observation in the bench-scale test work of iron/aluminium removal for Mesaba Copper-Nickel Project (Mayhew *et al.*, 2009), although the iron levels were much lower than nickel AL liquors. Iron and aluminium were removed by a two-stage precipitation process at pH 5 and 40 ºC, the level of nickel loss in the second stage was found to be highly dependent on the aluminium concentration in the feed solution, such that more nickel loss occurred when the aluminium concentration increased (Mayhew *et al.*, 2009).

5.3.3 Multi-stage precipitation experiments

Previous sections confirmed the presence of aluminium ions in the leach solution containing iron, aluminium, chromium and nickel ions exerts a significant impact on nickel loss. Temperature and pH are two significant factors affecting each other in controlling the precipitation of metallic ions. Higher temperatures favour the removal of iron, aluminium and chromium, but at a cost of more nickel loss to the solids. Aluminium often requires a higher precipitation pH compared to iron, *i.e.* pH 4 to 5 for aluminium and 2.5 to 3.5 for ferric iron (Steemson and Smith, 2009). Thus, it becomes feasible to design and develop a multi-precipitation process to remove iron, aluminium and chromium in different stages operated under these conditions with various temperature and pH. Table 5.7 shows some strategies for a two-stage precipitation process conducted in the Fe(III)+Ni(II)+Al(III)+Cr(III) quaternary system using stepwise changes in temperature and pH. The central concept behind the design of these multi-stage precipitation processes is to minimize the loss of nickel by precipitating iron, aluminium and chromium in different stages: the majority of iron together with some aluminium and chromium are expected to be precipitated in the first stage; the residual iron and significant fractions of aluminium and chromium are expected to be removed in the second stage.

Table 5.7: The experimental strategy for multi-stage precipitation processes.

Precipitation route	Multi-stage precipitation procedure			
	Stage 1-pump and neutralize 500 mL leach solution within 2.5 hours		Stage 2-Ageing 1 hour	
	pH	Temp. (ºC)	pH	Temp. (ºC)
Route-1	3.0	25	4.0	25
Route-2	3.0	25	3.0	85
Route-3	3.0	55	3.0	85
Route-4	2.5	85	3.0	85
Route-5	3.0	85	2.5	85

For Route-1 to Route-4 listed in Table 5.7, the first stage precipitations are designed to be conducted under a relatively low pH and/or temperature conditions to remove the major part of iron without losing significant nickel to the precipitates. The second stage with higher pH and/or temperature aims to reject most of the aluminium and chromium. For Route-5, a different precipitation strategy is introduced in which precipitation is conducted in a higher pH environment for the first stage and then in a lower pH value for the second stage. As the pH is lowered, some solid products precipitated from the first stage precipitation process could be redissolved to release the co-precipitated nickel into solution. This process is expected to inhibit further co-precipitation of nickel during the second stage. It should be noted that in order to minimise the redissolution of already precipitated metal (iron, aluminium and chromium) oxides, oxyhydroxide and/or oxyhydroxysulphate in the first stage, the pH value of the second stage of Route 5 is chosen to be 2.5 rather than a lower value.

For comparison, the single-stage precipitation experiments corresponding to each pH and temperature combination given in Table 5.7 were carried out as well. Both single- and multi-stage precipitation experiments were conducted in the Fe(III)+Ni(II)+Al(III)+Cr(III) quaternary system, with the initial and final chemical compositions given in Table 5.8. The corresponding elemental analyses of the solid products obtained and the metal recoveries are given in Table 5.9.

The first five experiments labelled as FNAC-1 to FNAC-5 shown in Tables 5.8 and 5.9 referred to the single-stage precipitation, while the last five experiments labelled as FNAC-M-1 to FNAC-M-5 represented the multi-stage precipitation. As can be seen from Table 5.9, above 80% iron and generally above 90% of the iron can be removed in all single- and multi-stage precipitation processes. For the single-stage precipitation experiments, a considerable amount of aluminium still remained in the solution for the experiments labelled as FNAC-1, FNAC-3 and FNAC-4. Further comparison of the results for the experiments with the same precipitation pH but different temperatures (FNAC-1, FNAC-3 and FNAC-5) suggests that precipitation of aluminium together with chromium increased as the temperature increased from 25 to 85 ºC (Tables 5.8 and 5.9). As expected, higher pH and temperature favour the removal of iron, aluminium and chromium but at a cost of a higher level of nickel loss. Thus, the existing single-stage precipitation processes are not acceptable with respect to both the impurity removal and nickel loss.

Table 5.8: The initial and final chemical composition of synthetic leach liquor for the single-and multi-stage precipitation from the Fe(III)+Ni(II)+Al(III)+Cr(III) system *.

Sample	Stage-1		Stage-2		Initial (g/L)				Final (g/L)			
	pH	T(°C)	pH	T(°C)	Fe	Ni	Al	Cr	Fe	Ni	Al	Cr
FNAC-1	3.0	25	N/A	N/A	30.2	5.1	6.6	2.0	0.20	2.4	2.6	0.4
FNAC-2	4.0	25	N/A	N/A	30.2	5.1	6.6	2.0	0.02	2.2	0.5	0.02
FNAC-3	3.0	55	N/A	N/A	31.4	5.3	6.4	1.9	0.02	2.4	1.7	0.1
FNAC-4	2.5	85	N/A	N/A	31.4	5.3	6.4	1.9	0.1	2.4	2.2	0.3
FNAC-5	3.0	85	N/A	N/A	31.4	5.3	6.4	1.9	0.02	2.2	0.3	0.1
FNAC-M-1	3.0	25	4.0	25	32.5	5.8	6.6	2.0	0.02	2.4	0.1	0.02
FNAC-M-2	3.0	25	3.0	85	30.0	5.0	6.3	1.9	0.01	2.4	0.7	0.02
FNAC-M-3	3.0	55	3.0	85	31.4	5.3	6.3	1.9	0.01	2.4	0.4	0.03
FNAC-M-4	2.5	85	3.0	85	32.5	5.8	6.6	2.0	0.03	2.4	0.4	0.04
FNAC-M-5	3.0	85	2.5	85	31.4	5.3	6.3	1.9	0.01	2.3	0.2	0.03

*Note: *"FNAC" and "FNAC-M" refer to the single- and multi-stage precipitation experiments conducted in the synthetic leach solution containing Fe(III), Al(III), Cr(III) and Ni(II) ions, respectively; N/A=Not Applicable to experiments.*

The experimental results of multi-stage precipitation shown in Table 5.9 (FNAC-M-1 to FNAC-M-5) indicate a high level of metal removal with relatively minimal co-precipitation of nickel can be achieved. The concentrations of iron, aluminium and chromium ions in the solution after multi-stage precipitation all dropped to below 0.1 g/L, 1 g/L and 0.1 g/L, respectively (Table 5.8). The two experiments labelled as FNAC-M-1 and FNAC-M-3 shown in Table 5.9 achieved an acceptable level of nickel loss (<1%) and a desirable precipitation of iron, aluminium and chromium (as much as 95% iron and chromium together with above 80% aluminium). It is interesting to note that the single-stage precipitation conducted at pH 3 and 85 ºC resulted in 3.73% nickel loss (FNAC-5), while the value of nickel loss dropped to 2.16% for a multi-stage precipitation conducted at pH 3 and 85 ºC first followed by

pH 2.5 and 85 ºC (FNAC-M-5). This suggests that the second stage processing with lower pH value redissolved some of the precipitates formed in the first stage precipitation, and liberated some of the co-precipitated nickel.

Table 5.9: Elemental analysis of the precipitates obtained and metals removal for the single- and multi-stage precipitation from the Fe(III)+Ni(II)+Al(III)+Cr(III) system.

Sample	Elemental composition in final solid product (weight %)					Metal recovery * (%)			
	Fe	Ni	Al	Cr	Ca	Fe	Al	Cr	Ni
FNAC-1	15.11	0.02	0.65	0.68	13.88	84.25	16.66	57.12	0.59
FNAC-2	13.89	0.08	2.48	0.85	13.91	97.80	78.88	93.74	3.06
FNAC-3	15.92	0.03	1.14	0.73	12.98	95.99	35.48	74.66	1.13
FNAC-4	16.65	0.03	1.72	0.69	12.06	89.78	47.95	63.06	0.94
FNAC-5	14.21	0.09	2.47	0.76	13.28	96.14	82.11	85.24	3.73
FNAC-M-1	13.19	0.02	2.52	0.80	14.28	95.26	89.44	94.75	0.67
FNAC-M-2	13.37	0.01	2.15	0.77	13.58	94.51	73.15	96.98	0.60
FNAC-M-3	13.90	0.02	2.31	0.82	13.78	95.66	82.19	94.74	0.95
FNAC-M-4	13.07	0.05	2.32	0.78	14.78	93.33	81.22	92.06	1.89
FNAC-M-5	13.57	0.05	2.31	0.77	13.84	97.75	86.12	93.48	2.16

*Note: * Weight of iron, aluminium, chromium and nickel in final solid product relative to initial weight of iron, aluminium, chromium and nickel in the initial solution.*

The aggregation and settling of fine solid colloidal particles (insoluble particles that remain suspended in water) is normally achieved by the addition of high molecular weight polymers, or “flocculants”. It is a key step in hydrometallurgical processing, being essential to economic and effective solid-liquid separation by gravity thickening. Four mechanisms are often involved in a flocculation process: polymer bridging, charge neutralization, polymer complex formation, and flocculation by free polymer (Gregory, 1985). The first two mechanisms have received the most attention and are probably more significant than the other mechanisms. The settling rate is a key parameter to estimate the efficiency of flocculation.

The results of settling rate tests for the precipitates produced from the current experiments are outlined in Table 5.10. These indicate that the settling rate is improved by increasing precipitation temperature (compare tests FNAC-1, FNAC-3 and FNAC-5) and particularly by using 4 mL cationic polymer FO 4190 VHM compared to 2 mL as flocculant (all tests). These effects may relate to colloid stability and change in the flocculation mechanism. High molecular weight cationic flocculants normally represent the convergence of bridging and charge neutralization mechanisms (Mangravite *et al.*, 1985). The early patent on the E.Z. Goethite Process to remove ferric iron from an iron-bearing acid leaching solutions by Allen *et al.* (1970) showed that the sludge obtained by operating the precipitation process within the range of pH from 1.7 to 3.5 and temperature from 50 °C to the boiling point can settle rapidly with the aid of a flocculant. For example, the addition of a high molecular weight polyacrylamide non-ionic polymer, Separan M.G.L., was found to be effective with settling rates of up to 3.3 m/h. Fast settling rates were also observed in the present work when using a similar non-ionic polymer as flocculant, such as the samples obtained at elevated temperatures (FNAC-3 to FNAC-5, FNAC-M-3 to FNAC-M-5). For the settling rates of the sludge obtained from multi-stage precipitation processes (FNAC-M-1 to FNAC-M-5), the final settling rates seem to be highly dependent on the first stage of the precipitation process, where the major portion of iron is hydrolysed and precipitated. For instance, when adding 4 mL cationic flocculant, the single-stage precipitations conducted at pH 3 and 25 °C (FNAC-1), and pH 3 and 85 °C (FNAC-5) showed a settling rate of 0.38 m/h and 6.11 m/h, respectively. However, an intermediate settling rate of 1.92 m/h was recorded by a multi-stage precipitation process conducted at pH 3 and 25°C for the first stage and then pH 3 and 85°C for the second stage (FNAC-M-2).

Table 5.10: Settling rates obtained for single- and multi-stage precipitates from the Fe(III)+Ni(II)+Al(III)+Cr(III) system.

Sample	Stage-1		Stage-2		Settling rate (m/h)			
					Flocculant-1 *		Flocculant-2 §	
	pH	T(°C)	pH	T(°C)	2 mL ¤	4 mL ¤	2 mL ¤	4 mL ¤
FNAC-1	3.0	25	N/A§	N/A	0.12	0.15	0.25	0.38
FNAC-2	4.0	25	N/A	N/A	0.10	0.14	0.26	0.35
FNAC-3	3.0	55	N/A	N/A	1.81	2.37	2.99	4.32
FNAC-4	2.5	85	N/A	N/A	4.01	4.78	6.01	7.89
FNAC-5	3.0	85	N/A	N/A	2.73	3.38	4.49	6.11
FNAC-M-1	3.0	25	4.0	25	0.15	0.21	0.24	0.36
FNAC-M-2	3.0	25	3.0	85	0.29	0.49	1.27	1.92
FNAC-M-3	3.0	55	3.0	85	1.95	2.75	4.14	5.05
FNAC-M-4	2.5	85	3.0	85	3.82	4.46	5.10	7.42
FNAC-M-5	3.0	85	2.5	85	2.98	3.05	4.36	6.80

*Note: * Flocculant-1 refers to non-ionic flocculant FA 920 VHM; § Flocculant-2 represents cationic flocculant FO 4190 VHM; ¤ Add 2 or 4 mL 0.025% flocculant to 250 mL sludge*; § *N/A=Not Applicable to experiments.*

As mentioned before, one aim of this chapter is to develop a multi-stage precipitation process to remove impurities efficiently without causing significant losses of nickel, and produce precipitation sludge with a fast settling rate. In terms of impurity removal, multi-stage precipitation experiments labelled as FNAC-M-1, FNAC-M-3, FNAC-M-4 and FNAC-M-5 achieved satisfactory results precipitating above 90% iron and chromium, and 80% aluminium (Table 5.9). According to the loss of nickel to the solids, multi-stage precipitation experiments labelled as FNAC-M-1, FNAC-M-2 and FNAC-M-3 showed acceptable levels of nickel losses (<1%) (Table 5.9). On the base of settling rate, the sludge obtained from the multi-stage precipitation experiments labelled as FNAC-M-3, FNAC-M-4 and FNAC-M-5 showed faster

settling rate (Table 5.10). However, in terms of the impurity removal, the level of nickel loss and settling rate, the multi-stage precipitation experiment labeled as FNAC-M-3 is found to be most attractive compared to other multi-stage precipitation processes.

Table 5.11: Chemical composition of real leach solutions obtained by atmospheric column leaching of Western Australian laterite ores (after 135 days).

Real Leach Solution-A *		Real Leach Solution-B §	
Elements	Concentration (g/L)	Elements	Concentration (g/L)
Fe	40.7	Fe	36.8
Ni	2.64	Ni	1.18
Co	0.17	Co	0.08
Al	2.71	Al	4.01
Cr	0.66	Cr	0.76
Mn	0.64	Mn	0.59
Mg	7.42	Mg	1.04

*Note: * Real leach solution-A is produced from sulphuric acid leaching of nontronite type ore; § Real leach solution-B is produced from sulphuric acid leaching of limonite type ore.*

To further test the multi-stage precipitation procedure, more experiments were performed on real leach solutions using a similar experimental procedure to that used for experiment FNAC-M-3. That is the first stage precipitation was conducted at pH 3 and 55 ºC, while the second stage precipitation was carried out at pH 3 and 85 ºC. For comparison, the corresponding single-stage precipitation at each pH and temperature were carried out as well. Stock pregnant leach solutions were used with the chemical composition as given in Table 5.11. These were obtained from atmospheric sulphuric acid column leaching experiments of Western Australian laterite ores (135 days) conducted at CSIRO Process Science and Engineering. The initial concentrations of iron and chromium are almost similar, but the concentrations

of nickel and aluminium are different in these two real leach liquors, which give different Fe/Ni, Al/Ni and Cr/Ni ratios. Table 5.12 to 5.14 show the results obtained from both single- and multi-stage precipitation using the real leach solutions. Table 5.15 gives the results of settling rate tests.

Table 5.12: The final chemical composition of real leach solutions for the single- and multi-stage precipitation*.

Sample	Stage-1		Stage-2		Final concentration (g/L)						
	pH	T(°C)	pH	T(°C)	Fe	Al	Cr	Mg	Mn	Ni	Co
RLS-A-S-1	3.0	55	N/A	N/A	0.02	0.6	0.08	3.3	0.3	1.1	0.07
RLS-A-S-2	3.0	85	N/A	N/A	0.01	0.2	0.03	3.3	0.3	1.0	0.07
RLS-A-M-1	3.0	55	3.0	85	0.01	0.2	0.02	3.2	0.3	1.1	0.07
RLS-B-S-1	3.0	55	N/A	N/A	0.01	0.8	0.07	0.5	0.3	0.5	0.03
RLS-B-S-2	3.0	85	N/A	N/A	0.01	0.2	0.04	0.5	0.3	0.4	0.03
RLS-B-M-1	3.0	55	3.0	85	0.002	0.3	0.03	0.5	0.3	0.5	0.03

*Note: * N/A=Not Applicable to experiment*

Table 5.13: Elemental analysis of the precipitates obtained for the single- and multi-stage precipitation from real leach solutions §.

Sample	Elemental composition in final solid product (weight %)							
	Fe	Al	Cr	Mg	Mn	Ni	Co	Ca
RLS-A-S-1	10.59	0.33	0.14	BDL	BDL	0.006	BDL	18.06
RLS-A-S-2	10.36	0.59	0.15	BDL	BDL	0.02	BDL	17.91
RLS-A-M-1	10.19	0.59	0.16	BDL	BDL	0.008	BDL	17.97
RLS-B-S-1	10.30	0.49	0.17	BDL	BDL	0.003	BDL	17.87
RLS-B-S-2	10.04	0.99	0.19	BDL	BDL	0.01	BDL	17.23
RLS-B-M-1	10.00	0.96	0.20	BDL	BDL	0.003	BDL	17.70

Note: § BDL=below detection limit (0.002%).

Table 5.14: Metal recovery for the single- and multi-stage precipitation from real leach solutions.

Sample	Metal recovery (%)			
	Fe	Al	Cr	Ni
RLS-A-S-1	95.97	44.93	76.27	0.88
RLS-A-S-2	96.31	82.34	87.18	2.81
RLS-A-M-1	96.20	83.29	93.67	1.13
RLS-B-S-1	94.26	41.01	75.43	0.85
RLS-B-S-2	95.60	86.82	88.44	3.10
RLS-B-M-1	97.62	85.65	92.65	0.98

Table 5.15: Settling rate obtained for the single- and multi-stage precipitation from real leach liquor system.

Sample	Stage-1		Stage-2		Settling rate (m/h)			
					Flocculant-1 *		Flocculant-2 §	
	pH	T(°C)	pH	T(°C)	2 mL ¤	4 mL ¤	2 mL ¤	4 mL ¤
RLS-A-S-1	3.0	55	N/A#	N/A	1.22	1.45	2.22	3.16
RLS-A-S-2	3.0	85	N/A	N/A	2.72	3.13	3.62	5.40
RLS-A-M-1	3.0	55	3.0	85	1.32	2.12	2.50	4.49
RLS-B-S-1	3.0	55	N/A	N/A	1.34	1.67	2.64	3.76
RLS-B-S-2	3.0	85	N/A	N/A	2.44	2.88	3.14	5.03
RLS-B-M-1	3.0	55	3.0	85	1.57	1.72	2.71	4.04

*Note: * Flocculant-1 refers to non-ionic flocculant FA 920 VHM; § Flocculant-2 represents cationic flocculant FO 4190 VHM; ¤ Add 2 or 4 mL 0.025% flocculant to 250 mL sludge*; *# N/A=Not Applicable to experiments.*

Comparison of the results of the single- and multi-stage precipitation experiments performed on the real leach solutions (Tables 5.12 to 5.15) suggests that even with the higher initial iron concentration, and different Fe/Ni, Al/Ni and Cr/Ni ratios,

satisfactory precipitation recoveries of iron, aluminium and chromium, acceptable level of nickel loss to the solids, and fast settling rate can still be achieved using a multi-stage precipitation process. It was also noted that the nickel losses here were slightly higher than the synthetic system. This may, at least in part be due to the higher ferric iron concentrations in the initial PLS (higher Fe/Ni ratio), which is in agreement with the observation in Chapter 4.

The results of multi-stage precipitation on both synthetic and real leach solutions presented here showed that the loss of nickel to the solids can be reduced by carefully controlling pH and temperature. Although the experiments conducted in this study all used the semi-batch precipitation procedures, this provides baseline laboratory data for industrial application as a fully continuous pilot-plant scale precipitation process. An example of this would be continuous stirred tank reactors (CSTR) which can be arranged in parallel or series. The pregnant leach solution can be processed with different treatments (*e.g.* pH and temperature) from one reactor to the next. The slurry produced from the last reactor can be recycled to the first reactor to act as seeds to increase the precipitation kinetics and improve crystallinity of the precipitates. In addition, on an industrial scale, the factors such as the reactor capacity, the consumption of neutralizing agent, and the cost of energy, should also be taken into account to develop and optimize an effective impurity removal process.

5.4 CONCLUSION

The results obtained within this chapter answer the two questions posed: what are the effects of iron, aluminium and chromium co-removal upon nickel losses, and how to develop a precipitation process with desirable precipitation recoveries of impurities, acceptable level of nickel loss to the solids, and satisfactory sludge property?

Comparison of the results of the precipitation experiments conducted in the Fe(III)+Ni(II), Fe(III)+Ni(II)+Al(III), and Fe(III)+Ni(II)+Cr(III) systems shows that

greater loss of nickel to the solids occurred in the presence of aluminium and chromium. In a more complicated Fe(III)+Ni(II)+Al(III)+Cr(III) quaternary system, the presence of aluminium was more significant in impacting the level of nickel loss. Increasing the concentration of aluminium in the initial pregnant leach solution resulted in more nickel loss. However, the presence of chromium and the interactions between aluminium and chromium statistically had little influence on nickel loss. This suggests that when a precipitation reaction occurs in a mixed sulphate solution containing iron, aluminium, chromium and nickel ions, the loss of nickel is mainly associated with iron and aluminium co-precipitation.

Further experiments performed in the Fe(III)+Ni(II)+Al(III)+Cr(III) quaternary system showed that 84% iron can be easily removed by simply raising the pH to 3 at 25 ºC, but the precipitation recoveries of aluminium and chromium were quite low at 17% and 57%, respectively. Increasing temperature favours the precipitation of aluminium and chromium. About 82% aluminium and 85% chromium can be removed from solution at pH 3 and 85 ºC, however, the loss of nickel to the solid was substantial at about 4%. By carefully controlling pH and temperature in multi-stage precipitation processes, the iron, aluminium and chromium can be effectively rejected with a minimal level of nickel loss and desirable sludge properties. The optimum conditions for a multi-stage precipitation process were found to be at pH 3 and 55 ºC in the first stage followed by a second stage operated at pH 3 and 85 ºC. Using this multi-stage precipitation procedure, as much as 95% iron and chromium together with above 80% aluminium can be removed, the level of nickel loss to the solid can be reduced to below 1%. The precipitate sludge showed a fast settling rate of 5.05 m/h with the addition of a cationic flocculant. Similar satisfactory results were also obtained when performing this multi-stage precipitation procedure on real leach solutions. The multi-stage precipitation process reported in this chapter has potential industrial application. It can be easily performed in continuous reactors which are arranged in parallel or series having varied pH and temperature control.

CHAPTER 6

THE EFFECT OF WATER SALINITY ON IRON, ALUMINIUM AND CHROMIUM CO-REMOVAL AND ASSOCIATED NICKEL LOSSES

6.1 INTRODUCTION

As outlined in Chapter 1, the majority of the world's nickel resources are present in lateritic deposits. In a nickel laterite profile, nickel and cobalt are hosted by limonite, asbolite, and nontronite ores which are amenable to hydrometallurgical processing methods such as acid leaching (Dalvi *et al*., 2004). The nature of hydrometallurgical processes involves the extraction of metals into aqueous solution. However, nickel-rich laterite ores are not often located in areas where large quantities of good quality fresh water are available. For example, in the arid regions of Australia, only hypersaline underground water may be available in significant amounts, and in Indonesia and the Philippines where laterite deposits occur on small islands, only large quantities of seawater are available (Liu, 2006). Thus, the water used for processing these laterites with sulphuric acid has often been saline, ranging from low to very high concentration of total dissolved salts (TDS). TDS is normally related to sodium chloride content, but also other salts such as magnesium chloride or potassium chloride and related sulphates can occur in small concentrations. According to the United States Geological Survey (2005), saline water can be classified into three categories: slightly saline water (1 to 3 g/L TDS), moderately saline water (3 to 10 g/L TDS), and highly saline water (10 to 35 g/L TDS). Seawater has a salinity of about 35 g/L. Hypersaline water refers to water having a greater salinity than seawater.

Since the late 1990s, a considerable amount of research has been undertaken

investigating the hydrometallurgical processing of Western Australia laterites using saline and/or hypersaline waters. Johnson *et al*. (2002) provided a systematic study of the effect of process water salinity on leaching kinetics and acid consumption during high pressure acid leaching of Cawse ores. The ore was leached at 250 ºC with sulphuric acid in process water ranging from tap water (<1 g/L Na) to concentrated hypersaline groundwater (~60 g/L Na). Acid consumption was found to increase as the salinity of the process water increased. The extraction of nickel was dependent on salinity with 95% extracted using tap water and 96% when seawater (11 g/L Na) was used. However, extraction dropped to 91% in higher saline water. The Bulong Nickel Operation located in the arid region of Western Australia was a unique plant that processed clay-rich laterite ores (a significant amount of nontronite clay and goethite with some maghemite and serpentine) using hypersaline waters. Whittington *et al*. (2003a) examined the effect of water salinity on the reactions occurring during the pressure acid leaching of Bulong laterite ores. Particular emphasis was placed on the effect of the water salinity on the process chemistry and residue mineralogy. The results showed that water salinity significantly affected the leaching (*e.g.* acid consumption and metal extraction). Leaching in hypersaline water resulted in the formation of amorphous silica with sodium jarosite and hematite, whereas leaching in less saline water favoured the formation of amorphous silica and hematite, with lesser amounts of sodium/hydronium alunite/jarosites.

Attention has also been focused on using saline water to treat laterite ores during atmospheric leaching. The use of sea water for heap leaching of nickeliferous oxide ores was first introduced by Agatzini-Leonardou and Dimaki in 2000 (Agatzini-Leonardou and Dimaki, 2000). The nickel and/or cobalt were extracted from ores by heap leaching with a dilute sulphuric acid solution prepared from sea water at ambient temperature. Another patent application by BHP Billiton reported a process for heap leaching of nickeliferous oxidic ores using a hypersaline water sulphuric acid lixiviant (Liu, 2006). The preferred concentration of TDS for the hypersaline water in this process is from 40 to 200 g/L, and most preferably from 50 to 150 g/L.

The laboratory data obtained from the column leaching of arid-region Australia ores (10 kg of agglomerated ores were fed into eight columns with 100 mm diameter and 1.86 m height to simulate heap leaching conditions) showed improved nickel recovery was achieved when hypersaline water was used together with sulphuric acid. Similar good results were obtained when using hypersaline water and hydrochloric acid as lixiviant. A recent patent, application also assigned to BHP Billiton, described an atmospheric leaching process for the recovery of nickel and cobalt from laterite ores using hypersaline water (Liu and Reynolds, 2011). These atmospheric sulphuric agitation leach tests were performed on laterite ores from Ravensthorpe Nickel Operations in Western Australia. The ores were separated into high-iron and low-magnesium (>25 wt% Fe and 0.5-6 wt% Mg) and low-iron and high-magnesium (5-20 wt% Fe and >8 wt% Mg) fractions. Each fraction was separately slurried with hypersaline water having a preferable TDS concentration ranging from 50 to 150 g/L. The limonite slurry was first leached at a temperature between 95 to 105 ºC using sulphuric acid. The free acid remaining was neutralized using the saprolite fraction of the ore in the second leach stage, during which iron was also precipitated as jarosite. The results obtained showed that the overall nickel and cobalt extractions were greater than 87% and 88%, respectively.

Hypersaline water provides large amounts of monovalent cations (*e.g.* Na^+ and K^+) and chloride ions. In the presence of the monovalent ions, the formation of jarosite-type compounds ($MFe_3(OH)_6(SO_4)_2$, where *M* refers to Na^+, K^+, NH_4^+, Ag^+ or H_3O^+, *etc.*) is favoured at lower pH value (<pH 2) and elevated temperature (>80 ºC) (Dutrizac and Jambor, 2000). If the jarosite-type compounds are the preferable phases of iron precipitates obtained from a laterite leach solution with high salinity, it is critical that the solid precipitation products do not contain significant amounts of nickel and cobalt. In this regard, the laboratory investigation on the behavior of nickel and cobalt during jarosite precipitation by Dutrizac and Chen (2004) showed that minor amounts of nickel and cobalt are structurally incorporated into sodium jarosite, potassium jarosite and ammonium jarosite. The extent of incorporation

increases as the concentration of dissolved nickel and cobalt increases.

Previous chapters studied the relationships between impurity removal and associated nickel losses in sulphate leaching systems. This chapter provides an experimental investigation on the impurity removal from synthetic sulphate leach solutions with the presence of various amounts of salts (as sodium chloride). Aims of this chapter were to study the effect of water salinity on 1) impurity removal efficiency and associated nickel losses; 2) the mineralogy changes of the precipitates. The latter was based on X-Ray Diffraction (XRD) data only, which was similar to the mineralogical study section in Chapter 4. More detailed mineralogical characterization involving an acid dissolution technique, Difference X-Ray Diffraction (DXRD), microscopic analysis and Fourier Transform Infra-Red (FTIR) spectroscopy is discussed in Chapter 7.

6.2 EXPERIMENTAL

All the precipitation experiments conducted in this chapter used a single-stage precipitation process which was similar to the semi-batch precipitation procedure used in Chapters 4 and 5. The synthetic pregnant leach solutions were prepared by dissolving $Fe_2(SO_4)_3 \cdot xH_2O$, $NiSO_4 \cdot 6H_2O$, $Al_2(SO_4)_3 \cdot 18H_2O$ and $Cr_2(SO_4)_3 \cdot xH_2O$ to give a concentration of 30 g/L Fe^{3+}, 5 g/L Ni^{2+}, 6.0 g/L Al^{3+}, and 2 g/L Cr^{3+}. A specific amount of sodium chloride was added to provide the required solution TDS. For each experiment, a volume of 500 mL of synthetic leach solutions was pumped into a baffled reaction vessel containing a pre-determined amount of de-ionized water over a period of 2.5 hours. A $CaCO_3$ (25% w/w) suspension in de-ionized water was simultaneously pumped into the reaction vessel to reach the target pH values. The temperature was controlled using an oil bath. At the completion of the reaction, the resulting slurry was vacuum filtered through a 0.45 µm Gelman Supor® membrane. The metal concentrations in the filtrate were analysed by ICP-OES, and the filter cake was carefully washed with large amounts of de-ionized water then

dried overnight at 60 ºC. The chemical composition of the dried solid products was determined by ICP-OES after aqua regia digestion.

Dried solid samples were submitted to X-Ray Diffraction (XRD) analysis using a PANalytical Empyrean diffractometer. Additional washing was performed to remove gypsum from these samples before XRD analysis. All XRD patterns were collected using CoKα radiation at 45 kV and 40 mA with a step scan of 0.02º.

6.3 RESULTS AND DISCUSSION

6.3.1 Preliminary precipitation experiments

Preliminary precipitation experiments were conducted with the aim of estimating the effect of water salinity on impurity removal efficiency and associated nickel losses. The salinity was adjusted by adding various amounts of sodium chloride into synthetic sulphate leach solutions containing iron, aluminium, chromium and nickel ions. The concentration of sodium chloride varied from 30 to 150 g/L, simulating salinity ranging from sea water to hypersaline water. Some experimental data obtained from the Fe(III)+Ni(II)+Al(III)+Cr(III) sulphate system in Chapter 5, that contained no sodium chloride, were used here to serve as “baselines” for comparison. The experimental conditions are given in Table 6.1.

Table 6.1: Summary of the initial and final chemical composition of synthetic leach solutions for the study of the effects of water salinity.

Sample	Precipitation conditions		Initial (g/L)					Final (g/L)				
	pH	T(°C)	Fe	Ni	Al	Cr	Na	Fe	Ni	Al	Cr	Na
FNAC-1‡	3	25	30.2	5.1	6.6	2.0	N/A	0.2	2.4	2.6	0.4	N/A
ES-1	3	25	30.6	5.0	6.2	1.9	11.9	0.3	2.3	2.4	0.4	4.8
ES-2	3	25	30.1	5.1	6.1	1.9	35.6	0.3	2.3	2.3	0.3	14.0
ES-3	3	25	30.2	5.0	6.1	1.9	58.8	0.3	2.3	2.3	0.3	23.4

Table 6.1 continued.

FNAC-3‡	3	55	31.4	5.3	6.4	1.9	N/A	0.02	2.4	1.7	0.1	N/A
ES-4	3	55	30.6	5.0	6.2	1.9	11.9	0.02	2.3	1.6	0.1	4.7
ES-5	3	55	30.1	5.1	6.1	1.9	35.6	0.05	2.3	1.7	0.1	14.8
ES-6	3	55	30.2	5.0	6.1	1.9	58.8	0.02	2.3	1.6	0.1	23.0
FNAC-5‡	3	85	31.4	5.3	6.4	1.9	N/A	0.02	2.2	0.3	0.1	N/A
ES-7	3	85	30.6	5.0	6.2	1.9	11.9	0.02	2.1	0.3	0.05	4.7
ES-8	3	85	30.1	5.1	6.1	1.9	35.6	0.04	2.2	0.5	0.1	14.3
ES-9	3	85	30.2	5.0	6.1	1.9	58.8	0.03	2.1	0.4	0.1	22.9

Note: ‡ Data was sourced from Table 5.8 of Chapter 5; N/A=Not Applicable to experiments.

Table 6.2 shows the elemental analysis and metal recoveries. The precipitation experiments were all conducted at a pH of 3 though at different temperatures. The general comments regarding the metal recoveries outlined in Table 6.2 are that increasing temperature favours the removal of iron, aluminium and chromium, but at a cost of more nickel loss to solid. Comparison of experimental results obtained from synthetic leach solutions with and without the presence of sodium chloride, as given in Table 6.2, shows there were no significant differences in the recoveries of iron, aluminium and chromium when the precipitation experiments were conducted at 25 ºC (FNAC-1, ES-1, ES-2 and ES-3). However, when the precipitation reactions were carried out at elevated temperatures, particularly at 85 ºC (FNAC-5, ES-7, ES-8 and ES-9), higher recoveries of iron, aluminium and chromium appear to be achieved and this was marginally larger for higher salinities.

Table 6.2: Elemental analysis of the solid precipitation products and metal recovery for the study of the effects of water salinity.

Sample	Elemental composition in final solid product (weight %)						Metal recovery [§] (%)			
	Fe	Ni	Al	Cr	Ca	Na	Fe	Ni	Al	Cr
FNAC-1[‡]	15.11	0.02	0.65	0.68	13.88	N/A	84.25	0.59	16.66	57.12
ES-1	16.09	0.01	0.58	0.71	12.11	0.01	84.59	0.47	15.02	58.68
ES-2	16.01	0.01	0.63	0.71	12.89	0.01	83.17	0.34	16.12	58.15
ES-3	16.25	0.01	0.64	0.70	12.17	0.01	85.60	0.40	16.57	57.50
FNAC-3[‡]	15.92	0.03	1.14	0.73	12.98	N/A	95.99	1.13	35.48	74.66
ES-4	16.02	0.03	1.21	0.80	12.64	0.02	94.32	1.21	35.11	76.01
ES-5	16.49	0.03	1.23	0.80	12.41	0.02	95.59	0.86	35.05	75.42
ES-6	16.18	0.03	1.24	0.82	12.44	0.02	96.12	0.92	36.42	77.44
FNAC-5[‡]	14.21	0.09	2.47	0.76	13.28	N/A	96.14	3.73	82.11	85.24
ES-7	14.56	0.08	2.47	0.79	13.30	0.01	97.81	3.21	82.27	83.05
ES-8	14.71	0.07	2.49	0.80	13.17	0.02	97.40	2.90	81.20	86.81
ES-9	14.69	0.06	2.55	0.85	12.76	0.01	98.02	2.44	84.15	88.89

Note: [§] *Weight of iron, aluminium, chromium and nickel in the final solid product relative to initial weight of iron, aluminium, chromium and nickel in the initial solution;* [‡] *Data was sourced from Table 5.9 of Chapter 5*; *N/A=Not Applicable to experiments.*

The recovery of nickel (nickel loss to solid), follows the opposite trends, *i.e.* higher water salinity resulted in lower levels of nickel loss (Table 6.2). This trend became noticeable particularly when the precipitation reaction was conducted at 85 ºC from the synthetic leach solutions with highest salinity (*e.g.* FNAC-5 vs. ES-9). Similar results were found for the precipitation process following atmospheric acid leaching of nickel laterite using hypersaline water (Liu and Reynolds, 2011), in which improved nickel recovery and iron precipitation efficiency was achieved when using hypersaline water with total dissolved salt ranging from 40 to 200 g/L. However,

some exceptions were also noted for the pairs of experiments labelled as ES-2 and ES-3, FNAC-3 and ES-4. Slightly higher levels of nickel losses were recorded when the precipitation reactions were conducted from the solutions with the presence of more sodium chloride. In order to gain a better understanding of the effect of water salinity, further investigation is necessary to be performed in wider pH ranges.

6.3.2 Statistically-designed experiments

A three factor Box-Behnken Design (BBD) combined with a Response Surface Methodology (RSM) was employed to estimate the effect of water salinity on nickel losses for wider pH ranges. This experimental strategy was successfully applied to study the effect of iron precipitation on nickel losses in Chapter 4. Details of this design and modelling approach are given in Chapter 4 and Appendix B.

Fifteen experiments were carried out using synthetic leach solutions which were prepared by dissolving $Fe_2(SO_4)_3 \cdot xH_2O$, $NiSO_4 \cdot 6H_2O$, $Al_2(SO_4)_3 \cdot 18H_2O$ and $Cr_2(SO_4)_3 \cdot xH_2O$ to give a chemical composition of 30 g/L Fe^{3+}, 5 g/L Ni^{2+}, 6 g/L Al^{3+} and 2 g/L Cr^{3+}. These synthetic leach solutions have similar Fe/Ni, Al/Ni and Cr/Ni ratios. The salinity was adjusted by adding various amounts of sodium chloride. The factors investigated were pH, temperature and the initial concentration of sodium chloride. All factors were evaluated at three levels represented in coded form as −, 0 and +, corresponding to the low, medium, and high values, respectively, as shown in Table 6.3. The experimental design matrix is given in Table 6.4 and the initial and final chemical composition of synthetic leach solutions for each experiment in Table 6.5.

Table 6.3: Factors and their levels used in statistically-designed experiments.

Factor	Name	Low (−)	Medium (0)	High (+)	Unit
A	pH	2	3	4	pH units
B	Temperature	25	55	85	ºC
C	NaCl concentration	30	90	150	g/L

Table 6.4: Design matrix for 3 factors and 15 experiments.

Sample	Basic design		
	A	B	C
ES-1	0	−	−
ES-3	0	−	+
ES-5	0	0	0
ES-7	0	+	−
ES-9	0	+	+
ES-10	+	0	+
ES-11	+	0	−
ES-12	+	+	0
ES-13	−	0	+
ES-14	0	0	0
ES-15	−	0	−
ES-16	−	−	0
ES-17	0	0	0
ES-18	+	−	0
ES-19	−	+	0

Table 6.5: The initial and final chemical composition of synthetic leach solutions for statistically-designed experiments.

Sample	Initial (g/L)					Final (g/L)				
	Fe	Ni	Al	Cr	Na	Fe	Ni	Al	Cr	Na
ES-1	30.6	5.0	6.2	1.9	11.9	0.3	2.3	2.4	0.4	4.8
ES-3	30.2	5.0	6.1	1.9	58.8	0.3	2.3	2.3	0.3	23.4
ES-5	30.1	5.1	6.1	1.9	35.6	0.05	2.3	1.7	0.1	14.8
ES-7	30.6	5.0	6.2	1.9	11.9	0.02	2.1	0.3	0.05	4.7
ES-9	30.2	5.0	6.1	1.9	58.8	0.03	2.1	0.4	0.1	22.9
ES-10	30.2	5.0	6.1	1.9	58.8	0.01	2.0	0.1	0.003	23.8
ES-11	30.6	5.0	6.2	1.9	11.9	0.01	1.9	0.2	0.02	4.5
ES-12	29.8	4.8	6.2	1.9	33.8	0.002	1.7	0.01	0.01	13.7
ES-13	30.2	5.0	6.1	1.9	58.8	4.8	2.2	2.5	0.7	23.2
ES-14	30.1	5.1	6.1	1.9	35.6	0.07	2.2	1.5	0.1	14.4
ES-15	30.6	5.0	6.2	1.9	11.9	4.0	2.3	2.5	0.7	4.8
ES-16	30.1	5.1	6.1	1.9	35.6	10.1	2.4	2.7	0.8	15.9
ES-17	30.1	5.1	6.1	1.9	35.6	0.06	2.3	1.4	0.1	14.6
ES-18	29.8	4.8	6.2	1.9	33.8	0.02	2.0	0.4	0.02	13.2
ES-19	30.1	5.1	6.1	1.9	35.6	1.1	2.2	1.9	0.8	13.9

Table 6.6 shows the elemental analysis of precipitates and the level of nickel loss to the solids (studied response). Using these experimental results, and by employing the method of least squares, it is feasible to fit an empirical quadratic equation, as given by Eq. B.1 and detailed in Appendix B. As shown in Table 6.6, the range of response values were large, *i.e.* the ratio of maximum to minimum values is 423.5. Hence, a suitable transformation should be used to describe the response correctly. The Box-Cox method for data transformation, which was detailed in Chapter 4, was used to confirm transformation of the value of nickel loss onto a logarithmic scale (log nickel loss (%)). In addition, the levels of sodium in solid precipitates were quite low for most samples shown in Table 6.6, though an exception for sample ES-19 was noted. The high proportion of sodium in sample ES-19 may, at least in part be due to the

formation of a new mineral phase. Further investigation is therefore required to determine the mineralogical property of the precipitates obtained.

Table 6.6: Elemental analysis of the precipitates obtained and metal recovery for statistically-designed experiments.

Sample	Elemental composition in final solid product (weight %)						Nickel loss to solid [§]
	Fe	Ni	Al	Cr	Na	Ca	
ES-1	16.09	0.01	0.58	0.71	0.01	12.11	0.47
ES-3	16.25	0.01	0.64	0.70	0.01	12.17	0.40
ES-5	16.49	0.03	1.23	0.80	0.02	12.41	0.86
ES-7	14.56	0.08	2.47	0.79	0.01	13.30	3.21
ES-9	14.69	0.06	2.55	0.85	0.01	12.76	2.44
ES-10	13.67	0.07	2.61	0.85	0.01	13.26	3.03
ES-11	13.98	0.10	2.61	0.86	0.01	13.42	4.13
ES-12	13.40	0.19	2.76	0.87	0.03	12.52	8.47
ES-13	16.54	0.003	0.23	0.48	0.02	13.58	0.07
ES-14	16.66	0.03	1.30	0.85	0.01	12.30	0.93
ES-15	16.58	0.003	0.22	0.49	0.01	13.81	0.08
ES-16	16.30	0.002	0.06	0.40	0.02	13.46	0.02
ES-17	16.18	0.03	1.29	0.83	0.01	12.77	0.89
ES-18	13.63	0.05	2.41	0.85	0.03	13.39	1.98
ES-19	17.48	0.01	0.82	0.62	0.65	11.18	0.18

Note: [§] Weight of nickel in the final solid product relative to initial weight of nickel in the initial solution.

In order to investigate the effects of each factor and all the possible interactions on the response, an analysis of variance (ANOVA) was performed, with the results given in Table 6.7.

Table 6.7: Analysis of variance (ANOVA) for the quadratic regression model.

Source	Sum of squares	DF	Mean square	F Value	*p*-value Prob>F
Model	7.84	9	0.87	323.62	<0.0001
A-pH	6.16	1	6.16	2287.96	<0.0001
B-Temperature	1.28	1	1.28	477.31	<0.0001
C-NaCl Con.	0.018	1	0.018	6.77	0.0482
AB	0.026	1	0.026	9.70	0.0264
AC	1.464×10^{-3}	1	1.464×10^{-3}	0.54	0.4939
BC	6.021×10^{-4}	1	6.021×10^{-4}	0.22	0.6561
A^2	0.32	1	0.32	117.90	0.0001
B^2	5.198×10^{-3}	1	5.198×10^{-3}	1.93	0.2232
C^2	0.011	1	0.011	3.96	0.1033
Residual	0.013	5	2.690×10^{-3}		
Lack of fit	0.013	3	4.291×10^{-3}	14.78	0.0640
Pure error	5.804×10^{-4}	2	2.902×10^{-4}		
Corrected total	7.85	14			

Note: DF = degrees of freedom; Prob = Probability.

The *p*-value is used as a powerful tool to check the significance of each factor, which is the estimated probability of rejecting the null hypothesis (H_0) of a statistical hypothesis test. The null hypothesis refers to the hypothesis of no change or no effect. Normally, a *p*-value less than 0.05 (95% confidence level) suggests statistical significance. The lower the *p*-value, the more significant it is. It can be seen from Table 6.7, both factors A (pH) and B (temperature) are highly significant with excellent *p*-values (<0.0001), indicating strong evidence against a null hypothesis, and these are the main factors affecting precipitation in a salinity media. The effect of factor C (NaCl concentration) is also statistically significant, but it shows a borderline *p*-value. In addition, only the interaction between A (pH) and B (temperature) shows a significant effect on the studied response (log (nickel loss (%))). This result, to some extent, is in agreement with the observation in Chapter 4,

where the interaction between pH and temperature had a significant effect on log (nickel loss (%)) during iron precipitation from synthetic sulphate leach solutions containing just iron and nickel ions. The quadratic term for factor A also has a significant effect. Hence, an adequate quadratic model can be fitted for the log (nickel loss (%)) with only consideration of all significant terms (*p*-values <0.05), given by:

$$\begin{aligned} Y_{\log(\text{nickel loss}(\%))} = & -6.43 + 2.82 \times \text{pH} + 0.02 \times \text{Temperature} \\ & - 7.95 \times 10^{-4} \times \text{NaCl Concentration} \\ & - 2.69 \times 10^{-3} \times \text{pH} \times \text{Temperature} - 0.3 \times \text{pH}^2 \end{aligned}$$

Eq. 6.1

Where NaCl concentration is in g/L and temperature is degree Celsius.

In order to visualize the relationship between response and factors that describe the fitted quadratic model (Eq. 6.1), 3D response surface graphs and corresponding 2D contour plots were constructed, and are shown in Figure 6.1. These graphs show the combined effect of the interaction between pH and temperature on nickel loss for various NaCl concentrations. Notably, these graphs were similar in shape. The effect of NaCl concentration on nickel loss was not apparent. This is consistent with the conclusion obtained by analysis of variance (Table 6.7). Closer inspection of the response surface graphs shows that a slight reduction of nickel loss occurred with increasing NaCl concentration when precipitation was conducted at pH 4 and 85°C. For example, the maximum percentage of nickel loss was about 8.5% when the initial leach solution contained 30 g/L NaCl (Figure 6.1 (a)), however, this value dropped to about 7.3% during precipitation from solution containing 150 g/L NaCl (Figure 6.1 (c)).

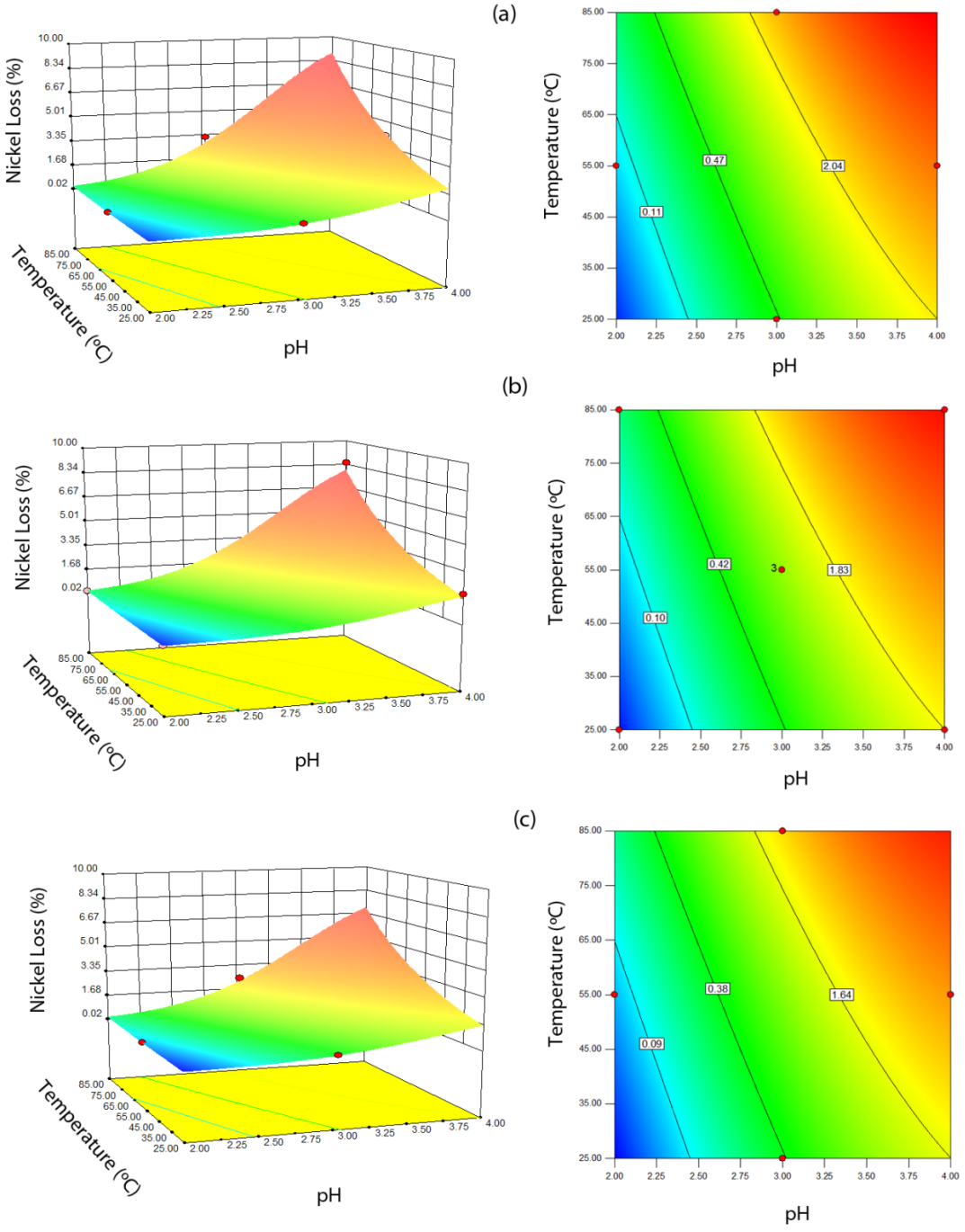

Figure 6.1: Response surface graphs (left) and corresponding contour plots (right) showing the combined effect of pH and temperature on nickel loss (%) ((a) NaCl Concentration=30 g/L; (b) NaCl Concentration=90 g/L; (c) NaCl Concentration=150 g/L). Red dots refer to experimental points.

6.3.3 XRD analysis of the precipitates

Several precipitation products obtained at pH 3, 85°C and various NaCl concentrations were examined by XRD analysis, and the results are given in Figure 6.2. It is noted that the XRD patterns of all these precipitates are dominated by schwertmannite and/or ferrihydrite with poor structural order. These patterns were similar to those obtained from synthetic solutions containing just iron and nickel ions (Figure 4.11 of Chapter 4). In addition, no apparent differences were observed in the XRD patterns for samples obtained from PLS containing various amounts of sodium chloride (Figure 6.2). The presence of large amounts of schwertmannite and/or ferrihydrite makes it difficult to identify other possible existing phases with higher structural order from XRD patterns. As indicated in Chapter 4, the presence of highly structural-ordered phases could only be identified after removing those phases with poor structure order, using selective Acidified Ammonium Oxalate (AAO) dissolution and Differential X-Ray Diffraction (DXRD). The application of these techniques to the characterization of iron-rich sulphate precipitates containing both poorly and highly structurally-ordered phases is discussed in Chapter 7.

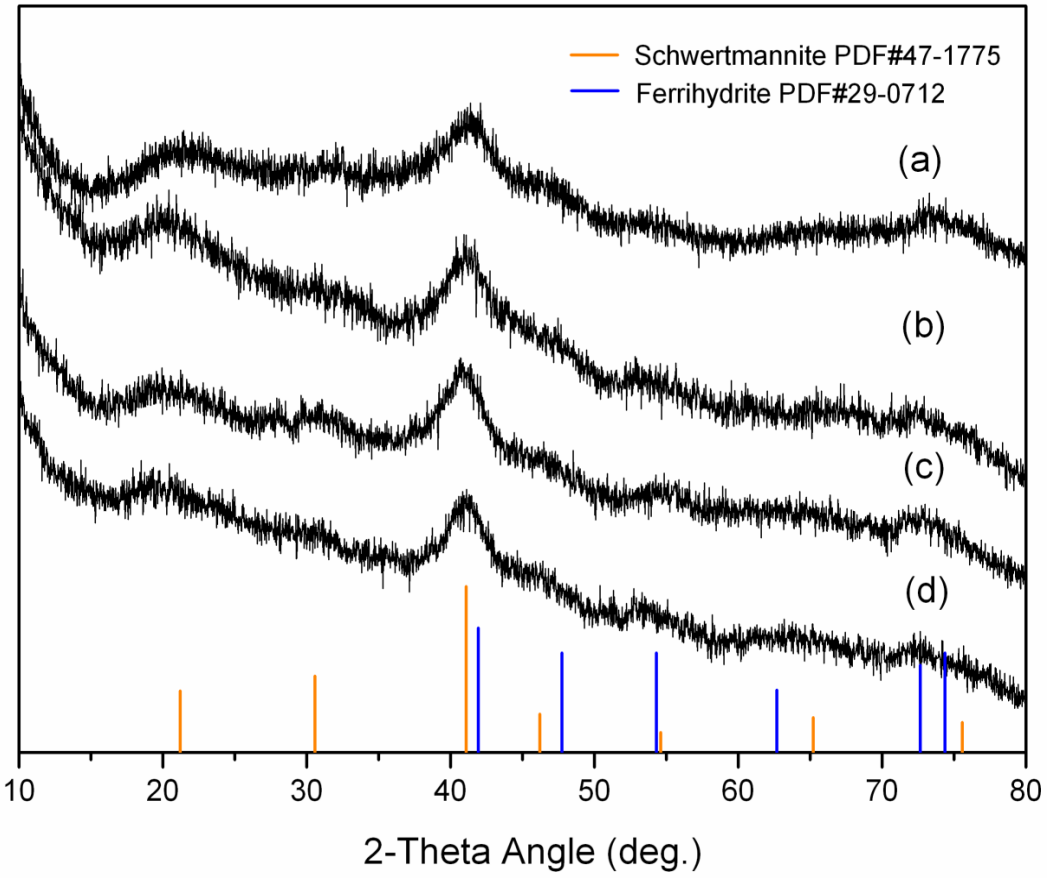

Figure 6.2: XRD patterns of precipitates formed from synthetic leach solutions for various experimental conditions ((a) sample FNAC-5, pH=3, 85 ºC and 0 g/L NaCl , (b) sample ES-7, pH=3, 85 ºC and 30 g/L NaCl, (c) sample ES-8, pH=3 and 85 ºC, 90 g/L NaCl, (d) sample ES-9, pH=3, 85 ºC and 150 g/L NaCl). The standard JCPDS patterns are shown as vertical lines at the bottom of the XRD patterns.

Jarosite-type compounds are known to have potential to form an impurity in hydrometallurgical processing. The formation of jarosite is favoured in the temperature range of 80 to 100 ºC and pH<2 from ferric sulphate solutions (Dutrizac and Jambor, 2000). Another important factor for the formation of jarosite is the presence of monovalent cations, such as Na^+, K^+, NH_4^+ and Ag^+. The review by Das *et al*. (1996) indicated that the monomer ferric species contains the basic chemical skeleton of jarosite. These exist in dynamic equilibrium with various basic sulphate species that are predominant in a ferric sulphate system. In the present study, those precipitation experiments conducted at elevated temperature in ferric sulphate media

in the presence of sodium chloride meet the requirements for the formation of jarosite-type compounds. Hence, it is worth performing XRD analysis on those samples. These results are shown in Figure 6.3.

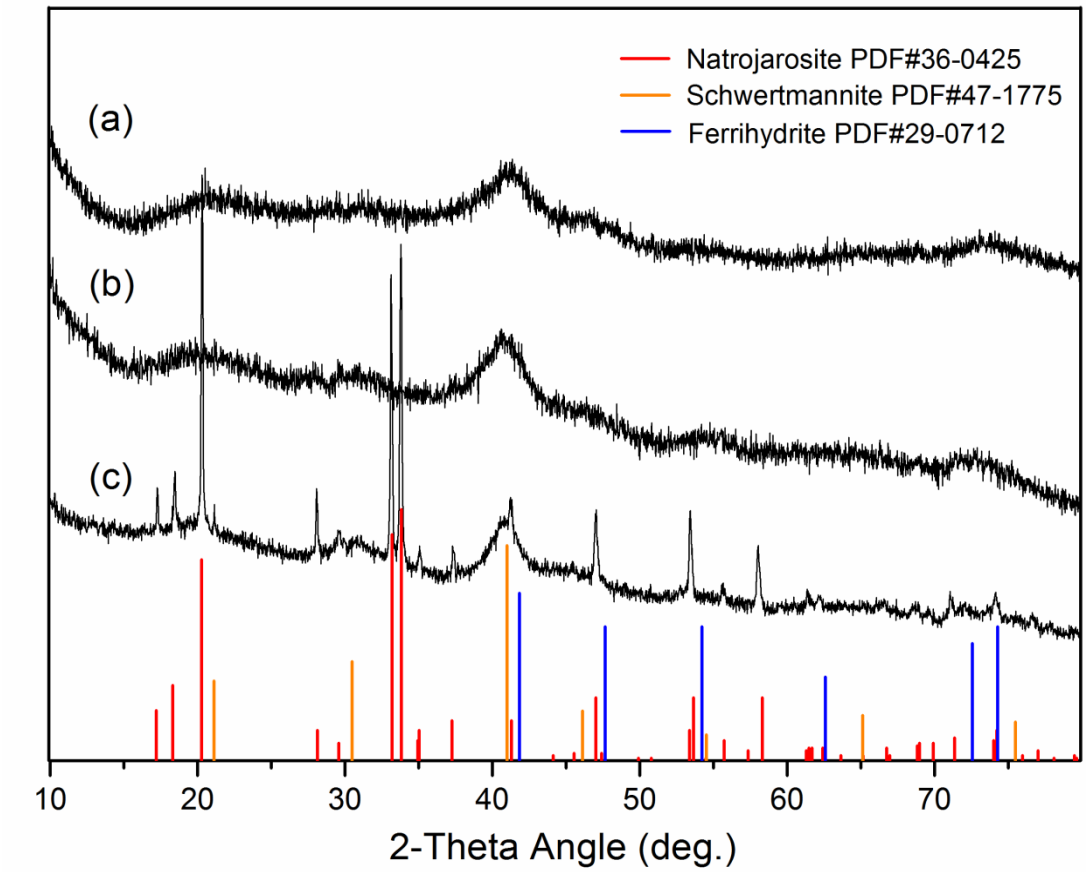

Figure 6.3: XRD patterns of precipitates formed from synthetic leach solutions ((a) sample ES-12, pH=4, 85 ºC and 90 g/L NaCl, (b) sample ES-8, pH=3, 85 ºC and 90 g/L NaCl, (c) sample ES-19, pH=2, 85 ºC and 90 g/L NaCl). The standard JCPDS patterns are shown as vertical lines at the bottom of XRD patterns.

The XRD patterns of all samples shown in Figure 6.3 were obtained at the same precipitation temperature (85 ºC), and from a synthetic leach solution with the same level of salinity (90 g/L NaCl), but the precipitation pH varied from 2 to 4. The poorly structurally-ordered schwertmannite and/or ferrihydrite are found to dominate the XRD patterns of the precipitates obtained at pH 3 and 4 (Figure 6.3 (a) and (b)). When the precipitation reaction was conducted at pH 2, sharp peaks are seen due to

natrojarosite ($NaFe_3(SO_4)_2(OH)_6$) (Figure 6.3 (c)). Notably, a small peak at *ca*. 21.5º 2θ (d-spacing 4.83Å) appeared to be gibbsite (d-spacing 4.85Å, PDF#33-18). However, the presence of gibbsite in sample ES-19 is questionable, as other distinctive XRD peaks for gibbsite were not identified. In addition, no distinct crystalline hematite (Fe_2O_3) was identified through XRD analysis, which was expected to be formed at atmospheric conditions in the presence of a high level of chloride. The reasons for non XRD-identifiable hematite in the present study are probably due to the lack of hematite seeding and/or preferable formation of jarosite-type compounds in a mixed sulphate and chloride aqueous media. Except for the sharp XRD peaks of natrojarosite, broad peaks belonging to poorly structural-ordered schwertmannite and/or ferrihydrite are also observed. This indicates that the sample obtained at pH 2 is a mixture containing both poorly and highly structurally-ordered phases.

6.4 CONCLUSION

The results of preliminary experiments reported within this chapter demonstrate that initial water salinity (as added sodium chloride) exerts little impact on the recovery of iron, aluminium and chromium when the precipitation is conducted at 25 ºC. However, when the precipitation reactions were carried out at 85 ºC, higher recoveries of iron, aluminium and chromium appear to be achieved and this was marginally higher for higher salinities. Further statistically-designed experiments confirmed that a reduction of nickel loss became notable only when the precipitation reaction was conducted at pH 4 and 85 ºC in a high salinity media. It was also demonstrated that pH and temperature, as well as their interaction are significant factors affecting the level of nickel loss. Increases in pH and temperature resulted in more loss of nickel to the solids, as also found in Chapter 4. The XRD analysis of solid precipitation products obtained from synthetic PLS with various salinities confirmed that schwertmannite and/or ferrihydrite were the dominant phase. Natrojarosite was identified when the precipitation reaction occurred at pH 2 and 85

^{o}C. The results of experiments performed within this chapter also suggest that the semi-batch precipitation method used in this thesis is able to process the PLS containing high water salinity with better nickel recovery and impurity removal efficiencies.

CHAPTER 7

CHARACTERIZATION OF IRON-RICH PRECIPITATES

7.1 INTRODUCTION

Fundamental XRD analysis in Chapters 4 and 6 showed iron-rich precipitates obtained were mainly poorly structurally-ordered schwertmannite and/or ferrihydrite. These iron-bearing oxyhydroxide and oxyhydroxysulphate minerals are thermodynamically unstable, and tend to transform over time to more stable iron oxides such as goethite and/or hematite (Cornell and Schwertmann, 2003). Moreover, the data on the thermodynamic properties and precise crystal structures of schwertmannite and ferrihydrite are still under debate (Jambor and Dutrizac, 1998; Majzlan *et al*., 2004). The disordered nature of these structures often leads to difficulty in mineralogical identification using routine X-Ray Diffraction (XRD) techniques. Furthermore, the mutual poor structural order of schwertmannite and ferrihydrite complicates their identification in a mixed assemblage. In particular, schwertmannite and ferrihydrite can become nearly undetectable by XRD when significant amounts of minerals with high structural order are also present in the mixed precipitate (Campbell and Schwertmann, 1984; Schwertmann *et al*., 1982). Conversely, trace to minor amounts of minerals with good structural order can be overlooked due to their XRD peaks being masked by minerals with poor structural order (Caraballo *et al*., 2009; Schulze, 1981). In such cases, a correct mineralogical analysis can only be made using a combination of several techniques that include selective dissolution using Acidified Ammonium Oxalate (AAO), Differential X-Ray Diffraction (DXRD), Scanning Electron Microscopy (SEM) and, Fourier Transform Infra-Red (FTIR) spectroscopy.

Metallic cations that include aluminium, chromium and nickel have been found to influence both the formation and transformation of iron oxides. These either change

the composition and properties of the end products or slow the transformation rates of their intermediates (Cornell and Schwertmann, 2003). Much research has been directed toward understanding the association of aluminium, chromium and nickel with goethite and ferrihydrite: see, for example, Al, Cr and Ni-goethite (Schwertmann *et al.*, 1989; Singh and Gilkes, 1992; Singh *et al.*, 2002) and Al, Cr and Ni-ferrihydrite (Giovanoli and Cornell, 1992; Lewis and Schwertmann, 1979; Schwertmann, 1991). These studies have established the mechanism of cation substitution for iron in goethite. However so far, no direct evidence of structural incorporation has been provided for the co-precipitation of ferrihydrite with various cations, probably due to the small particle size and poor crystallinity of ferrihydrite which makes the distinction between surface adsorption and structural incorporation difficult to determine (Cornell and Schwertmann, 2003). Furthermore, very few studies have examined the mixtures of iron oxides, oxyhydroxide and oxyhydroxysulphate with other metallic cations that commonly occur in the hydrometallurgical processing of AL liquors. Acero *et al.* (2006) studied the behaviour of trace metallic cations during schwertmannite precipitation and subsequent transformation into goethite and jarosite. However, this study as well as others (Caraballo *et al.*, 2009; Dold, 2003b) all focused on natural precipitates from acidic mine water and under conditions that differ from hydrometallurgical precipitation processes.

Chapter 7 provides a detailed mineralogical characterization of iron-rich precipitates. The aims are to apply selective AAO dissolution and characterization techniques that include DXRD, SEM and FTIR spectroscopy to obtain an accurate and detailed mineralogical identification of complicated iron-rich precipitates from synthetic atmospheric nickel laterite leach solutions, which contain both poorly and highly structural-ordered phases formed in the presence of the foreign metallic cations. Emphasis is directed toward the effects of the foreign metallic cations on crystallization, dissolution behavior and mineralogical properties of the precipitates.

7.2 EXPERIMENTAL AND ANALYTICAL METHODS

All precipitation experiments were conducted using a semi-batch procedure, as detailed in Chapter 4. For each test a volume of 500 mL of synthetic PLS containing 30 g/L Fe^{3+} [as $Fe_2(SO_4)_3 \cdot xH_2O$], 0 to 5 g/L Ni^{2+} [as $NiSO_4 \cdot 6H_2O$], 0 to 6.5 g/L Al^{3+} [as $Al_2(SO_4)_3 \cdot 18H_2O$], and 0 to 2 g/L Cr^{3+} [as $Cr_2(SO_4)_3 \cdot xH_2O$] was pumped into a baffled reaction vessel containing a pre-determined amount of de-ionized water over a period of 2.5 h. A $CaCO_3$ (25% w/w) suspension in de-ionized water was simultaneously pumped into the reaction vessel to maintain the pH at 4. The temperature was controlled using an oil bath and the precipitation reactions conducted at both 25 and 85 ºC. At the completion of the reaction, the resulting slurry was vacuum filtered through a 0.45 µm Gelman Supor® membrane. The metal concentrations in the filtrate were analysed by ICP-OES, and the filter cake was carefully washed with large amounts of hot de-ionized water until the conductivity of the filtrate was constant (<100 µS) and then dried overnight at 60 ºC. The chemical composition of the dried solid products was determined by ICP-OES after aqua regia digestion.

To obtain standards for comparison, schwertmannite was synthesized by the method of Loan *et al*. (2004) and 6-line ferrihydrite according to the method of Schwertmann and Cornell (2000). Briefly, schwertmannite was prepared by placing 1L of 0.7 g/L ferric solution (as $Fe_2(SO_4)_3 \cdot xH_2O$) in a Nalgene® bottle and then agitated using a mechanical bottle-roller water bath at 85 ºC for one hour. The solution was filtered through a 0.45 µm Gelman Supor® membrane, washed with Milli-Q water and dried overnight at 60 ºC. The 6-line ferrihydrite was prepared by adding 20 g of $Fe(NO_3)_3 \cdot 9H_2O$ into preheated 75 ºC Milli-Q water for 10 minutes, quenching in an ice bath and transferring the product to dialysis tubing for at least three weeks to remove the NO_3^- ions. The colloidal 6-line ferrihydrite formed was collected by freeze drying.

Selective dissolution experiments were conducted by dissolving the dried solid samples in 0.2 M ammonium oxalate solution acidified to pH 3.0 with 0.2 M oxalic acid at room temperature in the absence of visible light, as described by Schwertmann *et al*. (1982). The dissolution kinetics was studied by shaking approximately 2 g of sample in 1 L of acidified ammonium oxalate solution and extracting 10 mL samples at specific time intervals. The samples were immediately filtered and the ion concentration in the filtrate analysed by ICP-OES.

Dried solid samples were analysed by X-Ray Diffraction (XRD) using a Philips X'pert diffractometer with CoKα radiation operated at 45 kV and 40 mA with a step scan of 0.02º. Fourier Transform Infra-Red (FTIR) spectroscopy measurements were made with a Bruker infrared spectrometer from 4000-400 cm^{-1} at room temperature using the KBr pellet technique. Some samples were carbon-coated and examined at high magnification with a Zeiss Neon 40EsB Focused Ion Beam-Scanning Electron Microscope (FIB-SEM).

7.3 RESULTS AND DISCUSSION

7.3.1 Chemical compositions and mineralogical properties of iron-rich precipitates

The first two experiments shown in Table 7.1, labelled as F-1 and F-2, refer to the single-metallic samples obtained from PLS containing only ferric iron, which serve as "baselines" for other experiments. FN-2 and FN-4 are the bi-metallic samples precipitated from PLS containing iron and nickel, while FNAC-2 and FNAC-6 represent the multi-metallic samples obtained from PLS containing iron, aluminium, chromium and nickel. Notably, from Table 7.2, increasing temperature resulted in more aluminium, chromium, and nickel but less sulphur in the iron-rich solid precipitates.

Table 7.1: Summary of the experimental conditions and chemical composition of synthetic leach solution for preparation of iron-rich precipitates.

Sample	Precipitation Conditions		Initial (g/L)				Final (g/L)			
	pH	T (ºC)	Fe	Ni	Al	Cr	Fe	Ni	Al	Cr
F-1	4	25	29.5	N/A	N/A	N/A	0.02	N/A	N/A	N/A
F-2	4	85	29.5	N/A	N/A	N/A	0.01	N/A	N/A	N/A
FN-2[‡]	4	25	29.9	4.9	N/A	N/A	0.01	2.3	N/A	N/A
FN-4[‡]	4	85	29.9	4.9	N/A	N/A	0.01	2.2	N/A	N/A
FNAC-2[§]	4	25	30.2	5.1	6.6	2.0	0.02	2.2	0.5	0.02
FNAC-6	4	85	31.5	5.0	6.5	2.1	0.01	2.0	0.01	0.01

Note: [‡] Data were sourced from Table 5.1 of Chapter 5; [§]Data were sourced from Table 5.8 of Chapter 5; N/A=Not Applicable.

Table 7.2: The chemical composition of the iron-rich precipitates [*].

Sample	Elemental composition in the solid precipitation product (weight %)					
	Fe	Ni	Al	Cr	S	Ca
F-1	49.9	N/A	N/A	N/A	4.9	<0.01
F-2	52.4	N/A	N/A	N/A	2.9	<0.01
FN-2	50.8	0.03	N/A	N/A	5.0	0.02
FN-4	51.9	0.45	N/A	N/A	3.1	<0.01
FNAC-2	33.6	0.06	5.7	2.2	6.0	0.03
FNAC-6	34.1	0.54	7.1	2.3	4.8	<0.01

Note: [*] N/A=Not Applicable.

Figure 7.1 shows the XRD patterns of the synthetic 6-line ferrihydrite, synthetic schwertmannite, single-, bi- and multi-metallic samples. Schwertmannite and ferrihydrite have poor structural order, and usually precipitate as a mixture from acid sulphate solutions. Furthermore, ferrihydrite can adsorb sufficient sulphate to approximate the composition of schwertmannite, making it difficult to distinguish

between ferrihydrite and schwertmannite (Bigham and Nordstrom, 2000). The XRD patterns of both schwertmannite and 6-line ferrihydrite exhibit a strong peak at around 41° 2θ and two weaker peaks between 70° and 80° 2θ, although the intensities are reversed for these two peaks. Schwertmannite displays two better defined peaks at around 21° and 31° 2θ, while 6-line ferrihydrite shows a characteristically sharper peak at around 47° 2θ. Despite the differences, it is difficult to unambiguously identify these phases in a mixed assemblage of hydrated iron oxides, particularly when admixed with other minerals.

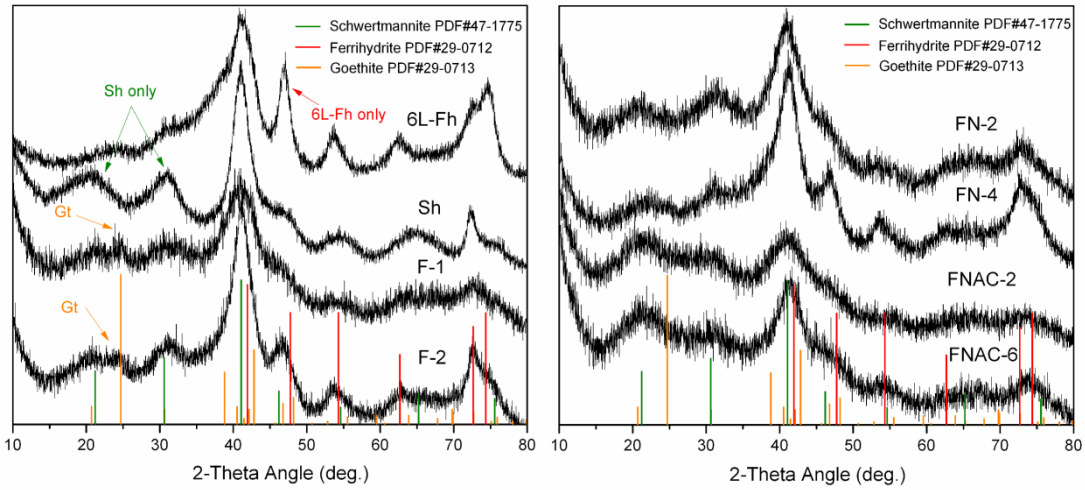

Figure 7.1: X-Ray Diffraction (XRD) patterns of the synthetic 6-line ferrihydrite (6L-Fh), schwertmannite (Sh), single-metallic samples (F-1 and F-2), bi-metallic samples (FN-2 and FN-4), and multi-metallic samples (FNAC-2 and FNAC-6). The standard JCPDS patterns are given as vertical lines at the bottom of XRD patterns. Abbreviation: Gt=goethite.

The XRD patterns of single-metallic sample F-1 and bi-metallic sample FN-2 appear to be dominated by schwertmannite, whereas that of sample F-2 and FN-4 shows characteristics of schwertmannite admixed with 6-line ferrihydrite. Only schwertmannite can be identified with certainty in the XRD patterns of the multi-metallic samples FNAC-2 and FNAC-6. Interestingly, weak peaks ascribed to goethite at *ca.* 25° 2θ can be identified in the XRD patterns of the single-metallic

samples F-1 and F-2, but were not discernible in the presence of foreign metallic cations. This suggests that the formation of goethite is influenced by the presence of foreign metallic cations. The experimental work by Giovanoli and Cornell (1992) has shown that divalent transition metal ions (*i.e.* Mn^{2+}, Co^{2+}, Ni^{2+}, Cu^{2+} and Zn^{2+}) have significant effects on the kinetics and products of crystallization derived from ferrihydrite. All of these ions, except for Mn^{2+}, can retard the transformation of ferrihydrite by stabilizing it against both dissolution, which leads to goethite formation, and internal rearrangement, which produces hematite. Aluminium shows a weak retarding ability on the transformation of ferrihydrite to phases with a highly ordered structure, but the extent of retardation depends on the Al/Fe ratio and the pH of solution; a higher Al/Fe ratio and lower pH enhance the retarding ability (Cornell and Schindler, 1987). The experimental work by Schwertmann *et al*. (1989) showed that ageing $Cr(NO_3)_3$-$Fe(NO_3)_3$ solution over sufficiently long periods (above 100 days), although under alkaline conditions, resulted in the near complete conversion of ferrihydrite to goethite. In the present study, comparison of the XRD patterns of single-, bi- and multi-metallic samples confirmed that the presence of nickel, aluminium and chromium can retard the transformations of schwertmannite and/or ferrihydrite to goethite, but aluminium and chromium further retard the formation of 6-line ferrihydrite. A more detailed discussion on the conversion between ferrihydrite, schwertmannite and goethite is given in subsequent sections.

7.3.2 Selective AAO dissolution of iron-rich precipitates

7.3.2.1 Dissolution kinetics

Selective dissolution using AAO can be used to discriminate poorly and highly structurally-ordered minerals in a mixed assemblage (Schwertmann *et al*., 1982). The dissolution rate is an important indicator, as ferrihydrite and schwertmannite readily dissolve in AAO solution at pH 3.0 and 25 °C in the absence of visible light but goethite does not (Cornell and Schwertmann, 2003). In the present study, the dissolution behaviour of iron-rich precipitates with foreign metallic cations present,

the bi-metallic and the multi-metallic precipitates, were examined, with the results presented in Figure 7.2. There were large differences in the shape of the curves for the bi-metallic and multi-metallic samples. The dissolution curves were sigmoidal in shape for bi-metallic samples, whereas the curves of multi-metallic samples were near linear. Precipitation temperature had a significant effect on the dissolution kinetics of the precipitates. All precipitates obtained at 25 ºC dissolved much slower compared to those precipitated at 85 ºC.

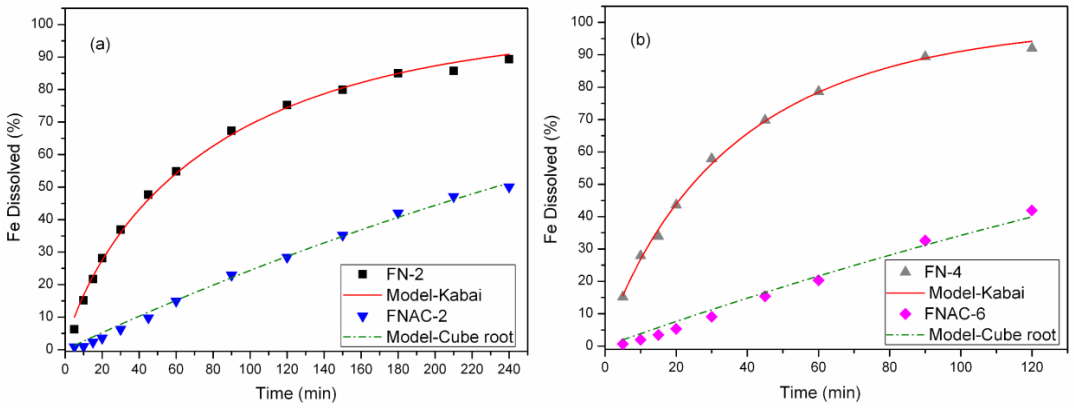

Figure 7.2: Dissolution curves of bi-metallic and multi-metallic precipitates obtained at different temperatures: (a) 25 ºC and (b) 85 ºC. Lines represent the modelled curve fits.

There have been many dissolution kinetic studies focusing on various natural and synthetic, pure and metal-substituted goethites (Landers and Gilkes, 2007; Lim-Nunez and Gilkes, 1987; Perrier *et al.*, 2006). These studies, which were normally conducted in strong mineral acid (*e.g.* HCl and H_2SO_4), have shown that metal substitution plays an important role in determining dissolution rate. For instance, Al^{3+}, which is the most common isomorphic substituent for Fe^{3+}, can substantially decrease the dissolution rate of goethite in various concentrations of HCl (Schwertmann, 1991). Chromium (as Cr^{3+}) stabilizes goethite against dissolution in 1 M HCl to a much greater extent than aluminium, even at a small level of incorporation, whereas nickel appears to have little effect on dissolution rate (Lim-

Nunez and Gilkes, 1987). The recent work by Kaur *et al*. (2010) further indicated that chromium strongly retarded the dissolution of both single- and multi-metal substituted goethites in 1M HCl. Since chloride is considered to activate the dissolution sites by forming surface Fe−Cl complexes, hydrochloric acid is widely used in controlled dissolution studies (Cornell *et al*., 1976). Although sulphate ions do not form such surface complexes, the experimental work by Landers *et al*. (2009) showed a similar effect for aluminium and chromium in reducing the dissolution rate of nickeliferous goethite in 2 M H_2SO_4. Compared to goethite, there is far less published data describing the dissolution behaviour of metal-substituted ferrihydrite and schwertmannite, particularly when both phases are present and admixed with minerals having highly ordered structures.

Normally, iron oxide dissolution proceeds by three pathways: protonation, reduction and complexation (Schwertmann, 1991). The dissolution of iron oxide by AAO is due to a cooperative mechanism involving the protons and oxalate ligand, which includes steps of oxalate adsorption, iron detachment and proton adsorption/surface restoration (Stumm *et al*., 1985). The study on the dissolution of Al-goethite by Cornell and Schindler (1987) showed that highly substituted goethite (15.9 mole% Al) dissolved much more slowly than unsubstituted goethite in acidified oxalate solution. Incorporation of metal ions within the structure of iron oxides can affect the dissolution behaviour by altering bond strength. The ionic radii of Al^{3+} (0.0535 nm) and Cr^{3+} (0.0615 nm) are smaller than for Fe^{3+} (0.0645 nm), which results in shorter bond lengths and larger Me−O bond energies, *i.e.* Al−O (29.3 kJ/mol) and Cr−O (24.5 kJ/mol) compared with Fe−O (23.7 kJ/mol) (Wells *et al*., 2006). Given the evidence from these previous studies, it can be postulated that aluminium and chromium will play similar roles for highly disordered iron-bearing oxyhydroxide and oxyhydroxysulphate. Aluminium and chromium appear to strongly stabilize the multi-metallic precipitates against dissolution by AAO solution.

Depending on the type or shape of the iron dissolution curves, the data are normally modelled by various mathematical equations, of which the Kabai equation and cube-root law are the most common ones and have been used in various studies (Landers and Gilkes, 2007; Singh and Gilkes, 1992; Wells *et al*., 2001). In this study, the sigmoidal dissolution-time profiles of the bi-metallic samples were best modelled using the Kabai equation (Kabai, 1973):

$$\ln\ln\frac{C_0}{C_0-C}=\ln K+\alpha\ln t=\alpha\ln k+\alpha\ln t \qquad \text{Eq. 6.1}$$

where C_0 is the initial amount of solid, C is the amount of solid dissolved at time t, k is a rate constant ($K=k^{\alpha}$) and α is a Kabai constant that relates to the characteristics of the solid phases. The iron dissolution rate constant (k_{Fe}) for FN-2 and FN-4 was 12.3×10^{-3} min^{-1} and 27.0×10^{-3} min^{-1}, respectively. The correlation coefficients (R^2) were both above 0.99, indicating good fit to data. The Kabai constant (α) for FN-2 and FN-4 was 0.81 and 0.89, respectively. Landers and Gilkes (2007) indicated that when $\alpha<1$, the rate of dissolution is determined by the rate of chemical reaction at the crystal surface, whereas the dissolution reaction is diffusion controlled when $\alpha>1$. For the multi-metallic samples (FNAC-2 and FNAC-6), the dissolution data were better described by the cube-root law (Hixson and Crowell, 1931):

$$1-(1-\omega)^{\frac{1}{3}}=kt \qquad \text{Eq. 6.2}$$

where ω is the fraction of the solid dissolved at time t and k is a rate constant. The rate constants for iron dissolution (k_{Fe}) were 0.89×10^{-3} min^{-1} for FNAC-2 and 1.30×10^{3} min^{-1} for FNAC-6, respectively.

7.3.2.2 Dissolution process revealed by SEM images

SEM images of the bi- and multi-metallic samples at different dissolution times are shown in Figure 7.3. Both FN-2 and FNAC-2 showed aggregates of spherical crystallites with diameters of about 0.5 µm (Figure 7.3 (a) and (g)). The appearance

of these particles is similar to that of schwertmannite, as reported by Schwertmann and Carlson (2005). After 120 and 240 minutes dissolution in oxalate solution, the "larger" spherical aggregates in sample FN-2 had dissolved to reveal "smaller" aggregates (Figure 7.3. (b) and (c)). In comparison, partially dissolved "larger" spherical features can still be observed in the residues for sample FNAC-2 (Figure 7.3 (h) and (i)). In the case of FN-4 and FNAC-6 (Figure 7.3 (d) and (j)), the nanoscale particles produced were highly aggregated, having similar structural appearance to that of ferrihydrite particles (Dold, 2003a). There were no significant differences in the appearance of residues from samples FN-4 and FNAC-6 after 60 and 120 minutes AAO dissolution.

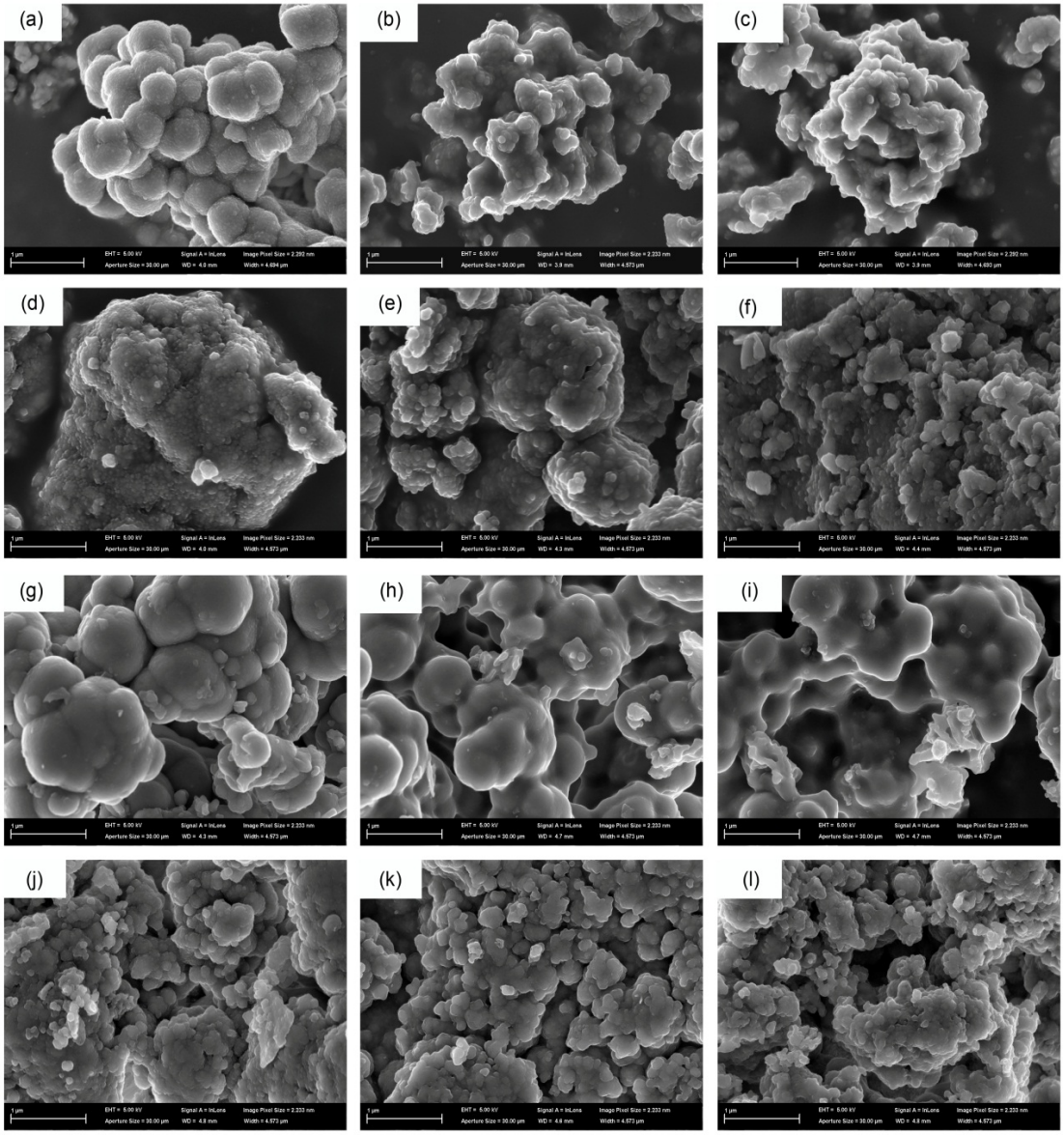

Figure 7.3: SEM images of bi-metallic and multi-metallic precipitates before and after AAO dissolution: sample FN-2 after 0 min (a), 120 min (b) and 240 min (c) AAO dissolution; sample FN-4 after 0 min (d), 60 min (e) and 120 min (f) AAO dissolution; sample FNAC-2 after 0 min (g), 120 min (h) and 240 min (i) AAO dissolution; sample FNAC-6 after 0 min (j), 60 min (k) and 120 min (l) AAO dissolution. The scale bar in each image corresponds to a distance of 1µm.

7.3.2.3 Congruency of metal(s) dissolution with iron

An indirect way to investigate the association between other metals and iron is from

plots of the % metal released versus % Fe dissolved during dissolution (Singh and Gilkes, 1992). If the metal and iron dissolve at a similar rate, the metal is uniformly distributed throughout the iron oxide matrix. By contrast, if the metal and iron dissolve incongruently, the other metal is either more concentrated at the iron oxide particle periphery or in the core. Graphs showing the relationships between the metals and iron dissolution for both bi- and multi-metallic samples are presented in Figure 7.4. Due to the presence of a very small amount of nickel in the sample FN-2 (0.03% Ni, Table 7.2), the soluble nickel obtained during the initial dissolution period could not be detected by ICP-OES (below the detection limit of 0.02 ppm) (Figure 7.4 (a)). To facilitate the calculation of experimental error, the dissolution of sample FN-2 was performed in triplicate, with error bars shown corresponding to standard deviations. The first point on the graph (Figure 7.4 (a)) suggests that the initial dissolution of iron was more rapid, and that by time the nickel in solution was concentrated enough to detect, it was dissolving faster than iron with trending back toward congruent behaviour. In the case of sample FN-4 (Figure 7.4 (b)), nickel initially dissolved faster than iron, but then slows so that the data approached the congruency. For the multi-metallic samples (Figure 7.4 (c) and (d)), aluminium, chromium and nickel dissolved approximately congruently with iron, indicating these metals were in general uniformly distributed within the iron oxide matrix.

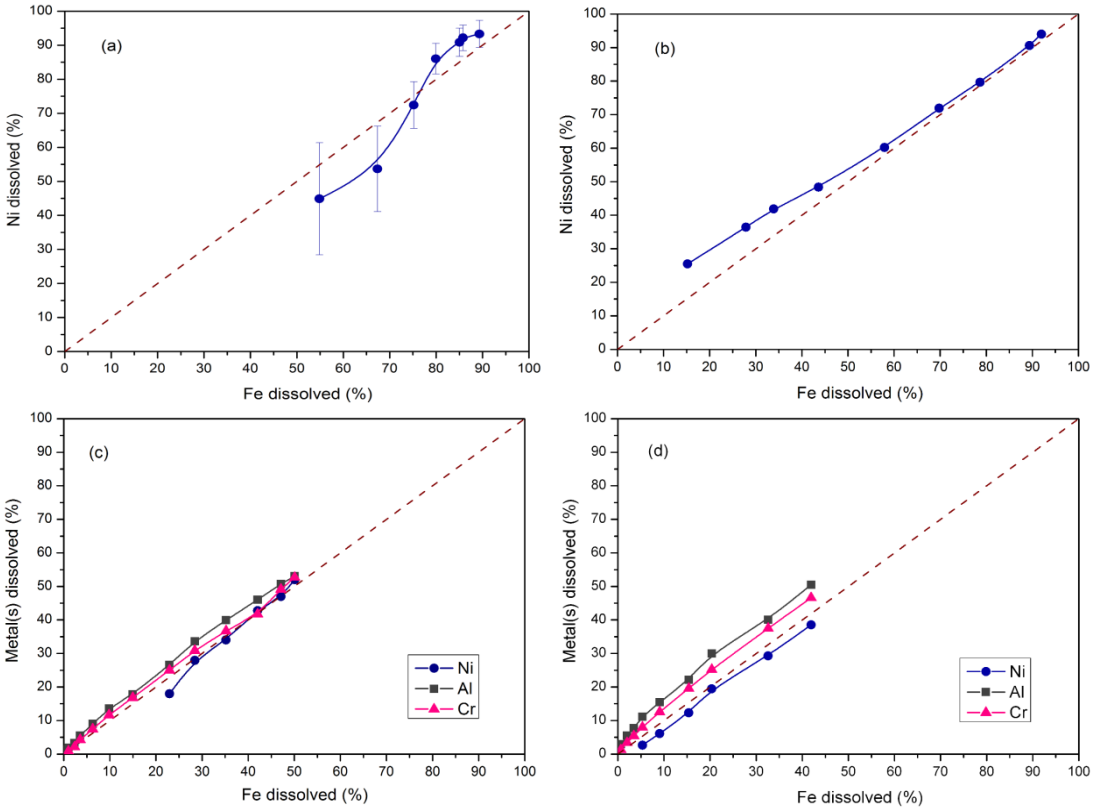

Figure 7.4: Dissolution of iron and metal(s): (a) and (b) for bi-metallic samples FN-2 and FN-4, respectively; (c) and (d) for multi-metallic samples FNAC-2 and FNAC-6, respectively. The unit slope, represented as dash line, indicates congruent dissolution of both iron and metal(s).

7.3.2.4 Changes in iron to sulphur ratios

A summary of the changes in the Fe/S mole ratio for iron precipitates, obtained at different AAO dissolution stages, is presented in Figure 7.5. The Fe/S mole ratio values of all samples increased rapidly during the initial dissolution period, and then reached plateaus after about 60 min (Figure 7.5). Specifically, the Fe/S mole ratio increased to approximately 8 within the first 20 min of dissolution for bi-metallic samples FN-2 and FN-4, which is similar to the typical ratio in schwertmannite (Bigham *et al*., 1990). Sulphate is known to occur both within the bulk structure and on the surface of schwertmannite, and the amount of surface adsorbed sulphate is reported from 30 to 35% (Jönsson *et al*., 2005) up to 60% (Webster *et al*., 1998). The

dissolution study of schwertmannite by Bigham *et al*. (1990) indicated that the surface sulphate was easily liberated at the initial dissolution stage. Thus, the fast release of sulphate during the initial dissolution stage (lower Fe/S mole ratios) was assumed to be partly due to the removal of sulphate from surface sites. It is noteworthy that it may be inaccurate to ascribe all the initially released sulphate to surface adsorbed sulphate associated with schwertmannite, as a considerable amount of sulphate can also adsorb onto goethite and ferrihydrite forming surface complexes (Parfitt and Smart, 1978). The initial fast release of sulphate was also observed for samples FNAC-2 and FNAC-6, but the subsequent plateau remained nearly constant at a Fe/S mole ratio between 4 and 5.

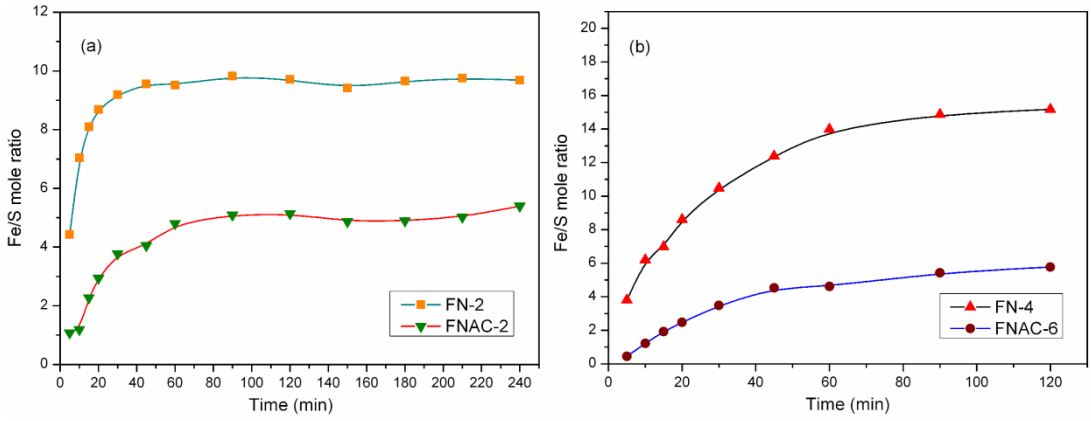

Figure 7.5: Changes in Fe/S mole ratios of AAO solution as a function of dissolution time for bi-metallic and multi-metallic samples obtained at different temperatures: (a) 25 ºC and (b) 85 ºC.

7.3.3 Mineralogical changes due to selective AAO dissolution

7.3.3.1 XRD and DXRD analysis

After removing some of the oxalate-extractable phases, the XRD patterns of the treated bi-metallic samples then show the presence of goethite (Figure 7.6 (a) and (b)). The goethite diffraction peaks became more apparent with extended extraction time. This confirms that the goethite peaks were hidden by the presence of large amounts of poorly structurally-ordered phases in the initial untreated sample (Figure

7.1). For the slow dissolving multi-metallic precipitates, XRD patterns were only collected for the samples at the completion of 120 min AAO dissolution (Figure 7.6 (c) and (d)). Here only poorly ordered schwertmannite can be identified in these patterns.

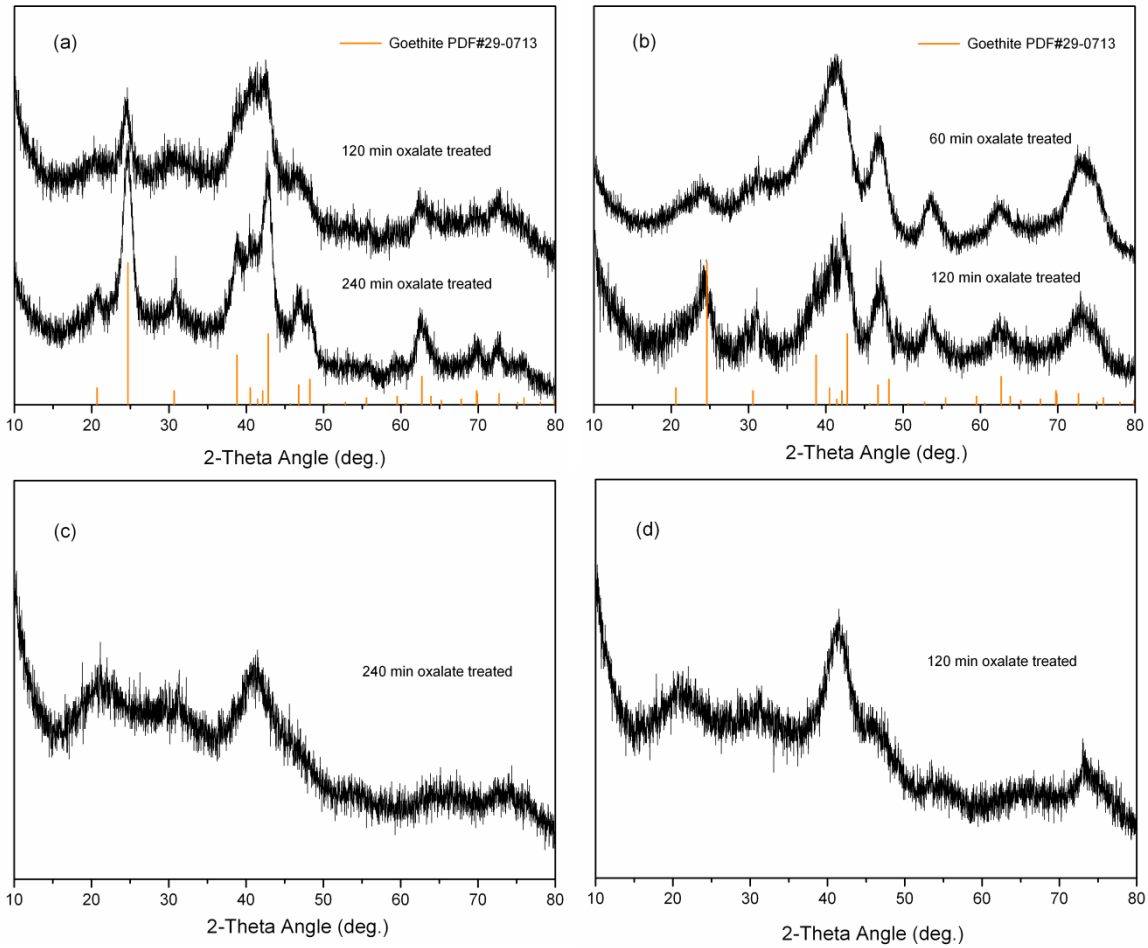

Figure 7.6: XRD patterns of the precipitates after AAO dissolution: (a) and (b) for bi-metallic sample FN-2 and FN-4, respectively; (c) and (d) for multi-metallic sample FNAC-2 and FNAC-6, respectively.

Differential X-ray diffraction (DXRD) facilitates the identification of dissolved ferrihydrite and schwertmannite by selective AAO dissolution (Schwertmann *et al.*, 1982). This technique involves the subtraction of an oxalate treated sample diffractogram from the diffractogram of the same sample prior to treatment. The XRD patterns obtained before and after AAO dissolution have different overall

intensities due to the changes in the mass attenuation coefficient resulting from the removal of the oxalate-soluble minerals (Schulze, 1981). To subtract the patterns correctly, an intensity correction factor (*k*-factor) is normally used (Schulze, 1981). The DXRD performed for both bi- and multi-metallic samples after different dissolution stages shows that schwertmannite was the most readily oxalate-extractable phase, which dissolved preferentially to 6-line ferrihydrite (Figure 7.7). This is in agreement with the observations of Dold (2003a), who studied the dissolution kinetics of natural and synthetic schwertmannite and ferrihydrite in oxalate solution and found that greater than 94% of the schwertmannite dissolved in 60 min, whereas only 16% of the synthetic 6-line ferrihydrite dissolved in the same period. Cornell and Schwertmann (2003) suggested AAO can dissolve ferrihydrite completely at room temperature within 2-4 h. The intensity of the negative peak at *ca.* 25° 2θ in the DXRD patterns of sample FN-2 (Figure 7.7 (a)) increased with increasing dissolution time. This suggests that most of the schwertmannite was removed, leaving the residual goethite essentially undissolved. The change in the degree of preferred orientation in particular for the goethite (110) diffraction peak after AAO treatment may also result in the negative peaks obtained from the pattern subtraction (Schulze, 1986). Conversely, in acidic sulphate solution, the schwertmannite transformation to goethite is slow, normally requiring hundreds of days at room temperature (Acero *et al.*, 2006). Thus, within the time frame of the present study, goethite observed from the AAO treated samples was inferred to be present in the initial precipitates.

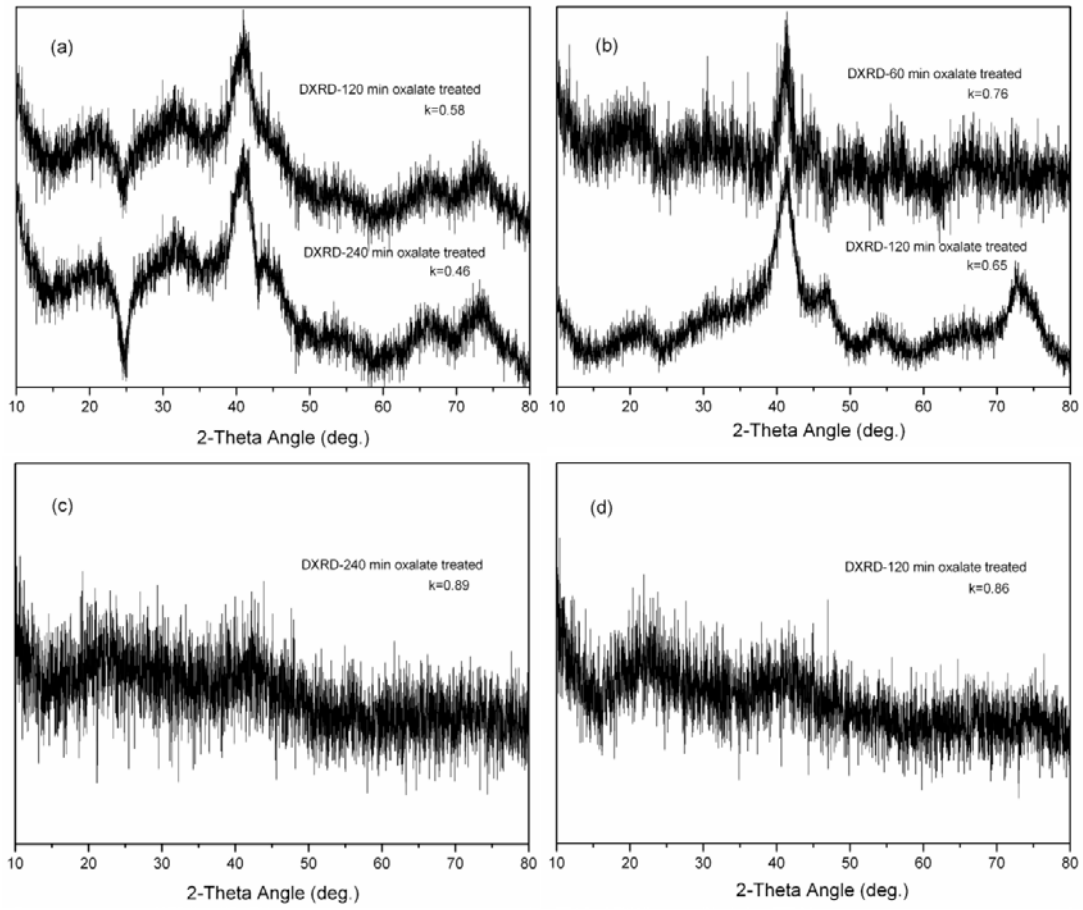

Figure 7.7: DXRD patterns obtained by subtracting oxalate treated pattern from untreated pattern: (a) and (b) for bi-metallic samples FN-2 and FN-4, respectively; (c) and (d) for multi-metallic samples FNAC-2 and FNAC-6, respectively.

The iron precipitation process used in this work is similar to the E.Z. Goethite Process which was originally developed by Allen *et al.* (1970) and subsequently modified by Roche (2009). Many researchers indicate that the residues from the E.Z. Goethite Process contained poorly defined basic iron sulphates and iron oxyhydroxide rather than pure goethite precipitates (Claassen *et al*., 2002; Davey and Scott, 1975; Gordon and Pickering, 1975). This observation was, to some extent, analogous to the findings of the present study. The iron-rich precipitates from the so-called E.Z. Goethite Process actually consist of significant amounts of schwertmannite and/or ferrihydrite, and minor amounts of goethite with poor crystallinity. In aqueous solutions, the phase transformations for hydrated iron oxides normally proceed via dissolution-recrystallization mechanism, in which the less

stable phases such as ferrihydrite and schwertmannite form first (Blesa and Matijević, 1989). The mechanism of goethite formation from the dissolution of ferrihydrite is well established in alkaline media due to the presence of the preferred growth unit $Fe(OH)_4^-$ (Cornell *et al.*, 1989). However, the goethite growth mechanism in acidic sulphate media is more complicated, as the $Fe(OH)_4^-$ growth unit is not usually present in acidic solutions, and the formation of the $FeSO_4^+$ complex strongly suppresses the polymerization of the hydroxyl complex and the precipitation of goethite (Cornell and Schwertmann, 2003). Loan (2004) suggested that goethite could be formed from ferrihydrite by structural re-arrangement in acid media, in which ferrihydrite acts as a growth unit that can adsorb and orientate on the goethite surface.

In the presence of sulphate, schwertmannite is the dominant phase, its formation being thermodynamically favoured over ferrihydrite in the pH range between 2 and 8 (Majzlan *et al.*, 2004). It has been shown that when schwertmannite is equilibrated with water at room temperature, it can transform to goethite over a long time period, *e.g.* 543 days at pH=3.9 (Bigham *et al.*, 1996), and 100 days at pH=4-7.2 (Schwertmann and Carlson, 2005). The experimental work by Schroth and Parnell (2005) has shown that goethite can be formed from schwertmannite via a dissolution/re-precipitation mechanism which is similar to that for the ferrihydrite transformation to goethite. In any event, there seems to be specific conditions for the formation of precipitates such as ferrihydrite, schwertmannite and goethite. These compounds seem to form from unique, and as yet unknown, polymerization reactions of ferric iron species which change markedly with precipitation conditions.

7.3.3.2 FTIR analysis

FTIR spectroscopy is a sensitive tool to detect the changes in the molecular symmetry of sulphate in schwertmannite-bearing samples (Boily *et al.*, 2010). The FTIR spectra for each AAO untreated bi- and multi-metallic sample presented in Figure 7.8 show similar absorption bands to schwertmannite, *i.e.* v_1–SO_4 at 976

cm^{-1}, splitting of the v_3−SO_4 band between 1200 and 1000 cm^{-1}, v_4−SO_4 at 608 cm^{-1}, Fe−O stretching vibration at 483 cm^{-1}, and OH−stretching and bending vibrations at 3300 and 1634 cm^{-1}, respectively (Bigham *et al.*, 1990). The assignment for the band at about 700 cm^{-1} is problematic and still under debate. Lazaroff (1983) assigned this band to the rotational mode of hydrated water in the iron-bearing sulphate precipitates. The recent FTIR spectra study of schwertmannite by Boily *et al.* (2010) has shown that the band at around 700 cm^{-1} resulted from the deformation modes of OH groups forming hydrogen bonds with sulphate ions. This is not dissimilar to the hydrogen bonds with chloride ions in the structure of akaganéite, as proposed by Weckler and Lutz (1998).

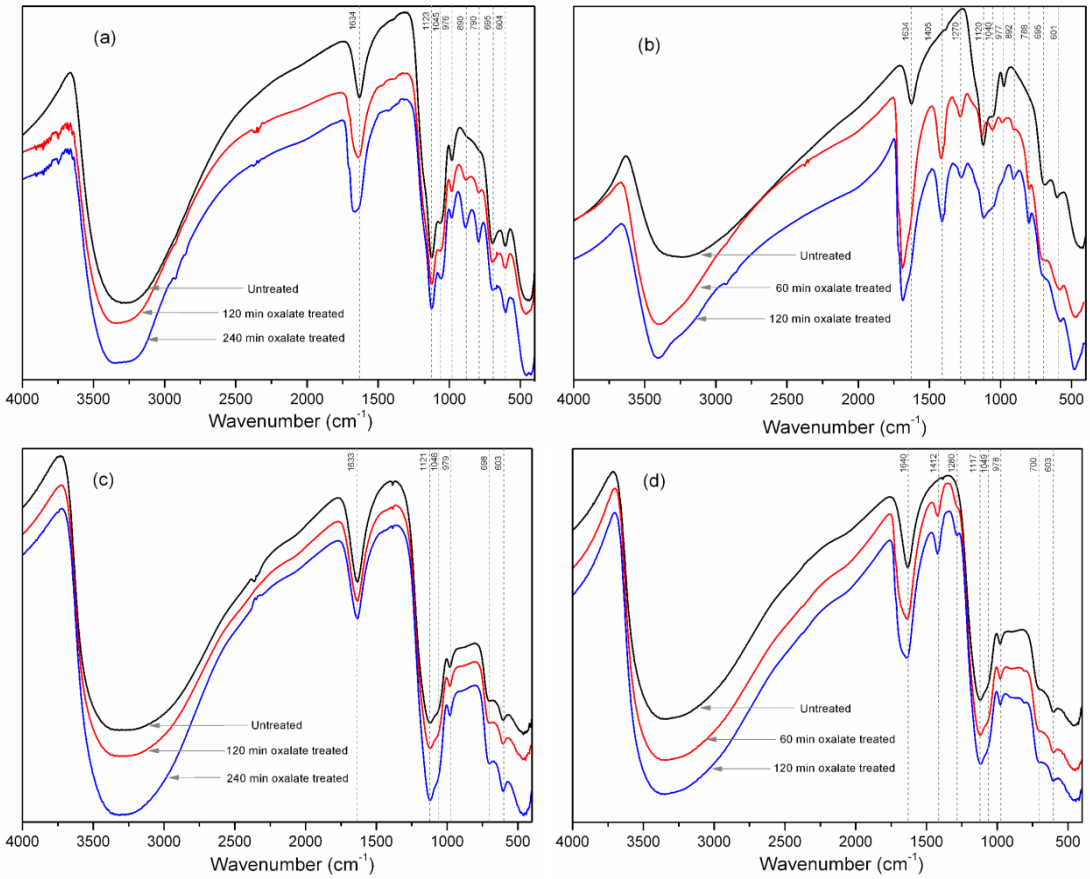

Figure 7.8: FTIR spectra of the precipitates before and after AAO dissolution: (a) and (b) for bi-metallic samples FN-2 and FN-4, respectively; (c) and (d) for multi-metallic samples FNAC-2 and FNAC-6, respectively.

The band located at 604 cm^{-1} is closely related to the stretching vibration of lattice sulphate (v_4−SO_4) (Myneni, 2000; Nakamoto, 1986). If this band belongs to an exclusively structural sulphate bonding into the tunnels of schwertmannite crystals, as indicated by Regenspurg (2002), it is probable that some schwertmannite still remained even after 240 min oxalate extraction for sample FN-2 (Figure 7.8 (a)). This conclusion is inconsistent with the findings of the work by Bigham *et al.* (1990), who suggested nearly complete dissolution for natural and synthetic schwertmannite could be achieved within 15 min with AAO at pH 3. It is perhaps more appropriate to assign this band generally to the v_4−SO_4 mode rather than to the specific structural sulphate belonging to schwertmannite. Conversely, the results of AAO dissolution are heavily dependent on experimental conditions, such as solid/solution ratio, temperature, time of reaction and the presence of foreign ions, especially the reduced species, *e.g.* Fe (II) *etc*. (Cornell and Schindler, 1987). It is also known that oxalate can form strong surface complexes. The IR spectra study on oxalate absorption by Hug and Bahnemann (2006) showed that absorbed oxalate displayed two prominent bands at 1715−1713 cm^{-1} (v_sC=O) and 1696−1679 cm^{-1} (v_{as}C=O), and another two strong peaks at 1424−1412 cm^{-1} (v_sC−O+v_sC−C) and 1279−1264 cm^{-1} (v_{as}C−O+v_{as}C−C). Similar conclusions were presented by Norén and Persson (2007). In the present study, the notable shift of the peak at 1634 cm^{-1} for AAO treated samples FN-2 and FN-4 suggests that oxalate remains in the residue. Also, the significant formation of the peaks at about 1270 and 1410 cm^{-1} for AAO treated samples FN-4 and FNAC-6 are the result of the formation of surface oxalate complexes.

The presence of goethite can be confirmed from the appearance of the intense pair of bands at 890 and 790 cm^{-1} due to the Fe−O−H bending vibrations. These are considered to be distinctive peaks for goethite (Schwertmann and Carlson, 2005). Notably, these bands were not resolved for untreated bi-metallic samples FN-2 and FN-4, but appeared after AAO dissolution, and became sharper with increasing extraction time. These observations suggested that such small amounts of goethite

can only be detected after removing most of the poorly structurally-ordered phases. The presence of goethite was not apparent in multi-metallic sample FNAC-2 (Figure 7.8 (c)). However, very weak peaks distinctive for goethite appeared for AAO treated sample FNAC-6 (Figure 7.8 (d)). This suggests the presence of a small amount of goethite, although no direct evidence was found in previous XRD and DXRD analysis.

Of particularly interest in the present study are the infrared absorption regions between 950 and 1300 cm^{-1}, which are closely related to the symmetry of absorbed sulphate complexes. More in-depth discussion of the surface complexation model of sulphate adsorption can be found elsewhere (Myneni, 2000; Nakamoto, 1986). The uncoordinated sulphate is T_d (tetrahedral) symmetry. The symmetry of sulphate can be reduced from T_d to either C_{3v} (monodentate, corner-sharing) or C_{2v} (bidentate binuclear, edge-sharing) with changes in local coordination and the bonding environment. For the AAO untreated and treated samples FN-2 and FN-4 (Figure 7.8 (a) and (b)), the presence of nondegenerate symmetric stretch v_1−SO_4 at 976 cm^{-1}, and the peak at 1123 cm^{-1} and shoulder at 1045 cm^{-1} that originate from the triply degenerate asymmetric stretch v_3−SO_4 suggest that the sulphate was absorbed to form a monodentate surface complex with C_{3v} symmetry. After 120 min AAO dissolution, the bands at 1040 and 976 cm^{-1} for treated sample FN-4 became very weak (Figure 7.8 (b)), but the main band centred near 1120 cm^{-1} can still be observed clearly. Thus, it is assumed that the sulphate still retained C_{3v} coordination character. The weaker bands located at 1040 and 976 cm^{-1} were assigned to the interaction of sulphate with goethite, which is similar to the observation by Parfitt and Smart (1978). For the FTIR spectra of multi-metallic samples FNAC-2 and FNAC-6 (Figure 7.8 (c) and (d)), sulphate still retained C_{3v} symmetry character, but the 1040 cm^{-1} peak was very weak and presented as a shoulder in these samples. Conversely, the stronger intensity of 1040 cm^{-1} bands observed in bi-metallic samples FN-2 and FN-4 probably suggested that the splitting of the v_3−SO_4 mode is better resolved. The bi-metallic samples contain a much higher proportion of lower

symmetry sulphate.

Much interest has focused on the study of sulphate adsorption onto iron oxides by vibrational spectroscopy. However, the complexation models for sulphate are still under debate. These can be affected by sample preparation procedures and data collection techniques. An early study on sulphate adsorption on iron oxides by Parfitt and Smart (1978) suggested that sulphate adopted C_{2v} symmetry when absorbed onto goethite with the v_3 band at 1254 cm^{-1} for air-dried sample and 1282 cm^{-1} for evacuated dried sample. However, Persson and Lövgren (1996) questioned the assignments of such high frequencies to the v_3 mode. They examined the sulphate complexes at the goethite-water interface by Diffuse−Reflectance (DR) spectroscopy, and suggested that sulphate exhibited T_d symmetry within the pH range 3 to 8, but that a weak splitting of the v_3 band appeared at 1220 cm^{-1} below pH 5 due to the presence of protonated sulphate. However, the samples examined in the study of Persson and Lövgren (1996) were diluted with KBr. Hug (1997) and Peak *et al.* (1999) indicated that sulphate adsorption is sensitive to changes in pH. Mixing of trace amounts of dried samples with KBr may lead to the shift of sample pH to 6 (saturated KBr solution). These can rapidly change the sulphate surface complex. From *in situ* Attenuated Total Reflection (ATR) FTIR studies on hydrated mineral surfaces, Hug (1997) observed C_{3v} symmetry with three bands between 950 and 1150 cm^{-1} in the pH ranges of 3 to 6. Peak *et al.* (1999) suggested that sulphate adsorption is a function of both pH and ionic strength; the symmetry reduces with decreasing pH and increasing ionic strength. The study of Paul *et al.* (2005) indicated that sulphate adsorbed onto a mineral surface is unlikely to preserve a well-defined high-symmetry point group. Sulphate adsorbs as a bidentate bridging or monodentate surface complexes under most experimental conditions. Drying strongly changes sulphate coordination or speciation, which results in greater v_3 band splitting with notable shifting of the bands. These conclusions are in closely agreement with the findings of Parfitt and Smart (1978) and Peak *et al.* (1999). In the studies of Paul *et al.* (2005) as well as Persson and Lövgren (1996), the higher frequency component of

the split v_3–SO_4 absorption band which results from C_{2v} symmetry was most likely to occur between 1200 and 1250 cm^{-1}. This is consistent with the conclusion that the peaks at 1270 and 1280 cm^{-1} for AAO treated samples FN-4 and FNAC-6 in the present study, respectively, were due to the interaction of oxalate from AAO dissolution.

7.4 CONCLUSION

A detailed mineralogical characterization was performed on the iron-rich precipitates from synthetic nickel laterite leach solutions by a combination of several techniques that include selective AAO dissolution, XRD, DXRD, SEM and FTIR spectroscopy. The initial XRD analysis of AAO-untreated samples showed that the structural ordering of precipitates was lower in the presence of foreign metallic cations. Nickel, aluminium and chromium retarded the transformations of schwertmannite and/or ferrihydrite to goethite, while aluminium and chromium suppressed the formation of 6-line ferrihydrite. All precipitates produced at 25 ºC dissolved much slower compared to those precipitated at 85 ºC. The presence of aluminium and chromium ions strongly influences the dissolution rates of iron-rich precipitates in AAO solutions. Multi-metallic precipitates showed a much slower dissolution rate compared to bi-metallic precipitates. Furthermore, XRD analysis of AAO treated samples showed that the presence of goethite in bi-metallic samples can only be detected after removing most of the oxalate-extractable schwertmannite and 6-line ferrihydrite. Due to the strong retarding ability of aluminium and chromium on the transformation of schwertmannite and ferrihydrite to goethite, poorly ordered schwertmannite was suggested to be the main phase in the multi-metallic precipitates even after AAO dissolution. The corresponding DXRD patterns indicated that schwertmannite was the most readily dissolved precipitate in AAO solution, and schwertmannite dissolved preferentially relative to 6-line ferrihydrite. FTIR analysis confirmed the presence of goethite in the bi-metallic precipitates and suggested that the sulphate is present to a greater extent in lower symmetry environments.

CHAPTER 8

SUMMARY AND FUTURE WORK

8.1 SUMMARY

Specific conclusions have been drawn at the end of each chapter. For completeness, further general summary are made here by combining points from the previous conclusions. This thesis consists of three main parts: (1) theoretical investigation of mixed iron and nickel sulphate solutions; (2) extensive experimental investigation on the impurity-removal processes and associated nickel losses from both synthetic and real nickel laterite AL liquors; (3) characterization of iron-rich precipitates obtained. Although each part focused on different areas of research, these overlap with each other. The conclusions from one part are therefore able to help answer questions rising from others.

8.1.1 Chemical Equilibrium

A chemical equilibrium model in the Fe(III)–Ni(II)–H_2SO_4–H_2O system was developed with the effects of ionic strength and temperature taken into account. This model was able to calculate the activity of hydrogen ion and corresponding pH value at a given ionic strength and temperature in a mixed aqueous iron and nickel sulphate solution. The modelling methodology presented can also be easily extended to simulate other aqueous electrolyte systems. The model developed was used to construct iron and nickel speciation diagrams, which clearly demonstrated the changes of equilibrium relationships between ferric and nickel species. Another important application of this model was to calculate a saturation index and predict precipitation and dissolution behaviours of iron oxides. It was found that schwertmannite is the dominant phase when the precipitation reaction occurs at pH values above 2.5. This prediction was consistent with the experimental results of

subsequent chapters.

8.1.2 Impurity removal and nickel loss

Considerable effort has been put into the experimental study of the relationships between impurities removal and nickel losses from nickel laterite AL liquors. This was achieved by initially investigating simple synthetic leach solutions containing Fe(III)+Ni(II), then more complicated solutions containing Fe(III)+Ni(II)+Al(III), Fe(III)+Ni(II)+Cr(III), and Fe(III)+Ni(II)+Al(III)+Cr(III), and finally real leach solutions. The strategy of Design of Experiments (DOE) was widely adopted throughout these studies. A semi-batch precipitation process was used in all cases, which is simple in design and operation. This technique used a method combining both dilution and neutralization, which avoids directly neutralizing nickel laterite AL liquors with high ionic concentrations in a batch process. It is also conceivable that this process can be scaled up to a fully continuous process with several reactors arranged in series or parallel.

From the study of the effect of iron precipitation on nickel losses in the Fe(III)+Ni(II) binary system, the solution pH, precipitation temperature and the initial Fe/Ni ratio in PLS were found to be the important factors affecting iron removal efficiency and the level of nickel loss. For the Fe(III)+Ni(II)+Al(III) and Fe(III)+Ni(II)+Cr(III) ternary systems, it was demonstrated that greater losses of nickel to the solids occurred in the presence of aluminium and chromium. Increasing solution pH and precipitation temperature favoured the precipitation of iron, aluminium and chromium, but at a cost of greater nickel losses. In order to achieve the aim of removing impurities effectively without causing significant loss of nickel, multi-stage precipitation processes were examined by carefully controlling pH and temperature. The optimum conditions for a multi-stage precipitation process were found to be at pH 3 and 55 ºC in the first stage precipitation followed by a second stage precipitation operated at pH 3 and 85 ºC. Using this multi-stage procedure, as much as 95% iron and chromium together with more than 80% aluminium can be

removed from a synthetic AL liquor containing Fe(III)+Ni(II)+Al(III)+Cr(III), with the level of nickel loss to solid kept to below 1%. The sludge showed a fast settling rate of 5.05 m/h with the addition of a cationic flocculant. Similar satisfactory results were also obtained when performing this multi-stage precipitation procedure on real leach solutions.

The investigations of the effect of water salinity on impurities removal and nickel losses suggest that the semi-batch precipitation method is able to process the PLS containing high water salinity with good nickel recovery and impurities removal efficiencies, particularly when the precipitation reactions were carried out at 85 ºC. XRD analysis of the precipitates confirmed that the poorly structural-ordered schwertmannite and/or ferrihydrite were the dominant phases. Natrojarosite can be detected when the precipitation reaction is conducted at pH 2 and 85 ºC from synthetic solution with high salinity.

8.1.3 Characterization of iron-rich precipitates

The precipitation process used in this thesis is similar to the conventional E.Z. Goethite Process, which was original developed by Allen *et al.* (1970). In the following years, many researchers suggested that the residues from E.Z. Goethite Process contained large amounts of poorly defined basic iron sulphates and iron oxyhydroxide rather than pure goethite precipitates (Claassen *et al*., 2002; Davey and Scott, 1975; Gordon and Pickering, 1975). The conflicting reports found on this topic are probably a result of the difficulties associated with the characterization of the iron-rich residues with poor structural-order. Hence, an accurate and detailed mineralogical characterization is essential to understand the nature of iron-rich residues. The present study applied several techniques that include selective AAO dissolution, XRD, DXRD, SEM and FTIR spectroscopy to characterize the complicated iron-rich precipitates from synthetic atmospheric nickel laterite leach solutions. This investigation was conducted with reference to the effects of foreign metallic cations on crystallization, dissolution behaviour and mineralogical

properties of the precipitates. From XRD analysis of AAO-untreated samples, it was demonstrated that nickel, aluminium and chromium retarded the transformations of schwertmannite and/or ferrihydrite to goethite, and that aluminium and chromium further suppressed the formation of 6-line ferrihydrite. The presence of aluminium and chromium ions strongly influences the dissolution rates of iron-rich precipitates in AAO solutions. XRD analysis of AAO-treated samples showed that the presence of goethite in the bi-metallic precipitates obtained from the solution containing Fe(III)+Ni(II) can only be detected after removing most of the oxalate-extractable schwertmannite and 6-line ferrihydrite. Of particular interest it was found that schwertmannite was the main phase in both AAO treated and untreated multi-metallic precipitates that were obtained from the solution containing Fe(III)+Ni(II)+Al(III)+Cr(III). The corresponding DXRD patterns suggested that schwertmannite was the most readily dissolved phase in AAO solution, and that schwertmannite dissolved preferentially relative to 6-line ferrihydrite. FTIR analysis confirmed the presence of goethite in the bi-metallic precipitates and suggested that the sulphate is present to a greater extent in low symmetry environments.

The results of this thesis are able to answer: (1) what are the effects of iron, aluminium and chromium precipitation on nickel losses; (2) can a precipitation process with desirable precipitation recoveries of impurities, acceptable level of nickel loss to the solids, and satisfactory sludge property be developed; (3) what are the influences of metallic cations including nickel, aluminium and chromium on the mineralogical properties of iron-rich precipitates? The aims of this thesis, as indicated in Chapter 1, due to improved understanding of the physicochemical processes that occur during the precipitation of impurities from nickel laterite AL liquors and associated nickel losses, have therefore been met.

8.2 FUTURE WORK

This thesis has made a considerable contribution to the knowledge of impurity-

removal processes and associated nickel losses from the nickel laterite atmospheric leaching system. The following section includes suggestions for future work.

8.2.1 Chemical equilibrium modelling in concentrated solutions

In this thesis, theoretical investigation of chemical equilibrium was simplified to a mixed sulphate system containing only ferric iron and nickel ions. The real leach solution from atmospheric leaching of nickel laterite, however, contains various metals other than iron and nickel, which is a concentrated multi-component system. The ion-association approach, which was implemented to develop a speciation-based model in this thesis, was confined to relatively low ionic strengths. However, high concentrations come with high non-ideal thermodynamic behavior. This often brings significant challenges in chemical modelling. The physicochemical and thermodynamic properties of concentrated multi-component systems with high ionic strength, needs to be further investigated. In contrast to the ion-association model, the Pitzer ion interaction model describes the properties of solution in terms of physicochemical interactions between free ions. The significance of this approach is that it has a good accuracy for an electrolyte solution with ionic strength up to 10 M. The Pitzer's ion interaction approach requires a linear summation of a large quantity of parameters obtained from single electrolyte solutions by fitting experimental osmotic and activity coefficients. However, the Pitzer model has limitations in determining the cation-anion interaction of all trace species in solutions. In this case, the extended Pitzer model combined with an ion-paring approach would be feasible, as noted from the speciation investigations in saline and natural water performed by Millero *et al*. (1995). Alternatively, a hybrid ion-association-interaction approach, as developed by Baghalha and Papangelakis (1998), would also be technically feasible in describing the chemistry and thermodynamics of the participating electrolytes in real industrial laterite leach solutions.

8.2.2 Improving the crystallization of iron-rich precipitates

Characterization of the precipitates obtained identified that schwertmannite and/or ferrihydrite are the dominant phases. The presence of large amounts of these poorly structural-ordered phases can result in high uptake of nickel. On the other hand, formation of high structurally-ordered phases would have fewer defect sites for nickel to attach. Therefore, it is worth conducting further investigation on improving the crystallinity of precipitation residues.

The process can be conducted in a fully continuous pilot-plant scale precipitation process, such as continuous stirred tank reactors (CSTR), which can be arranged in parallel or series. The pregnant leach solution can be treated with multi-stage precipitation procedures from one reactor to the next, using different combinations of pH and temperature. The slurry produced from the last reactor can be recycled to the first reactor to act as seed to increase the precipitation kinetics and improve crystallinity of the precipitates. There is also the option to perform solid/liquid separation after the first and second stages, *i.e.*, the first via Counter Current Decantation (CCD) and second via filtration. Underflow from CCD could be recycled as seed and the filter cake repulped for recycle to recover nickel. Thus water balance/usage would become a key factor in this case.

For supersaturation control, a continuous process is a far superior method to batch or semi-batch methods. A continuous process can offer a stable supersaturation environment rather than variable supersaturation conditions encountered in batch or semi-batch modes. Precipitation generally occurs from a high supersaturation solution, resulting in fast nucleation and consequent formation of a large number of small crystals. This process can result in fragile and poorly crystalline precipitates. Keeping a low supersaturation has the following benefits in improving precipitate quality: avoiding the formation of large and immobile polymeric species; decreasing the aggregation of clusters into agglomerates; facilitating the surface integration reaction due to the larger solid/liquid interface (Demopoulos, 2009). However, there

is typically not enough time to grow large particle size precipitates. A suitable residence time in a fully continuous process, which was beyond the scope of this study, is required to ensure iron-rich precipitates have enough time to crystallize and precipitate at steady state.

Improving the crystallinity of precipitates can also be achieved by adding foreign crystalline seeds (iron oxides) directly to the reactor before the precipitation reactions occur, which could be simply applied in the semi-batch precipitation process used in this thesis. However, one potential problem would be the characterization of the precipitates by XRD. Take goethite seeding as an example, it would be difficult to identify whether the presence of goethite seed promotes the formation of further goethite, as a higher seed loading could result in a greater intensity of the goethite diffraction peaks. Hence, one needs to add an internal standard and perform Quantitative X-Ray Diffraction (QXRD) to determine the goethite content of the final iron-rich precipitates. This will require a good fit to the background and suitable crystallographic models for the other phases. However, the presence of large amounts of poorly structural-ordered schwertmannite and/or ferrihydrite poses a potential problem in this approach.

In addition, the seeding of nickel laterite atmospheric leach liquor should be investigated further to better understand the effects upon the complex precipitation behavior of iron oxides and associated nickel loss mechanisms. This includes but is not limited to the following:

- Study the effects of seeding on particle sizes and surface areas of precipitates to determine whether seeding promotes the formation of larger and denser particles with less surface area that result in less uptake of nickel.
- Study the effects of seeding on improving sludge properties such as settling rate.

8.2.3 The effect of magnesium ions

This thesis studied the relationships between trivalent impurity ions and nickel losses. However, real leach liquors derived from the leaching of laterite ores, especially from the atmospheric leaching of saprolite ores, will contain a significant amount of magnesium ions (as Mg^{2+}). Magnesium ions are known to exert a bisulphate "buffering" effect which is very pronounced in high temperature and pressure acid leach systems. Even at moderate temperature under atmospheric conditions, such as 90 to 100 ºC, the presence of significant magnesium may be important. Hence, it is worth investigating any effect upon this important factor on impurity rejection and nickel losses in greater detail.

8.2.4 The effect of ferrous ions

Except for the large amounts of ferric ions in nickel laterite AL liquors, ferrous ions (as Fe^{2+}) can also be present in various proportions relative to ferric ions, often depending upon the nature of the ore that is leached. The removal of ferrous ions from solution requires both oxidation and precipitation processes. The oxidation of ferrous ions at lower pH is more difficult or slower (Morgan and Lahav, 2007). Thus, it would be interesting to determine if the simultaneous oxidation and hydrolysis of ferrous ions result in a higher level of nickel loss than the prior oxidation of ferrous ions at a lower pH, followed by an increase of pH for hydrolysis. Important parameters that would need to be taken into account are the oxidation method (*i.e.* O_2, H_2O_2, SO_2/O_2 or air), oxidation rate, E_h value (a function of Fe^{3+}/Fe^{2+}) and catalyst (*e.g.* Cu^{2+}).

A recent study by Burton *et al.* (2008) suggested that Fe^{2+} played a catalytic role in accelerating the transformation of schwertmannite to goethite. Although this study focused on acid-sulphate media with pH value above 5, it does give some indication of the schwertmannite and goethite formation mechanisms. It would therefore also be worth examining if the presence of ferrous iron affects the mineralogy of iron-rich

precipitates in the precipitation processes used in this thesis.

8.2.5 Improving dewatering and sludge properties

As good dewatering and sludge properties are critical in industrial applications, methods for improving settling rate, sludge volume, filtration rate, cake moisture and solids loading need to be further investigated. This study would involve the use of effective flocculants with optimization of the amount required to increase aggregation.

8.2.6 Test work using other neutralization agents

Although magnesia is an expensive reagent, it is still worth testing other cheaper magnesium-containing neutralization agents, such as magnesite, dolomite and saprolite ores. There is also scope to further examine Ca-containing reagents. The effects of the neutralizing agent upon the solid-liquid separation properties of the precipitates could also be considered.

8.2.7 Nickel speciation within the iron-rich precipitates

Nickel loss occurs as either co-precipitation (adsorption) or incorporation into the structure of iron oxides. In some cases, the trace level of nickel present in iron-rich precipitates often causes difficulty in tracking nickel by Scanning Electron Microscopy coupled with Energy Dispersive Spectroscopy (SEM-EDS), as SEM-EDS can only collect data from a sample's surface to 1 μm depth with a semi-quantitative analysis limit of 0.1 wt%.

The low level nickel uptake by iron oxides also results in only small changes in the crystal structure and, the shape and position of XRD peaks. This makes conventional X-ray diffraction (XRD) insensitive for the detection of discrete crystalline phases present in amounts smaller than 1% in bulk samples. However, some high sensitivity techniques are useful for analyzing the iron-rich samples containing trace-level

amounts of nickel. For instance, synchrotron radiation-based X-ray absorption spectroscopy (XAS) can provide insight into the local coordination environment. This would provide fundamental and mechanistic information on the substitution of nickel for iron. XAS requires a high intensity X-ray source that is typically one million times more intense than a conventional X-ray tube, and is only therefore available at synchrotron facilities. The high intensities used for XAS make it possible to examine most elements at concentrations down to the ppm level.

8.2.8 The mechanism of iron oxides formation

The mechanism of iron oxides (including goethite, schwertmannite and ferrihydrite) formation from both synthetic and real AL liquors, needs to be clearly defined. This involves investigation of the precipitation mechanisms of iron oxides that are dominated by nucleation and aggregation, as well as the interphase-transformations. Schwertmannite and ferrihydrite are thermodynamically unstable, and tend to transform over time to more stable iron oxides such as goethite. However, there is no direct evidence to confirm whether schwertmannite or ferrihydrite is a necessary intermediate for the formation of goethite. There seems to be a balance or competition mechanism rather than a single mechanism path. In this regard, ^{57}Fe Mössbauer absorption spectroscopy may be of benefit to determine the transformation sequence. ^{57}Fe Mössbauer absorption spectroscopy is a solid-state nuclear probe technique that relies on the magnetic behavior of iron in a crystal structure. The magnetic ordering in iron oxides differ considerably, which allows Mössbauer spectroscopy to unequivocally identify and quantify various iron oxides in mixtures (Cornell and Schwertmann, 2003). XRD is relatively insensitive to variations in schwertmannite and ferrihydrite structures due to small particle size and/or poor structural order. Unlike XRD, distinct spectral signals can be obtained from both poorly and highly structural-ordered iron using ^{57}Fe Mössbauer absorption spectroscopy. Furthermore, Mössbauer absorption spectroscopy also provides important information on particle size and isomorphous substitution. This may

provide further insight into the substitution mechanism(s) of metallic cations such as nickel.

REFERENCES

Acero, P., Ayora, C., Torrentó, C. and Nieto, J.M., 2006. The behavior of trace elements during schwertmannite precipitation and subsequent transformation into goethite and jarosite. Geochimica et Cosmochimica Acta, 70: 4130-4139.

Agatzini-Leonardou, S. and Burkin, A.R., 1985. Statistical approach to the precipitation of iron as 'goethite'. Transactions of the Institution of Mining and Metallurgy Section C: Mineral Processing and Extractive Metallurgy, 94: C105-114.

Agatzini-Leonardou, S. and Dimaki, D., 2000. Method for extraction of nickel and/or cobalt oxide ores by heap leaching with a dilute sulphuric acid solution, prepared from sea water, at ambient temperature. Greek Patent No. 1, 003,569/2000.

Agatzini-Leonardou, S., Dimaki, D. and Boskos, E., 1997. Extraction of nickel and cobalt from Greek low-grade nickel oxide ores by heap leaching. In: W.C. Cooper and I. MihaylovI (Editors), Nickel-Cobalt 97 International Symposium, Sudbury, Ontario, Canada, 489-503.

Agatzini-Leonardou, S., Tsakiridis, P.E., Oustadakis, P., Karidakis, T. and Katsiapi, A., 2009. Hydrometallurgical process for the separation and recovery of nickel from sulphate heap leach liquor of nickeliferrous laterite ores. Minerals Engineering, 22: 1181-1192.

Albarède, F., 1995. Introduction to geochemical modeling. Cambridge University Press, Cambridge.

Allen, R.W., Haigh, C.J. and Hamdorf, C.J., 1970. An improved method of removing dissolved ferric iron from iron-bearing solution. Australian Patent No. 424, 095.

Angelopoulos, P., Evangelaras, H. and Koukouvinos, C., 2009. Analyzing

unreplicated 2^k factorial designs by examining their projections into k-1 factors. Quality and Reliability Engineering International 26: 223-233.

Appelo, C.A.J. and Postma, D., 2005. Geochemistry, groundwater and pollution. A.A. Balkema Publishers, Leiden.

Arroyo, J.C. and Neudorf, D.A., 2004. Atmospheric leach process for the recovery of nickel and cobalt from limonite and saprolite ores. US Patent No. 6, 680, 035 B2.

Babčan, J., 1971. Synthesis of jarosite $KFe_3(SO_4)_2(OH)_6$. Geologicky Zbornik-Geologica Carpathica, 22: 299-304.

Baes, C.F. and Mesmer, R.E., 1976. The hydrolysis of cations. Wiley, New York.

Baes, C.F. and Mesmer, R.E., 1981. The thermodynamics of cation hydrolysis. The American Journal of Science, 281: 935-962.

Baghalha, M. and Papangelakis, V., 1998. The ion-association-interaction approach as applied to aqueous H_2SO_4-$Al_2(SO_4)_3$-$MgSO_4$ solutions at 250°C Metallurgical and Materials Transactions B, 29: 1021-1030.

Benjamin, M.M. and Leckie, J.O., 1981. Conceptual model for metal-ligand-surface interactions during adsorption. Environmental Science and Technology, 15: 1050-1057.

Beukes, J.P., Giesekke, E.W. and Elliott, W., 2000. Nickel retention by goethite and hematite. Minerals Engineering, 13: 1573-1579.

Bienermann, G. and Schindler, P., 1957. On the solubility product of precipitated iron (III) hydroxide. Acta Chemica Scandinavica, 11: 731-740.

Bigham, J.M., Carlson, L. and Murad, E., 1994. Schwertmannite, a new iron

oxyhydroxysulphate from Pyhäsalmi, Finland, and other localities. Mineralogical Magazine, 58: 641-648.

Bigham, J.M. and Nordstrom, D.K., 2000. Iron and aluminum hydroxysulphates from acid sulphate waters. In: C.N. Alpers, J.L. Jambor and D.K. Nordstrom (Editors), Sulphate minerals: crystallography, geochemistry, and environmental significance. Mineralogical Society of America, Washington, DC, 351-403.

Bigham, J.M., Schwertmann, U., Carlson, L. and Murad, E., 1990. A poorly crystallized oxyhydroxysulfate of iron formed by bacterial oxidation of Fe (II) in acid mine waters. Geochimica et Cosmochimica Acta, 54: 2743-2758.

Bigham, J.M., Schwertmann, U., Traina, S.J., Winland, R.L. and Wolf, M., 1996. Schwertmannite and the chemical modeling of iron in acid sulfate waters. Geochimica et Cosmochimica Acta, 60: 2111-2121.

Blakey, B.C., 1994. Synthesis and solubility of hydronium alunite under direct sulphuric acid pressure leaching conditions. Master Thesis, University of Toronto, Toronto.

Blakey, B.C. and Papangelakis, V.G., 1996. A study of solid-aqueous equilibria by the speciation approach in the hydronium alunite-sulfuric acid-water system at high temperatures. Metallurgical and Materials Transactions B, 27B: 555-566.

Blesa, M.A. and Matijević, E., 1989. Phase transformations of iron oxide, oxohydroxides, and hydrous oxides in aqueous media. Advances in Colloid and Interface Science, 29: 173-221.

Bodson, F.J.J., 1972. Recovery of zinc values from zinc plant residue. U.S. Patent No. 3652264.

Boily, J.F., Gassman, P.L., Peretyazhko, T., Szanyi, J. and Zachara, J.M., 2010. FTIR spectral components of schwertmannite. Environmental Science and Technology, 44: 1185-1190.

Bolin, N.J. and Sundkvist, J.E., 2008. Two-stage precipitation process of iron and arsenic from acid leaching solutions. Transactions of Nonferrous Metals Society of China, 18: 1513-1517.

Bottero, J.Y., Manceau, A., Villieras, F. and Tchoubar, D., 1994. Structure and mechanisms of formation of iron oxide hydroxide (chloride) polymers. Langmuir, 10: 316-319.

Box, G.E.P. and Behnken, D.W., 1960. Some new three level designs for the study of quantitative variables. Technometrics, 2: 455-475.

Box, G.E.P. and Cox, D.R., 1964. An analysis of transformations. Journal of the Royal Statistical Society, 26B: 211-246.

Box, G.E.P., Hunter, W.G. and Hunter, J.S., 1978. Statistics for experiments: An introduction to design, data analysis, and model building. John Wiley and Sons, Inc., New York.

Burkin, A.R., 2001. Chemical hydrometallurgy-theory and principles. Imperial College Press, London.

Burton, E.D., Bush, R.T., Sullivan, L.A. and Mitchell, D.R.G., 2008. Schwertmannite transformation to goethite via the Fe(II) pathway: Reaction rates and implications for iron-sulfide formation. Geochimica et Cosmochimica Acta, 72: 4551-4564.

Byrne, R.H. and Kester, D.R., 1976. Solubility of hydrous ferric oxide and iron speciation in seawater. Marine Chemistry, 4: 255-274.

Byrne, R.H. and Luo, Y.R., 2000. Direct observations of nonintegral hydrous ferric oxide solubility products $K^*_{so}=[Fe^{3+}][H^+]^{-2.86}$. Geochimica et Cosmochimica Acta, 64: 1873-1877.

Byrne, R.H., Luo, Y.R. and Young, R.W., 2000. Iron hydrolysis and solubility revisited: observations and comments on iron hydrolysis characterizations. Marine Chemistry, 70: 23-35.

Campbell, A.S. and Schwertmann, U., 1984. Iron oxide mineralogy of placic horizons. Journal of Soil Science, 35: 569-582.

Caraballo, M.A., Rötting, T.S., Nieto, J.M. and Ayora, C., 2009. Sequential extraction and DXRD applicability to poorly crystalline Fe- and Al-phase characterization from an acid mine water passive remediation system. American Mineralogist, 94: 1029-1038.

Carvalho-e-Silva, M.L., Ramos, A.Y., Tolentino, H.C.N., Enzweiler, J., Netto, S.M. and Alves, M.C.M., 2003. Incorporation of Ni into natural goethite. An investigation by X-ray absorption spectroscopy. American Mineralogist, 88: 876-882.

Casas, J.M., Alvarez, F. and Cifuentes, L., 2000. Aqueous speciation of sulfuric acid-cupric sulfate solutions. Chemical Engineering Science, 55: 6223-6234.

Cavasino, F.P., 1968. Temperature-jump study of the kinetics of the formation of the monosulfato complex of iron(III). The Journal of Physical Chemistry, 72: 1378-1384.

Chang, Y., Zhai, X., Li, B. and Fu, Y., 2010. Removal of iron from acidic leach liquor of lateritic nickel ore by goethite precipitate. Hydrometallurgy, 101: 84-87.

Cifuentes, L., Casas, J.M. and Simpson, J., 2006. Temperature dependence of the speciation of copper and iron in acidic electrolytes. Chemical Engineering Research

and Design, 84: 965-969.

Claassen, J.O., 2002. Characterisation and optimisation of the Zincor iron process. M.Eng. Thesis, University of Pretoria.

Claassen, J.O., 2006. Product quality parameters in the reaction crystallization of metastable iron phases from zinc-rich solutions. Ph.D Thesis, University of Pretoria.

Claassen, J.O., Meyer, E.H.O., Rennie, J. and Sandenbergh, R.F., 2002. Iron precipitation from zinc-rich solutions defining the Zincor Process. Hydrometallurgy, 67: 87-108.

Claassen, J.O. and Sandenbergh, R.F., 2006. Particle growth parameters in the precipitation of metastable iron phases from zinc-rich solutions. Hydrometallurgy, 84: 165-174.

Cornell, R.M., Giovanoli, R. and Schneider, W., 1989. Review of the hydrolysis of iron(III) and the crystallization of amorphous iron (III) hydroxide hydrate. Journal of Chemical Technology and Biotechnology, 46: 115-134.

Cornell, R.M., Giovanoli, R. and Schneider, W., 1992. The effect of nickel on the conversion of amorphous iron (III) hydroxide into more crystalline iron oxides in alkaline media. Journal of Chemical Technology and Biotechnology, 53: 73-79.

Cornell, R.M., Posner, A.M. and Quirk, J.P., 1976. Kinetics and mechanisms of the acid dissolution of goethite (α-FeOOH). Journal of Inorganic and Nuclear Chemistry, 38: 563-567.

Cornell, R.M. and Schindler, P.W., 1987. Photochemical dissolution of goethite in acid/oxalate solution. Clays and Clay Minerals, 35: 347-352.

Cornell, R.M. and Schwertmann, U., 2003. The iron oxides: structure, properties,

reactions, occurrences and uses. Wiley-VCH GmbH and Co. KGaA, Weinheim.

Crawford, R.J., Harding, I.H. and Mainwaring, D.E., 1993. Adsorption and coprecipitation of single heavy metal ions onto the hydrated oxides of iron and chromium. Langmuir, 9: 3050-3056.

Criss, C.M. and Cobble, J.W., 1964a. The thermodynamic properties of high temperature aqueous solutions. IV. Entropies of the ions up to 200°C and the correspondence principle. Journal of the American Chemical Society, 86: 5385-5390.

Criss, C.M. and Cobble, J.W., 1964b. The thermodynamic properties of high temperature aqueous solutions. V.The calculation of ionic heat capacities up to 200°C. Entropies and heat capacities above 200°C. Journal of the American Chemical Society, 86: 5390-5393.

Cubeddu, F., Piasentin, M., Reilly, F., Meregalli, L. and Tolomio, M., 1996. The paragoethite process at the Enirisorse-Porto Vesme plant. In: J.E. Dutrizac and G.B. Harris (Editors), Proceedings of the second International Symposium on Iron Control in Hydrometallurgy. Canadian Institue of Mining, Metallurgy and Petroleum, Ottawa, 147-161.

Dalvi, A.D., Bacon, W.G. and Osborne, R.C., 2004. The past and the future of Nickel laterites, PDAC 2004 International Convention, Trade Show and Investors Exchange, Toronto, 7-10.

Daniel, C., 1959. Use of half-normal plots in interpreting factorial two-level experiments. Technometrics, 1: 311-341.

Daniele, P.G., Rigano, C., Sammartano, S. and Zelano, V., 1994. Ionic strength dependence of formation constants-XVIII. The hydrolysis of iron (III) in aqueous KNO_3 solutions. Talanta, 41: 1577-1582.

Das, G.K., Acharya, S., Anand, S. and Das, R.P., 1996. Jarosites: a review. Mineral Processing and Extractive Metallurgy Review, 16: 185-210.

Das, K., 1988. Single ion activities in aqueous sulfuric acid solutions: A new extra-thermodynamic assumption. Journal of Solution Chemistry, 17: 327-336.

Davey, P.T. and Scott, T.R., 1975. Formation of β-FeOOH and α-Fe_2O_3 in the Goethite Process. Transactions of the Institution of Mining and Metallurgy Section C: Minerals Processing and Extractive Metallurgy, 84: C83-86.

Davey, P.T. and Scott, T.R., 1976. Removal of iron from leach liquors by the "Goethite" process. Hydrometallurgy, 2: 25-33.

Davies, C.W., 1962. Ion Association. Butterworths, London.

Demopoulos, G.P., 2009. Aqueous precipitation and crystallization for the production of particulate solids with desired properties. Hydrometallurgy, 96: 199-214.

Diakonov, I.I., 1998. Thermodynamic properties of iron oxides and hydroxides; III, Surface and bulk thermodynamic properties of lepidocrocite (γ-FeOOH) to 500 K. European Journal of Mineralogy, 10: 31-41.

Dickson, A.G., Wesolowski, D.J., Palmer, D.A. and Mesmer, R.E., 1990. Dissociation constant of bisulfate ion in aqueous sodium chloride solutions to 250 degree C. The Journal of Physical Chemistry, 94: 7978-7985.

Dirksen, J.D. and Ring, T.A., 1991. Fundamentals of crystallization kinetic effects on particle size distributions and morphology. Chemical Engineering Science, 46: 2389-2472.

Dold, B., 2003a. Dissolution kinetics of schwertmannite and ferrihydrite in oxidized mine samples and their detection by differential X-ray diffraction (DXRD). Applied

Geochemistry, 18: 1531-1540.

Dold, B., 2003b. Speciation of the most soluble phases in a sequential extraction procedure adapted for geochemical studies of copper sulfide mine waste. Journal of Geochemical Exploration, 80: 55-68.

Dousma, J., den Ottelander, D. and de Bruyn, P.L., 1979. The influence of sulfate ions on the formation of iron(III) oxides. Journal of Inorganic and Nuclear Chemistry, 41: 1565-1568.

Dutrizac, J.E., 1987. An overview of iron precipitation in hydrometallurgy. In: G.L. Strathdee, M.O. Klein and L.A. Melis (Editors), Crystallization and Precipiation. Pergamon Press, Saskatoon, Canda, 259-283.

Dutrizac, J.E. and Chen, T.T., 2004. Factors affecting the incorporation of cobalt and nickel in jarosite-type compounds. Canadian Metallurgical Quartely, 43: 305-320.

Dutrizac, J.E. and Dinardo, O., 1983. The co-precipitation of copper and zinc with lead jarosite. Hydrometallurgy, 11: 61-78.

Dutrizac, J.E. and Jambor, J.L., 2000. Jarosites and their application in hydrometallurgy. In: C.N. Alpers, J.L. Jambor and D.K. Nordstrom (Editors), Sulphate minerals: crystallography, geochemistry, and environmental significance. Mineralogical Society of America, Washington, 405-452.

Dutrizac, J.E. and Kaiman, S., 1976. Synthesis and properties of jarosite-type compounds. The Canadian Mineralogist, 14: 151-158.

Eggleton, R.A. and Fitzpatrick, R.W., 1988. New data and a revised structural model for ferrihydrite. Clays and Clay Minerals, 36: 111-124.

España, J.S., 2007. Chapter 7 - The behavior of iron and aluminum in acid mine

drainage: speciation, mineralogy, and environmental significance. In: M.L. Trevor (Editor), Thermodynamics, Solubility and Environmental Issues. Elsevier, Amsterdam, 137-150.

Filippou, D., Demopoulos, G.P. and Papangelakis, V.G., 1995. Hydrogen ion activities and species distribution in mixed metal sulfate aqueous systems. AIChE Journal, 41: 171-184.

Flynn, C.M., 1984. Hydrolysis of inorganic iron(III) salts. Chemical Reviews, 84: 31-41.

Fox, L.E., 1988. The solubility of colloidal ferric hydroxide and its relevance to iron concentrations in river water. Geochimica et Cosmochimica Acta, 52: 771-777.

Galster, H., 1991. pH Measurement: fundamentals, methods, applications, instrumentation VCH Verlagsgesllschaft mbH, Weinheim.

Garside, J., 1985. Industrial crystallization from solution. Chemical Engineering Science, 40: 3-26.

Giovanoli, R. and Cornell, R.M., 1992. Crystallization of metal substituted ferrihydrites. Zeitschrift für Pflanzenernährung und Bodenkunde, 155: 455-460.

Gordon, A. and Pickering, R., 1975. Improved leaching technologies in the electrolytic zinc industry. Metallurgical and Materials Transactions B, 6B: 43-53.

Gregory, J., 1985. The action of polymeric flocculants in flocculation, sedimentation and consolidation. In: B.M. Moudgil and P. Somasundaran (Editors), Flocculation, sedimentation and consolidation: Proceedings of the Engineering Foundation Conference. American Institute of Chemical Engineers, Sea Island, Georgia, 125-137.

Guise, L. and Castro, F., 1996. Iron, aluminium and chromium co-elimination by hydrolytic precipitation from nickel- and cobalt-containing sulphuric acid solutions. In: J.E. Dutrizac and G.B. Harris (Editors), Iron control and disposal: proceedings of the Second International Symposium on Iron Control in Hydrometallurgy. Canadian Institute of Mining, Metallurgy and Petroleum, Ottawa, 275-286.

Gupta, G.K. and Mukherjee, T.K., 1990. Hydrometallurgy in extraction processes, Volume II. CRC Press, Florida.

Gustafsson, J.P., 2011. Visual MINTEQ ver. 3.0, Availabe from: <http://www2.lwr.kth.se/English/OurSoftware/vminteq/index.html> [Accessed: 10 January 2012].

Han, K.N., Narita, E. and Lawson, F., 1982. The coprecipitation behavior of Co (II) and Ni (II) with Fe (III), Cr (III) and Al (III) from aqueous ammoniacal solutions. Hydrometallurgy, 8: 365-377.

Helgeson, H.C., 1967. Thermodynamics of complex dissociation in aqueous solution at elevated temperatures. The Journal of Physical Chemistry, 71: 3121-3136.

Hixson, A.W. and Crowell, J.H., 1931. Dependence of reaction velocity upon surface and agitation. Industrial and Engineering Chemistry, 23: 923-931.

Hoak, R.D. and Sindlinger, C.J., 1949. New technique for waste pickle liquor neutralization. Industrial and Engineering Chemistry, 41: 65-70.

Hsu, P.H. and Marion, G., 1985. The solubility product of goethite. Soil Science, 140: 344-351.

Hug, S.J., 1997. In situ Fourier transform infrared measurements of sulfate adsorption on hematite in aqueous solutions. Journal of Colloid and Interface

Science, 188: 415-422.

Hug, S.J. and Bahnemann, D., 2006. Infrared spectra of oxalate, malonate and succinate adsorbed on the aqueous surface of rutile, anatase and lepidocrocite measured with in situ ATR-FTIR. Journal of Electron Spectroscopy and Related Phenomena, 150: 208-219.

Jackson, K.J. and Helgeson, H.C., 1985. Chemical and thermodynamic constraints on the hydrothermal transport and deposition of tin: I. Calculation of the solubility of cassiterite at high pressures and temperatures. Geochimica et Cosmochimica Acta, 49: 1-22.

Jambor, J.L. and Dutrizac, J.E., 1998. Occurrence and constitution of natural and synethetic ferrihydrite, a widespread iron oxyhydroxide. Chemical Reviews, 98: 2549-2585.

Janney, D.E., Cowley, J.M. and Buseck, P.R., 2000. Structure of synthetic 2-line ferrihydrite by electron nanodiffraction. American Mineralogist, 85: 1180-1187.

Jarvinen, G.D., 2008. Precipitation crystallization processes In: R.G. Wymer, D.S. Kosson, C. Atkins-Duffin, D. DePaoli, K. Higley and T. Todd (Editors), Short Course: Introduction to Nuclear Chemistry and Fuel Cycle Separations. Vanderbilt University School of Engineering. Department of Civil and Environmental Engineering, Nashville.

Johnson, J.A., McDonald, R.G., Whittington, B.I., Quan, L.P. and Muir, D.M., 2002. Process water salinity effects in the pressure leaching of Cawse nickel laterite ores. In: M.L. Peek and G. Van Weert (Editors), Chloride Metallurgy, Vol. 1. CIM, Montreal, 339-354.

Johnson, K.S. and Pytkowicz, R.M., 1979. Activity coefficients in electrolyte

solutions: Vol 2. CRC Press, Boca Raton, Florida.

Jolivet, J.P., Chanéac, C. and Tronc, E., 2004. Iron oxide chemistry. From molecular clusters to extended solid networks. Chemical Communications: 481-487.

Jönsson, J., Persson, P., Sjöberg, S. and Lövgren, L., 2005. Schwertmannite precipitated from acid mine drainage: phase transformation, sulphate release and surface properties. Applied Geochemistry, 20: 179-191.

Kabai, J., 1973. Determination of specific activation energies of metal oxides and metal oxide hydrates by measurement of the rate of dissolution. Acta Chimica Academiae Scientiarum Hungaricae, 78: 57-73.

Kaur, N., Singh, B. and Kennedy, B.J., 2010. Dissolution of Cr, Cd, Zn and Pb single- and multi-metal substituted goethite: relation to structural and morphological properties. Clays and Clay Minerals, 58: 415-430.

Kawano, M. and Tomita, K., 2001. Geochemical modeling of bacterially induced mineralization of schwertmannite and jarosite in sulfuric acid spring water. American Mineralogist, 86: 1156-1165.

Kenttämaa, J., 1958. A cryoscopic study of ionic association in bivalent metal sulphates using saturated aqueous solutions. Acta Chemica Scandinavica, 12: 1323-1329.

Kiyama, M. and Takada, T., 1973. The hydrolysis of ferric complexes. magnetic and spectrophotometric studies of aqueous solutions of ferric salts. Bulletin of the Chemical Society of Japan, 46: 1680-1686.

Knight, R.J. and Sylva, R.N., 1974. Precipitation in hydrolysed iron (III) solutions. Journal of Inorganic and Nuclear Chemistry, 36: 591-574.

Köse, C.H. and Topkaya, Y.A., 2011. Hydrometallurgical processing of nontronite type lateritic nickel ores by MHP process. Minerals Engineering, 24: 396-415.

Landers, M. and Gilkes, R.J., 2007. Dehydroxylation and dissolution of nickeliferous goethite in New Caledonian lateritic Ni ore. Applied Clay Science, 35: 162-172.

Landers, M., Gilkes, R.J. and Wells, M., 2009. Dissolution kinetics of dehydroxylated nickeliferous goethite from limonitic lateritic nickel ore. Applied Clay Science, 42: 615-624.

Lazaroff, N., 1983. The exclusion of D_2O from the hydration sphere of $FeSO_4{-}7H_2O$ oxidized by thiobacillus ferrooxidans. Science, 222: 1331-1334.

Lewis, D. and Cardile, C., 1989. Hydrolysis of Fe III solution to hydrous iron oxides. Australian Journal of Soil Research, 27: 103-115.

Lewis, D.G. and Schwertmann, U., 1979. The influence of Al on iron oxides. Part III. Preparation of Al goethites in M KOH. Clay Minerals, 14: 115-126.

Lim-Nunez, R. and Gilkes, R.J., 1987. Acid dissolution of synthetic metal-containing goethite and hematites. In: L.G. Schultz, H.V. Olphen and F.A. Mumpton (Editors), Proceedings of the International Clay Conference. The Clay Minerals Society, Denver, 197-204.

Lindsay, W.L., 1979. Chemical equilibria in soils. Wiley Interscience New York.

Lister, M.W. and Rivington, D.E., 1955. Ferric sulphate complexes, and ternary complexes with thiocyanate ions. Canadian Journal of Chemistry, 33: 1591-1602.

Liu, H., 2003. Atmospheric pressure leach process for lateritic nickel ore. World Patent 2003/093517 A1.

Liu, H., 2006. An improved process for heap leaching of nickeliferous oxidic ores. World Patent 2006/119559 A1.

Liu, H. and Papangelakis, V.G., 2005. Chemical modeling of high temperature aqueous processes. Hydrometallurgy, 79: 48-61.

Liu, H. and Reynolds, G.A., 2011. Process for atmospheric leaching of laterite ores using hypersaline leach solution. US Patent No. 2011/0056333 A1.

Liu, X. and Millero, F.J., 1999. The solubility of iron hydroxide in sodium chloride solutions. Geochimica et Cosmochimica Acta, 63: 3487-3497.

Lo, B. and Waite, T.D., 2000. Structure of Hydrous Ferric Oxide Aggregates. Journal of Colloid and Interface Science, 222: 83-89.

Loan, M., 2004. The paragoethite process: fundamentals of ferrihydrite, schwertmannite and goethite precipitation. Ph.D Thesis, Curtin University.

Loan, M., Cowley, J.M., Hart, R. and Parkinson, G.M., 2004. Evidence on the structure of synthetic schwertmannite. American Mineralogist, 89: 1735-1742.

Loan, M., Newman, O.M.G., Cooper, R.M.G., Farrow, J.B. and Parkinson, G.M., 2006. Defining the Paragoethite process for iron removal in zinc hydrometallurgy. Hydrometallurgy, 81: 104-129.

Loan, M., St.Pierre, T.G., Parkinson, G.M., Newman, O.M.G. and Farrow, J.B., 2002. Identifying nanoscale ferrihydrite in hydrometallurgical residues. Journal of Metals, 54: 40-43.

Lowenhaupt, H.E., Litz, J.E. and Howe, D.L., 1985. Methods of recovering nickel from laterite ores. US Patent No. 4548794.

Majzlan, J., Navrotsky, A. and Schwertmann, U., 2004. Thermodynamics of iron oxides: Part III. Enthalpies of formation and stability of ferrihydrite (~$Fe(OH)_3$), schwertmannite (~$FeO(OH)_{3/4}(SO_4)_{1/8}$), and ε-$Fe_2O_3$. Geochimica et Cosmochimica Acta, 68: 1049-1059.

Mangravite, F., Leitz, C. and Galick, P., 1985. Organic polymeric flocculants: Effect of charge density, molecular weight and particle concentration. In: B.M. Moudgil and P. Somasundaran (Editors), Flocculation, sedimentation and consolidation: Proceedings of the Engineering Foundation Conference. American Institute of Chemical Engineers, Sea Island, Georgia, 139-158.

Manov, G.G., Bates, R.G., Hamer, W.J. and Acree, S.F., 1943. Values of the constants in the Debye-Hückel Equation for activity coefficients. Journal of the American Chemical Society, 65: 1765-1767.

Marshall, W.L. and Jones, E.V., 1966. Second dissociation constant of sulfuric acid from 25 to 350° Evaluated from solubilities of calcium sulfate in sulfuric acid solutions. The Journal of Physical Chemistry, 70: 4028-4040.

Martell, A.E. and Smith, R.M., 1977. Critical stability constants. Plenum Press, New York.

Matijević, E., Sapieszko, R.S. and Melville, J.B., 1975. Ferric hydrous oxide sols I. Monodispersed basic iron(III) sulfate particles. Journal of Colloid and Interface Science, 50: 567-581.

Mayhew, K., Mean, R., O'Connor, L. and Williams, T., 2009. Nickel and cobalt recovery from Mesaba concentrate, Proceedings of the 14th Annual ALTA Nickel/Cobalt Conference. ALTA Metallurgical Services, Perth, Australia.

McCristal, T.G. and Manning, J., 1998. Conversion of the Pasminco Hobart smelter

to para-goethite. In: J.E. Dutrizac, J.A. Gonzales, G.L. Bolton and P. Hancock (Editors), Zinc and Lead Processing. The Metallurgical Society of CIM, Montreal, 439-453.

McDonald, R.G. and Whittington, B.I., 2008a. Atmospheric acid leaching of nickel laterites review Part I. Sulphuric acid technologies. Hydrometallurgy, 91: 35-55.

McDonald, R.G. and Whittington, B.I., 2008b. Atmospheric acid leaching of nickel laterites review. Part II. Chloride and bio-technologies. Hydrometallurgy, 91: 56-69.

Meyer, E.H.O., Howard, G., Heagele, R. and Beck, R.D., 1996. Iron control and removal at the Zinc Corporation of South Africa. In: J.E. Dutrizac and G.B. Harris (Editors), Proceedings of the Second International Symposium on Iron Control in Hydrometallurgy. Canadian Institue of Mining, Metallurgy and Petroleum, Ottawa, 163-182.

Michel, F.M., Barrón, V., Torrent, J., Morales, M.P., Serna, C.J., Boilye, J.F., Liu, Q., Ambrosini, A., Cismasu, A.C. and Brown Jr., G.E., 2010. Ordered ferrimagnetic form of ferrihydrite reveals links among structure, composition, and magnetism. Proceedings of the National Academy of Science of the United States of America, 107: 2787-2792.

Michel, F.M., Ehm, L., Antao, S.M., Lee, P.L., Chupas, P.J., Liu, G., Strongin, D.R., Schoonen, M.A.A., Phillips, B.L. and Parise, J.B., 2007. The structure of ferrihydrite, a nanocrystalline material. Science 316: 1726-1729.

Millero, F.J. and Pierrot, D., 2007. The activity coefficients of Fe(III) hydroxide complexes in NaCl and $NaClO_4$ solutions. Geochimica et Cosmochimica Acta, 71: 4825-4833.

Millero, F.J., Yao, W. and Aicher, J., 1995. The speciation of Fe(II) and Fe(III) in

natural waters. Marine Chemistry, 50: 21-39.

Misawa, T., Hashimoto, K. and Shimodaira, S., 1974. The mechanism of formation of iron oxide and oxyhydroxides in aqueous solutions at room temperature. Corrosion Science, 14: 131-149.

Missen, R.W., Mins, C.A. and Saville, B.A., 1999. Introduction to chemical reaction engineering and kinetics. John Wiley and Sons, Inc., Toronto.

Montgomery, D.C., 2005. Design and analysis of experiments John Wiley and Sons, Inc., Hoboken, New Jersey.

Morgan, B. and Lahav, O., 2007. The effect of pH on the kinetics of spontaneous Fe(II) oxidation by O_2 in aqueous solution-basic principles and a simple heuristic description. Chemosphere, 68: 2080-2084.

Mullin, J.W., 2001. Crystallization. Elsevier Butterworth-Heinemann, London.

Murad, E. and Rojík, P., 2003. Iron-rich precipitates in a mine drainage environment: Influence of pH on mineralogy. American Mineralogist, 88: 1915-1918.

Musić, S., Orehovec, Z. and Popović, S., 1994. Structural properties of precipitates formed by hydrolysis of Fe^{3+} ions in $Fe_2(SO_4)_3$ solutions. Journal of Materials Science, 29: 1991-1998.

Myers, R.H. and Montgomery, D.C., 2002. Response surface methodology: process and product optimization using designed experiments. John Wiley and Sons, Inc., New York.

Myneni, S.C.B., 2000. X-ray and vibrational spectroscopy of sulfate in earth materials. Reviews in Mineralogy and Geochemistry, 40: 113-172.

Nakamoto, K., 1986. Infrared and Raman spectra of inorganic and coordination compounds. John Wiley and Sons, New York.

Norén, K. and Persson, P., 2007. Adsorption of monocarboxylates at the water/goethite interface: The importance of hydrogen bonding. Geochimica et Cosmochimica Acta, 71: 5717-5730.

Oustadakis, P., Agatzini-Leonardou, S. and Tsakiridis, P.E., 2006. Nickel and cobalt precipitation from sulphate leach liquor using MgO pulp as neutralizing agent. Minerals Engineering, 19: 1204-1211.

Papangelakis, V.G. and Demopoulos, G.P., 1990. Acid pressure oxidation of arsenopyrite: I. Reaction chemistry. Canadian Metallurgical Quarterly, 29: 1-12.

Papangelakis, V.G., Liu, H. and Rubisov, D.H., 2004. Solution chemistry and reactor modelling of the PAL-process: Successes and challenges, in International Laterite Nickel Symposium-2004 (ed: W P Imrie), 289-305

Parfitt, R.L. and Smart, R.S.C., 1978. The mechanism of sulphate adsorption on iron oxides. Soil Science Society of America Journal, 42: 48-50.

Parida, K.M. and Das, J., 1996. Studies on ferric oxide hydroxides. Part 1 Effect of sulfate ions on the formation and physico-chemical properties of ferric oxide hydroxides prepared by a homogeneous precipitation method. Journal of Materials Science, 29: 1991-1998.

Parks, G.A., 1965. The isoelectric points of solid oxides, solid hydroxides, and aqueous hydroxo complex systems. Chemical Reviews, 65: 177-198.

Paul, K.W., Borda, M.J., Kubicki, J.D. and Sparks, D.L., 2005. Effect of dehydration on sulfate coordination and speciation at the Fe-(Hydr)oxide-water interface: A

molecular orbital/density functional theory and fourier transform infrared spectroscopic investigation. Langmuir, 21: 11071-11078.

Peak, D., Ford, R.G. and Sparks, D.L., 1999. An in situ ATR-FTIR investigation of sulfate bonding mechanisms on goethite. Journal of Colloid and Interface Science, 218: 289-299.

Perrier, N., Gilkes, R.J. and Colin, F., 2006. Heating Fe oxide-rich soils increases the dissolution rate of metal. Clays and Clay Minerals, 54: 165-175.

Persson, P. and Lövgren, L., 1996. Potentiometric and spectroscopic studies of sulfate complexation at the goethite-water interface. Geochimica et Cosmochimica Acta, 60: 2789-2799.

Pitzer, K.S., 1991. Activity coefficients in electrolyte solutions. CRC Press, Boca Raton, Florida.

Pivovarov, S., 2005. Modeling of ionic equilibria of trace metals (Cu^{2+}, Zn^{2+}, Cd^{2+}) in concentrated aqueous electrolyte solutions at 25°C. Journal of Colloid and Interface Science, 291: 421-432.

Plyasunova, N.V., Zhang, Y. and Muhammed, M., 1998. Critical evaluation of thermodynamics of complex formation of metal ions in aqueous solutions. IV. Hydrolysis and hydroxo-complexes of Ni^{2+} at 298.15 K. Hydrometallurgy, 48: 43-63.

Pollard, R.J., Cardile, C.M., Lewis, D.G. and Brown, L.J., 1992. Characterization of FeOOH polymorphs and ferrihydrite using low-temperature, applied-field, Mössbauer spectroscopy. Clay Minerals, 27: 57-71.

Rafal, M., Berthold, J.W., Scrivner, N.C. and Grise, S.L., 1995. Models for electrolyte solutions. In: S.I. Sandler (Editor), Models for thermodynamics and phase

equilibria calculations. Marcel Dekker, New York, 601-670.

Rancourt, D.G. and Meunier, J.F., 2008. Constraints on structural models of ferrihydrite as a nanocrystalline material. American Mineralogist, 93: 1412-1417.

Regenspurg, S., 2002. Characterisation of schwertmannite geochemical interactions with arsenate and chromate and significance in sediments of lignite opencast lakes. Ph.D Thesis, Universität Bayreuth.

Roche, E.G., 2009. Iron precipitation. World Patent 2009/155651 A1.

Rubisov, D.H. and Papangelakis, V.G., 2000. Sulphuric acid pressure leaching of laterites-speciation and prediction of metal solubilities “at temperature”. Hydrometallurgy, 58: 13-26.

Sánchez-España, J., Yusta, I. and Diez-Ercilla, M., 2011. Schwertmannite and hydrobasaluminite: A re-evaluation of their solubility and control on the iron and aluminium concentration in acidic pit lakes. Applied Geochemistry, 26: 1752-1774.

Sapieszko, R.S., Patel, R.C. and Matijević, E., 1977. Ferric hydrous oxide sols. 2. Thermodynamics of aqueous hydroxo and sulfato ferric complexes. Journal of Physical Chemistry, 81: 1061-1068.

Schneide, W., 1984. Hydrolysis of iron(III)-chaotic olation versus nucleation. Comments on Inorganic Chemistry, 3: 205-223.

Schroth, A.W. and Parnell Jr, R.A., 2005. Trace metal retention through the schwertmannite to goethite transformation as observed in a field setting, Alta Mine, MT. Applied Geochemistry, 20: 907-917.

Schulze, D.G., 1981. Identification of soil iron oxide minerals by differential X-ray diffraction. Soil Science Society of America Journal, 45: 437-440.

Schulze, D.G., 1986. Correction of mismatches in 2θ scales during differential X-ray diffraction. Clays and Clay Minerals, 34: 681-685.

Schwertmann, U., 1991. Solubility and dissolution of iron oxide. Plant and Soil, 130: 1-25.

Schwertmann, U. and Carlson, L., 2005. The pH-dependent transformation of schwertmannite to goethite at 25°C. Clay Minerals, 40: 63-66.

Schwertmann, U. and Cornell, R.M., 2000. Iron oxides in the laboratory: preparation and characterization (second edition). Wiley-VCH GmbH and Co. KGaA, Weiheim.

Schwertmann, U., Friedl, J. and Stanjek, H., 1999. From Fe (III) ions to ferrihydrite and then to hematite. Journal of Colloid and Interface Science, 209: 215-223.

Schwertmann, U., Gasser, U. and Sticher, H., 1989. Chromium-for-iron substitution in synthetic goethites. Geochimica et Cosmochimica Acta, 53: 1293-1297.

Schwertmann, U. and Murad, E., 1983. Effect of pH on the formation of goethite and hematite from ferrihydrite. Clays and Clay Minerals, 31: 277-284.

Schwertmann, U., Schulze, D.G. and Murad, E., 1982. Identification of ferrihydrite in soils by dissolution kinetics, differential X-ray diffraction, and Mössbauer spectroscopy. Soil Science Society of America Journal, 46: 869-875.

Seyssiecq, I., Veesler, S., Boistelle, R. and Lamérant, J.M., 1998. Agglomeration of gibbsite $Al(OH)_3$ crystals in Bayer liquors. Influence of the process parameters. Chemical Engineering Science, 53: 2177-2185.

Singh, B. and Gilkes, R.J., 1992. Properties and distribution of iron oxides and their association with minor elements in the soils of south-western Australia. Journal of Soil Science, 43: 77-98.

Singh, B., Sherman, D.M., Gilkes, R.J., Wells, M.A. and Mosselmans, J.F.W., 2002. Incorporation of Cr, Mn and Ni into goethite (α-FeOOH): mechanism from extended X-ray absorption fine structure spectroscopy. Clay Minerals, 37: 639-649.

Sipos, P., Bódi, I., May, P.M. and Hefter, G.T., 1997. The ionic product of water in concentrated tetramethylammonium chloride solutions. Talanta, 44: 617-620.

Söhnel, O. and Garside, J., 1992. Precipitation basic principles and industrial applications. Butterworth-Heinemann Ltd, Oxford.

Steemson, M. and Smith, M., 2009. The development of nickel laterite heap leach projects, Proceedings of the 14th Annual ALTA Nickel/Cobalt Conference. ALTA Metallurgical Services, Perth, Australia.

Stefánsson, A., 2007. Iron(III) hydrolysis and solubility at 25 °C. Environmental Science and Technology, 41: 6117-6123.

Stipp, S.L., 1990. Speciation in the iron(II)-iron(III)-sulfate-water system at 25.degree.C and low pH: sensitivity of an equilibrium model to uncertainties. Environmental Science and Technology, 24: 699-706.

Stumm, W., Furrer, G., Wieland, E. and Zinder, B., 1985. The effect of complex-forming ligands on the dissolution of oxides and aluminosilicates. In: J.I. Drever (Editor), The Chemistry of Weathering, Dordrecht, Netherlands, 55-74.

Sundkvist, J.E., 2002. Method of purifying acid leaching solution by precipitation and oxidation. US Patent No. 6, 406, 676 B1.

Tödheide, K., 1972. Water at high temperature and pressure. In: F. Franks (Editor), Water. A Comprehensive Treatise. Plenum Press, New York, 1972-1975.

Towe, K.M. and Bradley, W.F., 1967. Mineralogical constitution of colloidal

"hydrous ferric oxides". Journal of Colloid and Interface Science, 24: 384-392.

Tsangaris, D.M. and Baltzis, B.C., 1996. Evaluation of batch and semi-batch reactor operation for enzymatic reactions with inhibitory kinetics. Chemical Engineering Science, 51: 2757-2762.

Turnbull, D., 1952. Kinetics of solidification of supercooled liquid mercury droplets. The Journal of Chemical Physics, 20: 411-424.

Vasil'eV, V.P., 1962. Influence of ionic strength on the instability constants of complexes. Russian Journal of Inorganic Chemistry, 7: 924-927.

Vasil'eV, V.P., 2004. On so-called concentration and true thermodynamic equilibrium constant in solution. Russian Journal of Coordination Chemistry, 30: 73-74.

Vlek, P.L.G., Blom, T.J.M., Beek, J. and Lindsay, W.L., 1974. Determination of the solubility product of various iron hydroxides and jarosite by the chelation method. Soil Science Society of America Journal 38: 429-432.

Wang, W. and Breisinger, D., 1998. The acid-base behavior of zinc sulfate electrolytes: The temperature effect. Metallurgical and Materials Transactions B, 29: 1157-1166.

Webster, J.G., Swedlund, P.J. and Webster, K.S., 1998. Trace metal adsorption onto an acid mine drainage iron(III) oxy hydroxy sulfate. Environmental Science and Technology, 32: 1361-1368.

Weckler, B. and Lutz, H.D., 1998. Lattice vibration spectra. Part XCV. Infrared spectroscopic studies on the iron oxide hydroxides goethite (α), akaganéite (β), lepidocrocite (γ), and feroxyhite (δ). European Journal of Solid State and Inorganic Chemistry, 35: 531-544.

Wells, M.A., Fitzpatrick, R.W. and Gilkes, R.J., 2006. Thermal and mineral properties of Al-, Cr-, Mn-, Ni- and Ti-substituted goethite. Clays and Clay Minerals, 54: 176-194.

Wells, M.A., Gilkes, R.J. and Fitzpatrick, R.W., 2001. Properties and acid dissolution of metal-substituted hematites. Clays and Clay Minerals, 49: 60-72.

Whittington, B.I. and Johnson, J.A., 2005. Pressure acid leaching of arid-region nickel laterite ore. Part III Effect of process water on nickel losses in the residue. Hydrometallurgy, 78: 256-263.

Whittington, B.I., Johnson, J.A., Quan, L.P., McDonald, R.G. and Muir, D.M., 2003a. Pressure acid leaching of arid-region nickel laterite ore. Part II. Effect of ore type. Hydrometallurgy, 70: 47-62.

Whittington, B.I., McDonald, R.G., Johnson, J.A. and Muir, D.M., 2003b. Pressure acid leaching of arid-region nickel laterite ore. Part I: effect of water quality. Hydrometallurgy, 70: 31-46.

Whittington, B.I. and Muir, D., 2000. Pressure acid leaching of nickel laterites A review. Mineral Processing and Extractive Metallurgy Review 21: 527-600.

Yakovlev, Y.B., Kul'ba, F.Y., Pus'ko, A.G. and Gerchikova, M.N., 1977. Hydrolysis of iron (III) sulphate in zinc sulphate solutions at 25, 50, and 80 ^{o}C. Russian Journal of Inorganic Chemistry, 22: 27-29.

Yu, J.Y., Heo, B., Choi, I.K., Cho, J.P. and Chang, H.W., 1999. Apparent solubilities of schwertmannite and ferrihydrite in natural stream waters polluted by mine drainage. Geochimica et Cosmochimica Acta, 63: 3407-3416.

Zinck, J.M., 1993. An investigation into the hydrolytic precipitation of iron (III) from

sulphate-bearing effluents. M.Eng Thesis, McGill University.

Zinck, J.M. and Dutrizac, J.E., 1998. The behaviour of zinc, cadmium, thallium, tin and selenium during ferrihydrite precipitation from sulphate solutions. CIM Bulletin, 91: 94-101.

APPENDIX A: Computer Program for Chemical Equilibrium Study

A sample Microsoft® Visual C++ computer program that was written to study the chemical equilibrium of the Fe(III)–Ni(II)–H_2SO_4–H_2O system. This program was used to solve the non-liner equations (Eqs. 3.53-3.56) and construct Figures 3.2-3.7. The simulated solution contained 0.015 mol Fe^{3+}, 0.0025 mol Ni^{2+} and 0.05 mol SO_4^{2-}.

```
#include <stdio.h>
#include <stdlib.h>
#include <math.h>
void f(x,y,n)
int n;
double x[],y[];
{
        double k0,k1,k2,k3,k4,k5,k6,k7,k8,k9,k10,k11,k12,k13,k14,k15,k16,k17;

//The initial ionic strength;

  k0=0.1975;

 //Equilibrium constants;

  k1=pow(10,-13.9836+1.017*sqrt(k0)/(1+1.6*sqrt(k0))-0.5176*k0);
  k2=pow(10,-2.2136-2.034*sqrt(k0)/(1+1.6*sqrt(k0))+0.1105*k0);
  k3=pow(10,-5.7215-3.051*sqrt(k0)/(1+1.6*sqrt(k0))+0.1151*k0);
  k4=pow(10,-2.9252+0.0383*k0);
  k5=pow(10,-21.5703-2.034*sqrt(k0)/(1+1.6*sqrt(k0))-0.3633*k0);
  k6=pow(10, 1.4188-3.051*sqrt(k0)/(1+1.6*sqrt(k0))-0.0864*k0);
  k7=pow(10,4.1388-6.102*sqrt(k0)/(1+1.6*sqrt(k0))+0.1439*k0);
  k8=pow(10,5.4126-8.136*sqrt(k0)/(1+1.6*sqrt(k0))+0.7036*k0);
  k9=pow(10,1.5239-9.905*sqrt(k0)/(1+1.6*sqrt(k0))+0.0294*k0);
  k10=pow(10,-9.8493-3.051*sqrt(k0)/(1+1.6*sqrt(k0))+0.3581*k0);
  k11=pow(10,-9.4783-1.022*sqrt(k0)/(1+sqrt(k0))+0.15);
  k12=pow(10,-29.9539);
  k13=pow(10,-9.7930+1.022*sqrt(k0)/(1+sqrt(k0)));
  k14=pow(10,-27.8061+2.044*sqrt(k0)/(1+sqrt(k0))-0.26);
  k15=pow(10,-18.0536-1.022*sqrt(k0)/(1+sqrt(k0))+0.05);
```

```
  k16=pow(10,2.3517+3.9*sqrt(k0)/(1+2.22*sqrt(k0))+0.32*k0);
  k17=pow(10,1.3438);

//x[0], x[1], x[2] and x[3] refer to [Fe3+], [H+], [SO4 2–] and [Ni2+], respectively;

//Ferric iron mass-balance;

y[0]=0.015-x[0]-k2*x[0]/x[1]-k3*x[0]/x[1]/x[1]-2*k4*x[0]*x[0]/x[1]/x[1]-k5*x[0]/
x[1]/x[1]/x[1]/x[1]-k7*x[0]*x[2]-k8*x[0]*x[2]*x[2]-k6*k17*x[0]*x[1]*x[2]-k10*
x[0]/x[1]/x[1]/x[1]/x[1]-2*k9*x[0]*x[0]*x[2]*x[2]*x[2];

//Nickel mass-balance;

y[1]=0.0025-x[3]-k11*x[3]/x[1]-k12*x[3]/x[1]/x[1]/x[1]-2*k13*x[3]*x[3]/x[1]-
4*k14*x[3]*x[3]*x[3]*x[3]/x[1]/x[1]/x[1]/x[1]-k15*x[3]/x[1]/x[1]-k16*x[3]*x[2];

//Sulphate mass-balance;

y[2]=0.05-x[2]-k7*x[0]*x[2]-2*k8*x[0]*x[2]*x[2]-k6*k17*x[0]*x[1]*x[2]-3*k9*
x[0]*x[0]*x[2]*x[2]*x[2]-k17*x[1]*x[2]-k16*x[3]*x[2];

//Charge-balance;

y[3]=3*x[0]+2*k2*x[0]/x[1]+k3*x[0]/x[1]/x[1]+4*k4*x[0]*x[0]/x[1]/x[1]+k7*x[0]*
x[2]+2*k6*k17*x[0]*x[1]*x[2]+2*x[3]+k11*x[3]/x[1]+3*k13*x[3]*x[3]/x[1]+4*k1
4*x[3]*x[3]*x[3]*x[3]/x[1]/x[1]/x[1]/x[1]+x[1]-k5*x[0]/x[1]/x[1]/x[1]/x[1]-
k8*x[0]*x[2]*x[2]-k12*x[3]/x[1]/x[1]/x[1]-k1/x[1]-k17*x[1]*x[2]-2*x[2];


        n=n;
        return;
}

int gaus(a,b,n)
int n;
double a[],b[];
{
        int *js,l,k,i,j,is,p,q;
        double d,t;
        js=malloc(n*sizeof(int));
        l=1;
        for(k=0;k<=n-2;k++)
        {
                d=0.0;
```

```
for(i=k;i<=n-1;i++)
        for(j=k;j<=n-1;j++)
        {
                t=fabs(a[i*n+j]);
                if (t>d)
                {
                        d=t;
                        js[k]=j;
                        is=i;
                }
        }
if(d+1.0==1.0)
        l=0;
else
{
        if(js[k]!=k)
                for(i=0;i<=n-1;i++)
                {
                        p=i*n+k;
                        q=i*n+js[k];
                        t=a[p];
                        a[p]=a[q];
                        a[q]=t;
                }
        if(is!=k)
        {
                for(j=k;j<=n-1;j++)
                {
                        p=k*n+j;
                        q=is*n+j;
                        t=a[p];
                        a[p]=a[q];
                        a[q]=t;
                }
                t=b[k];
                b[k]=b[is];
                b[is]=t;
        }
}

if(l==0)
{
        free(js);
        printf("fail\n");
```

```
                return (0);
        }
        d=a[k*n+k];
        for(j=k+1;j<=n-1;j++)
        {
                p=k*n+j;
                a[p]=a[p]/d;
        }
        b[k]=b[k]/d;
        for(i=k+1;i<=n-1;i++)
        {
                for(j=k+1;j<=n-1;j++)
                {
                        p=i*n+j;
                        a[p]=a[p]-a[i*n+k]*a[k*n+j];
                }
                b[i]=b[i]-a[i*n+k]*b[k];
        }
}
d=a[(n-1)*n+n-1];
if(fabs(d)+1.0==1.0)
{
        free(js);
        printf("fail\n");
        return (-3);
}
b[n-1]=b[n-1]/d;
for(i=n-2;i>=0;i--)
{
        t=0.0;
        for(j=i+1;j<=n-1;j++)
                t=t+a[i*n+j]*b[j];
        b[i]=b[i]-t;
}
js[n-1]=n-1;
for(k=n-1;k>=0;k--)
        if(js[k]!=k)
        {
                t=b[k];
                b[k]=b[js[k]];
                b[js[k]]=t;
        }
free(js);
return(1);
```

```
}



int netn(n,eps,t,h,x,k,f)
int n,k;
void (*f)();
double eps,t,h,x[];
{
        int i,j,l;
        double am, z,beta,d,*y,*a,*b;
        y=malloc(n*sizeof(double));
        a=malloc(n*n*sizeof(double));
        b=malloc(n*sizeof(double));
        l=k;
        am=1.+eps;
        while(am>=eps)
        {
                (*f)(x,b,n);
                am=0.;
                for(i=0;i<=n-1;i++)
                {
                        z=fabs(b[i]);
                        if(z>am)
                                am=z;
                }
                if(am>=eps)
                {
                        l=l-1;
                        if(l==0)
                        {
                                free(y);
                                free(b);
                                free(a);
                                printf("fail\n");
                                return (0);
                        }
                        for(j=0;j<=n-1;j++)
                        {
                                z=x[j];
                                x[j]=x[j]+h;
                                (*f)(x,y,n);
                                for(i=0;i<=n-1;i++)
                                        a[i*n+j]=y[i];
```

```
                        x[j]=z;
                    }
                    if(gaus(a,b,n)==0)
                    {
                        free(y);
                        free(b);
                        free(a);
                        printf("fail\n");
                        return (-1);
                    }
                    beta=1.0;
                    for(i=0;i<=n-1;i++)
                        beta=beta-b[i];
                    if(fabs(beta)+1.==1.)
                    {
                        free(y);
                        free(b);
                        free(a);
                        printf("fail\n");
                        return (-2);
                    }
                    d=h/beta;
                    for(i=0;i<=n-1;i++)
                        x[i]=x[i]-d*b[i];
                    h=t*h;
                }
        }
        free(y);
        free(b);
        free(a);
        return (k-1);
}

void main()
{
        int i,k;
        void f(double [], double [], int);
        double eps, t, h;
        static double x[4]={1.0,1.0,1.0,1.0};
        t=0.1;
        h=0.1;
        eps=1e-8;
        k=1000;
        i=netn(4,eps,t,h,x,k,f);
```

```
        printf("\n");
        printf("i=%d\n",i);
        printf("\n");
        for(i=0;i<=3;i++)
                printf("x(%d)=%lf\n",i,x[i]);
        printf("\n");
}
```

APPENDIX B: Box-Behnken Design

Box-Behnken Design (BBD) is an incomplete three level factorial design for response surface methodology (RSM). The number of experiments (N) for BBD is $N=2k(k-1)+C_0$, where k is the number of factors and C_o is the number of central points. For three factors, this design requires 15 experiments composed of 12 middle points at the edges and 3 replicated central points. With three experiments at the central point, it is possible to estimate the pure error sum of squares, SS_{PE}.

The experimental data generated by BBD are normally used to fit a quadratic model given by:

$$y = \beta_0 + \sum_{i=1}^{k} \beta_i x_i + \sum_{i=1}^{k-1} \sum_{j=2}^{k} \beta_{ij} x_i x_j + \sum_{i=1}^{k} \beta_{ii} x_i^2 + \varepsilon \qquad \text{Eq. B.1}$$

where x_i and x_j represent coded factors, β_0 is a regression coefficient, β_i are linear coefficients, β_{ij} are the coefficients for the interaction terms and β_{ii} represent quadratic coefficients. The random error terms ε are generally assumed to follow a normal distribution with mean of zero and constant variance of σ^2, thus these errors are independent of each other. The relationship between the natural and coded factor is written as:

$$x_i = \frac{X_i - X_0}{\Delta X} \qquad \text{Eq. B.2}$$

where x_i is the coded value of an independent factor; X_i is the actual value of an independent factor; X_0 is the actual value of an independent factor at the central point, and ΔX is the step change value corresponding to a unit variation of the dimensionless value.

To simplify, Eq. B.1 can be written in matrix notation as:

$$\mathbf{Y} = \mathbf{X\beta} + \boldsymbol{\varepsilon} \qquad \text{Eq. B.5}$$

where **Y** is a matrix of the observations, **X** is a matrix of the independent factors, **β** and **ε** are the matrices of the regression coefficient and random error, respectively. The coefficients in Eq. B.3 can be determined by the method of least squares with the least squares function described as:

$$\mathbf{L} = \sum_{i=1}^{n} \boldsymbol{\varepsilon}_i^2 \qquad \text{Eq. B.4}$$

The least squares estimators, **b**, should satisfy the relationship:

$$\left.\frac{\partial \mathbf{L}}{\partial \boldsymbol{\beta}}\right|_{\mathbf{b}} = -2\mathbf{X}^{\mathbf{T}}\mathbf{Y} + 2\mathbf{X}^{\mathbf{T}}\mathbf{X}\mathbf{b} = 0 \qquad \text{Eq. B.5}$$

Thus the solution of Eq. B.5 or the least squares estimator of **β** is:

$$\mathbf{b} = (\mathbf{X}^{\mathbf{T}}\mathbf{X})^{-1}\mathbf{X}^{\mathbf{T}}\mathbf{Y} \qquad \text{Eq. B.6}$$

where $\mathbf{X}^{\mathbf{T}}$ is the transpose of the matrix **X**, and $(\mathbf{X}^{\mathbf{T}}\mathbf{X})^{-1}$ is the inverse of the matrix $\mathbf{X}^{\mathbf{T}}\mathbf{X}$.

PUBLICATIONS

The following peer-reviewed journal and conference publications have arisen from work completed by the candidate for this thesis.

Wang, K., Li, J., McDonald, R.G., Browner, R.E., 2013. Characterization of iron-rich precipitates from synthetic atmospheric nickel laterite leach solutions. Minerals Engineering, 40: 1-11.

Wang, K., Li, J., McDonald, R.G., Browner, R.E., 2012. The aqueous ionic equilibrium and speciation of iron and nickel in sulphuric solutions. XXVI International Mineral Processing Congress (IMPC), New Delhi, India, 5795-5813.

Wang, K., Li, J., McDonald, R.G., Browner, R.E., 2012. Nickel loss during iron precipitation and product characterization. Advanced Materials Research, 402: 293-296.

Wang, K., Li, J., McDonald, R.G., Browner, R.E., 2011. The effect of iron precipitation upon nickel losses from synthetic atmospheric nickel laterite leach solutions: Statistical analysis and modelling. Hydrometallurgy, 109: 140-152.